Indoor Optical Wireless Communications Supporting Secure Multiple Access

Tian Liang

Submitted in partial fulfilment of the requirements of the degree of

Doctor of Philosophy

Department of Electrical and Electronic Engineering

The University of Melbourne

Australia

July 2018

DECLARATION

This is to certify that

1. the thesis comprises only my original work towards the PhD,
2. none of the work presented in this thesis has been submitted for any other degree or diploma at my university.
3. due acknowledgement has been made in the text to all other material used,
4. the thesis is less than 100,000 words in length, exclusive of tables, figures, bibliographies, appendices and footnotes.

_____

Tian Liang, July 2018

Preface

This thesis comprises only my original work (100%), which I conducted under the supervision of Professor Thas (Ampalavanapillai) Nirmalathas, Professor Christina Lim, Professor Elaine Wong and Dr. Desmond (Ke) Wang. All the work in this thesis was conducted by the author of this thesis including, analytical models, MATLAB simulations, theoretical analysis, experiments and manuscript writing, which contributed about 90% to the work. My supervisors provided insightful technical comments and discussions which contributed about 10% to the work.

The thesis has not been submitted for other qualifications. All the work towards the thesis was carried out after the enrolment in the degree. No third party editorial assistance was provided in preparation of the thesis. The work was partially supported by the Australian Commonwealth Government through an Australian Government Research Training Program Scholarship and the Australian Research Council (ARC) Discovery Project (DP170100268).

The 1st journal publication (listed in Chapter 1 Section 1.4) contains only the original work of the student, including experiments, analytical models, simulations and manuscripts writing, which contributed about 80% to the publication. Tingting Song was in collaboration to build up the initial experimental setup, which contributed about 10% to the publication. Professor Thas (Ampalavanapillai) Nirmalathas, Professor Christina Lim, Professor Elaine Wong and Dr. Desmond (Ke) Wang provided helpful discussions and comments, which contributed about 10% to the publication.

The 2nd and 3rd journal publications contain only the original work of the student, including experiments, analytical models, simulations and manuscripts writing, which contributed about 90% to the publication. Professor Thas (Ampalavanapillai) Nirmalathas, Professor Christina Lim, Professor Elaine Wong, Dr. Desmond (Ke)

Wang and Tingting Song provided helpful discussions and comments, which contributed about 10% to the publications.

The 4th journal publication is based on literature review provided and written by Dr. Desmond (Ke) Wang, which contributed 90% to the publication. The other authors including the author of the thesis provided helpful comments and editing, which contributed about 10% to the publication.

The 1st and 2nd conference publications contain only the original work of the student, including experiments, analytical models, simulations and manuscripts writing, which contributed about 90% to the publication. Professor Thas (Ampalavanapillai) Nirmalathas, Professor Christina Lim, Professor Elaine Wong, Dr. Desmond (Ke) Wang and Tingting Song provided helpful discussions and comments, which contributed about 10% to the publications.

The 3rd and 4th conference publications are based on literature review provided and written by Professor Thas (Ampalavanapillai) Nirmalathas and Dr. Desmond (Ke) Wang, respectively, which contributed 90% to each publication. The other authors including the author of the thesis provided helpful comments and editing, which contributed about 10% to the publication.

The 5th conference publication is written and based on research conducted by Tingting Song, which contributed about 80% to the publication. The author of the thesis was in collaboration to build the initial experimental setup, which contributed about 10% to the publication. The other authors provided helpful discussions and comments, which contributed about 10% to the publication.

The 6th conference publication is written and based on research conducted by Dr. Desmond (Ke) Wang, which contributed about 90% to the publication. The other authors including the author of the thesis provided helpful comments and editing, which contributed about 10% to the publication.

The 7th accepted conference paper contains the experimental results of the author of this thesis, Sampath Edirisinghe and Dr. Desmond (Ke) Wang, which contributed about 25% to the work, respectively. Professor Thas (Ampalavanapillai) Nirmalathas provided literature review and manuscript writing, which contributed about 20% to the work. The other authors provided helpful comments, which contributed about 5% to the work.

The 8^{h} invited conference paper contains the experimental results of the author of this thesis, Sampath Edirisinghe, Tingting Song and Dr. Desmond (Ke) Wang, which contributed about 17.5% to the work, respectively. Professor Thas (Ampalavanapillai) Nirmalathas provided literature review and manuscript writing, which contributed about 25% to the work. The other authors provided helpful comments, which contributed about 5% to the work.

Abstract

Bandwidth intensive applications such as high-definition video streaming, real-time video transmission, tactile communications, virtual reality (VR), augmented reality (AR) and the like are being developed for portable consumer devices connected wirelessly to the Internet. Increasing the bandwidth of the wireless connectivity has been the focus of much research. Optical wireless communications (OWC) system has emerged as a promising technique to provide high-speed wireless connections for data intensive applications as it can easily leverage today's well-developed fibre based broadband access networks. The OWC technology is preferable over other alternatives including Wi-Fi, millimetre-wave (mm-wave), and ultra-wideband (UWB) systems in certain deployment scenarios. The optical band employed in OWC systems has a huge amount of unregulated bandwidth and is also immune to the interference from the radio frequency (RF) band. With these key advantages, OWC systems can be implemented in personal living and working spaces providing scalable bandwidth. In addition, they can also be deployed in areas where RF signals are carefully controlled and managed, such as in hospitals and airplanes. The thesis presents a systematic investigation of key functionalities of OWC – high bandwidth through modulation formats, multi-user access, and security in the physical layer.

Firstly, a comprehensive analytical system model is built for typical indoor OWC system with a general square QAM modulation format to achieve high bandwidth and by using cost-effective opto-electronic components. By using experiments based on 1.25 Gb/s – 5 Gb/s 4-QAM modulation format and 2.5 Gb/s – 10 Gb/s 16-QAM modulated system to verify, an relatively accurate analytical model was developed and the impacts of key system parameters on the system performance are thoroughly analysed using the analytical model, such as transmission optical power, laser *RIN* property, expanded beam waist, background light power and so on.

A multi-user access scheme named as time-slot coding (TSC) scheme is proposed. The function of the TSC scheme is experimentally demonstrated based on 4-QAM and 16-QAM modulation formats, respectively. The adaptive loading function employing both 4-QAM and 16-QAM compatible with the TSC scheme is also studied. Experimental results show that the satisfactory coverage is improved by a maximum of 61.2% compared to the TSC scheme employing 16-QAM alone. Furthermore, time-slot code misalignment due to non-ideal timing issues during code generation process is investigated both experimentally and analytically. In particular, the effect of the code overlapping ratio on the bit error rate (BER) performance of a general square QAM modulation format is analytically derived for typical indoor OWC systems. The experimental results match with analytical results with 4-QAM and 16-QAM modulation formats and show that the code misalignment tolerance can be more than 92.3% for 4-QAM and 26.9% for 16-QAM with received optical power levels greater than -19.7 dBm.

A novel physical layer mechanism is proposed for the provision of simultaneously secure connections for multiple users in indoor OWC systems. It is achieved by employing the TSC scheme together with chaotic phase sequence. The chaotic phase sequence applied to each symbol to secure the transmission is generated according to the logistic map, which based on a key set containing a constant parameter r and an initial value x_1. The feasibility of showing the proposed mechanism is capable of providing OWC connections is proved by analytical study and experiments. Experimental results also show that adding the chaotic phase does not degrade the legitimate user's signal quality. The robustness is also critically investigated and both analytical and experimental results indicate that the proposed scheme was robust and was able to maintain high communication security against eavesdropper's high searching accuracy of 10^{-10} within the optical-wireless links. The time-slot code misalignment tolerance with chaotic phase is further studied through analytical model and experiments, where the agreement shows that 68.6% and 22.6% misalignment tolerance is achieved for 4-QAM and 16-QAM modulation formats, respectively, at the received optical power of over -20.2 dBm.

Acknowledgements

My deepest gratitude must foremost go to my supervisors, Professor Thas (Ampalavanapillai) Nirmalathas, Professor Christina Lim, Professor Elaine Wong and Dr. Desmond (Ke) Wang. Thanks to Thas's wise guidance, immense knowledge and incredible patience along with my entire PhD admission period, I always get inspired about how to flesh out and develop my research projects. I also feel impressive about Christina's enthusiasm for research, careful attention to detail and insightful comments. I am very grateful that my experimental demonstration skills are well developed because of the valuable experience provided by Christina, Elaine and Desmond. Furthermore, I feel really appreciated it for all my supervisors' superior editing and presentation skills to help proof-read and polish my research outputs. Thanks Desmond for always being the first one that gives prompt technical advice when I encounter problems. In addition to the aid of research, Christina also provides me with valuable opportunities to develop my interpersonal skills by undertaking teaching assistance work, which lay a good foundation to my early career. Furthermore, I would like to express my special gratitude to Elaine for that she does not only provide technical advice but also provides valuable advice on my life while she is always considerate and encouraging. I would also like to thank my Ph.D advisory committee chair, Professor Kenneth Crozier, for his time, useful comments and coordination. Again, here are millions of thanks to all my supervisors and my committee chair for their contributions to make my entire Ph.D candidature smooth.

Completing this work would have been all the more difficult were it not for the support and friendship provided by my dear friends and colleagues, Yu Tian, Lihua Ruan, Dr. Yifei Wang, Miao Sun, Jian Fang, Dr. Di Che, Dr. Imali Dias, Dr. Alan Lee, Dr. Chathurika Ranaweera, Dr. Benoit Gouhier, Yu Bai, and Yaqi Zhu. I feel really thankful that I have been together with them experienced a valuable period of life and shared various moments of life. Every time I encounter technical and/or personal issues, they

are around to listen and help. I would also like to express my sincere gratitude to all my friends whose names are not mentioned individually, other staff and colleagues from Photonics Research Lab and Department of Electrical and Electronic Engineering for their support and help in general. Special thanks must go to the University of Melbourne for providing scholarship, unlimited resources and world-class facilities.

Last but most important of all, my heartfelt gratitude is for my beloved family, especially for my parents, Wenfu Liang and Jun Cai, as well as my husband Hongtao Yang, who experienced all of the ups and downs of this journey but always provide me with unconditional love and support. Words cannot express how much I love you but time will tell.

To My Loving Parents and My Husband

Table of Contents

List of Figures

List of Tables

Chapter 1 Introduction

1.1 Motivation of the Thesis

Mobile communications have become increasingly important during the past decade, leading to a rapid proliferation of high-performance personal communication devices with constantly improving capabilities. As devices begin to support data-intensive applications including real-time video transmission, interactive gaming, virtual reality, augmented reality and tactile communications providing end users with ever improving user experience, the demands for high-speed wireless communications especially in personal area such as working and living spaces is also increasing [1, 2]. Compared to providing connectivity in personal area networks (PAN) via wired physical connections like fibre network, a matured technology bringing the Internet to the doorstep of users' premises, wireless access support mobility of end-users is becoming preferred access method.

To achieve high speed data rates for wireless indoor applications, several candidates have been proposed and studied. Wi-Fi is a popular wireless local area networking (WLAN) technology that provides relatively high-speed connections between electronic devices and central network. In ultra-wideband (UWB) systems, the transmitted information spreads over a sufficiently large bandwidth at a very low energy density level to share with but avoid interference with conventional standards. However, complex signal processing techniques are generally required due to limited available bandwidth in the allocated spectrum and restricted transmission signal power [3, 4]. Millimetre-wave (mm-wave) systems using the 60 GHz band are widely considered as one of the solutions for next-generation wireless communication systems, especially

when taking the scarce lower frequency RF spectrum into account [5]. Signal generation and distribution are always challenging and the requirement of high-bandwidth optoelectronics devices is costly. In addition to the candidates above, optical wireless communications technology where the optical radiation carries information via free space is another promising technology for high-speed indoor communications due to huge unregulated bandwidth in the optical region.

High-speed optical wireless communications channel has been widely studied where single user access exceeding 200 Gb/s can be achieved with the help of space division multiplexing or wavelength division multiplexing [6, 7]. At the same time, multi-user scenario for practical optical wireless communications applications has also attracted considerable attention. Similar to radio frequency systems, conventional multiple access techniques such as time-division multiple access, frequency-division multiple access, code-division multiple access and the combination of them can be adopted with optical wireless links. With sensitive requirement of signal-to-noise ratio for optical wireless communications system, time-division multiple access technique is considered more efficient and thus favourable [8]. However, strict synchronisation at the receiver side is always challenging and scheduling framework or guard intervals are thus appreciated to allow transmission of symbols over different time slots but complicate signal transmission and detection.

Due to transmissions in optical domain, another widely acknowledged advantage of optical wireless communications is the capability of providing physical layer security [8]. However, such advantage is based on the assumption of immediate vicinity with the use of very narrow optical beams. When multiple users (and devices) are covered with a wider optical beam, security issues arise. Alleviating communication security issues in optical wireless communications systems, especially those supporting multiple user access, has yet to be widely investigated.

Deep understanding is needed to compare different approaches and design choices and to thoroughly investigate system performance. An analytical system model for indoor optical wireless communications network has become necessary. Despite limited in their nature, current literature on modelling of optical wireless communications also suffers from limitations of model only applicable to signals with additive white Gaussian noise. The development of an analytical model that is adaptive to various

modulated symbol patterns and has the potential to analyse interference from a variety of signal formats still remains elusive.

1.2 Thesis Outline

The main objective of this thesis is to explore methodologies for supporting multiple user access of the indoor optical wireless communications with unprecedented levels of security to each user. An analytical system model for indoor optical wireless network is first mathematically formulated based on general square QAM modulation format but without loss of further potential to be modified to other symbol patterns. Experiments for verification of the derived system model are carried out based on both 4-QAM and 16-QAM modulation formats with a typical optical wireless communication link having various data rates. In order to provide multi-user connections, a novel scheme named as time-slot coding scheme is proposed. In time-slot coding scheme, each user is assigned a simple "pre-assigned code" to acquire its symbol sequence. The proposed solution is further experimentally demonstrated, where more than 5 users are considered. We also investigate the capability of time-slot coding scheme to support adaptive loading function by employing both 4-QAM and 16-QAM simultaneously to serve multiple users at different locations. Besides the benefits of providing multiple data rates at the same time, error-free coverage can be extended. The code misalignment that is likely to happen during practical code generation procedures is thoroughly evaluated via both analytical studies and experiments for two adjacent users. The multiple access system is further equipped with secure capability especially for cases where multiple users are covered by a single transmitter. The phase noise terms, which are determined by a chaotic logistic map, are applied to each user's symbol sequence to secure the corresponding transmission. The feasibility of utilising time-slot coding scheme together with chaotic phase noise to provide secure multi-user connections is investigated theoretically and experimentally. Power penalty introduced by the chaotic phase and the impact of the number of users are experimentally

demonstrated. In addition, the selection of securing key is comprehensively analysed via theoretical studies and experiment. The limitations of the secure multiple access scheme including tolerance against eavesdropper's exhaustive search and time-slot code misalignment is also studied analytically and verified via experiments. Last but not least, the impact of key system parameters on the typical indoor optical wireless system performance is thoroughly analysed using the derived analytical model, such as transmission optical power, laser *RIN* property, expanded beam waist, background light power, preamplifier noise and so on.

The thesis is structured as follows:

Chapter 2: Literature Review

This chapter provides a comprehensive review on promising techniques suitable for short-range communications including Wi-Fi, millimetre-wave, ultra-wide band and optical wireless communications systems. Previous studies of OWC with single channel transmission and challenges are also included. Traditional multiple access techniques in both electrical and optical domain are introduced. Adaptive loading techniques are also explored as a solution to improve system flexibility of multiple access networks. In addition, communication security techniques especially techniques for secure multi-user connections in the field of optical wireless communications are reviewed.

Chapter 3: System Model for Indoor Optical Wireless Communications with Square QAM

In this chapter, a comprehensive system model is formulated to facilitate analysis of typical optical wireless communications with quadrature amplitude modulation format under a general square constellation. Optical wireless connections with multiple data rates based on both 4-QAM and 16-QAM modulation formats are demonstrated. The proposed system model is verified through extensive comparisons between experimental and analytical results.

Chapter 4: Time-slot Coding Scheme for Multiple Access for Indoor Optical Wireless Communications

This chapter first introduces the principle of the proposed time-slot coding scheme aiming to provide simultaneous multi-user connections. Experimental demonstration of the multiple access capability of the scheme is performed for 5 users with 4-QAM and 16-QAM modulated data. This chapter also provides experimental investigation of

system performance with increasing number of users. Furthermore, two strategies of adaptive loading function compatible with the proposed time-slot coding scheme are described and experimentally demonstrated to improve system flexibility. The imperfect timing issues are investigated and mathematically formulated for both time-slot coding scheme and conventional time-division multiple access technique. This chapter also provides experimental results illustrating system performance affected by time-slot code misalignment.

Chapter 5: Secure Multi-user Connections for Indoor Optical Wireless Communications with Time-slot Coding and Chaotic Phase

In this chapter, a novel mechanism capable of providing secure multi-user connections is proposed by incorporating chaotic phase which is generated based on logistic map. Key performance metric, noise rate, is defined and derived to show feasibility of the proposed mechanism. Security feature and power penalty for legitimate users introduced by the introduction of chaotic phase terms are experimentally evaluated under various system scenarios. A comprehensive investigation on system robustness against un-authorised access is also undertaken in this chapter. The impact of exhaustive search performed by potential eavesdropper is evaluated through both theoretical analysis and experiments. Furthermore, system tolerance against code misalignment within the time-slot coding is mathematically formulated and experimentally demonstrated.

Chapter 6: Investigation on Impacts of Key System Parameters of High-speed Indoor Optical Wireless Communications

Performance of optical wireless communications systems with QAM modulation format with general square constellation are extensively evaluated in this chapter. Optimal beam waists and the corresponding maximised error-free coverage are determined for various system capacities. The impact of noise from transmitter, free-space transmission channel and detection on system performance is also formulated and evaluated. As another key factor in the proposed secure multiple access optical wireless communications network, code misalignment tolerance is studied with and without chaotic phase for various system capacities.

Chapter 7: Conclusions and Future Work

This chapter summarises research investigated throughout the thesis. Based on key findings of research work conducted for this thesis, relevant future work is also identified and the scope of such work are outlined in this thesis for the benefit of potential readers of the thesis.

1.3 Original Contributions

To achieve the objectives as mentioned in the last section, a novel scheme based on optical wireless communications in in-building applications that enables ultra-broadband communications to be established for multiple users simultaneously is devised. This multi-user scheme for OWC is based on time-slot coding and the performance is thoroughly characterised experimentally. The work is further extended to provide secure multi-user communication by employing chaotic phase generated by logistic map. The mechanism feasibility and robustness are critically investigated. Last but not least, a comprehensive analytical system model for typical OWC systems with a general square QAM modulation format is built with experimental verification to facilitate analysis of key system parameters. The summary below shows key contributions of this thesis provided by each chapter.

Chapter 3

- Formulation of the theoretical model for typical OWC systems with a general square QAM modulation format
    - Derived expression of signal-to-noise ratio (SNR)
    - Derived expression of standard deviation of received signal
    - Derived expression of symbol error rate (SER)
    - Derived expression of the relationship between SER and bit error rate (BER)
    - Derived BER equation

- Experimental demonstrated a typical indoor OWC system based on both 4-QAM and 16-QAM with multiple bit rates to verify the derived analytical model

Chapter 4

- Proposed time-slot coding (TSC) scheme for multiple access of indoor OWC connections
- Experimentally demonstrated multi-user connection function based on both 4-QAM and 16-QAM with multiple data rates for 5 users
- Investigated impact of the number of users on BER performance
- Proposed and experimentally demonstrated adaptive loading function compatible with TSC scheme
- Analytically and experimentally Investigated impact of imperfect timing on system performance
    - Derived SER equations for both conventional time-division multiple access (TDMA) and TSC scheme and analytically compared the results between them
    - Formulated mathematical expression of BER with time-slot code overlapping ratio and dominant system noise
    - Experimentally tested code misalignment tolerance for both 4-QAM and 16-QAM modulation formats and compared the experimental and analytical results

Chapter 5

- Proposed a novel mechanism to simultaneously provide secure connections for multiple users by employing TSC scheme and chaotic phase
- Analytically analysed feasibility of the secure mechanism and the impact of keys
- Experimentally evaluated power penalty introduced by the chaotic phase
- Experimentally demonstrated secure capability of the mechanism with 4-user connections
- Experimentally evaluated the impact of the number of users on the system performance
- Analysed limitations of the secured mechanism

  - Derived outage rate with exhaustive search and illustrated analytical results of key's impact
  - Mathematically formulated SER with search accuracy
  - Analytically evaluated the impact of key set on SER performance of eavesdropper
  - Analysed auto-correlation and cross-correlation of chaotic phase sequence
- Experimentally demonstrated system robustness against high search accuracy and verified the derived SER equation
- Evaluated tolerance to the time-slot code misalignment incorporating chaotic phase
  - Formulated mathematical expression of BER with time-slot code overlapping ratio, chaotic phase and dominant system noise
  - Experimentally tested code misalignment tolerance for both 4-QAM and 16-QAM modulation formats and compared the experimental and analytical results

Chapter 6

- Analysed optical beam waists and the respective maximised error-free coverage for various data rate in demand
- Investigated impacts of transmitted optical power and laser noise on system performance
- Investigated impacts of transmission channel and detection on system performance
- Analysed and compared code misalignment tolerance results of multiple access system with and without secure capability for multiple data rates.

1.4 Publications

Journal Publications

1. T. Liang, K. Wang, C. Lim, E. Wong, T. Song, and A. Nirmalathas, "Time-slot coding scheme for multiple access in indoor optical wireless communications", *Optics Letters*, vol. 41, no. 22, 5166 – 2169, Nov. 2016.

2. T. Liang, K. Wang, C. Lim, E. Wong, T. Song, and A. Nirmalathas, "Time-slot Coding Scheme with Adaptive Loading Function for Multiple Access in Indoor Optical Wireless Communications", *Journal of Lightwave Technology*, vol. 35, no. 18, 4079 – 4086, July 2017.

3. T. Liang, K. Wang, C. Lim, E. Wong, T. Song, and A. Nirmalathas, "Secure multiple access for indoor optical wireless communications with time-slot coding and chaotic phase", *Optics Express*, vol. 25, no. 18, 22046 – 22054, Sep. 2017.

4. K. Wang, A. Nirmalathas, C. Lim, T. Song, T. Liang, K. Alameh, and E. Skafidas, "Short-range optical wireless communications for indoor and interconnects applications", *ZTE Communications*, vol. 14, no. 2, 13 – 22, 2016

Conference Publications

1. T. Liang, K. Wang, C. Lim, E. Wong, T. Song, and A. Nirmalathas, "Experimental demonstration of time-slot coding scheme for multiple access in high-speed optical wireless communications with imaging receiver", in *Proc. of Conference on Lasers and Electro-Optics Pacific Rim/Opto-Electronics and Communications Conference/Photonics Global Conference (CLEO-PR/OECC/PGC)*, Singapore, July 2017.

2. T. Liang, K. Wang, C. Lim, E. Wong, T. Song, and A. Nirmalathas, "Robust and secure indoor optical wireless communications supporting multiple users", *Optical Fiber Communication Conference and Exhibition (OFC)*, San Diego, California, March 2018, pp. M3K.6.

3. A. Nirmalathas, K. Wang, C. Lim, E. Wong, E. Skafidas, K. Alameh, T. Song and T. Liang, "Multi-gigabit indoor optical wireless networks – feasibility and

challenges", in *Proc. of IEEE Photonics Society Summer Topical Meeting Series (SUM)*, Newport Beach, California, July 2016, pp. 130 – 131.

4. K. Wang, S. Gao, Y. Wang, T. Song, T. Liang, A. Nirmalathas, C. Lim, K. Alameh, and E. Skafidas, "Short-range infrared optical wireless communications – systems and integration", in *Proc. of IEEE Photonics Society Summer Topical Meeting Series (SUM)*, Newport Beach, California, July 2016, pp. 152 – 153.

5. T. Song, K. Wang, A. Nirmalathas, T. Liang, E. Wong, J. Ma, "High-speed optical wireless personal area communication system supporting multiple users", in *Proc. of IEEE Photonics Conferences (IPC)*, Waikoloa, Hawaii, October 2016, pp. 297 – 298.

6. K. Wang, T. Song, T. Liang, A. Nirmalathas, C. Lim, K. Alameh, and E. Skafidas, "A dual-infrared-transmitter optical wireless based indoor user localization system with high accuracy", in Proc. of Optical Fiber Communication Conference and Exhibition (OFC), Los Angeles, California, March 2017, pp. 1 – 3.

7. A. Nirmalathas, T. Liang, S. Edirisinghe, C. Lim, E. Wong, K. Wang, and K. Alameh, "Highspeed optical wireless communications for local area networks – invited", accepted in *Proc. of Conference on Opto-Electronics and Communications Conference (OECC)*, Jeju, Korea, July 2018.

8. A. Nirmalathas, T. Liang, S. Edirisinghe, T. Song, K. Wang, C. Lim, E. Wong, C. Ranaweera, and K. Alameh, "Communicating with light wirelessly: towards an optical wireless future – invited", submitted in *Microwave Photonics (MWP) Symposium*, Matsue, Japan, 2018.

Chapter 2 Literature Review

2.1 Introduction

With the growing penetration of high-performance personal communication devices such as smartphones, tablets and ultrabooks, which are capable of supporting the ever-growing bandwidth intensive applications such as high-definition video streaming and real-time video transmission, the volume of data traffic exchanged in the immediate vicinity of our personal spaces has increased explosively in the last five years [1, 2]. Other emerging network applications including tactile communications, which supports transmitting real-time touch and actuation to revolutionise our daily life [9, 10], virtual reality (VR) and augmented reality (AR), also necessitate high throughput and low latency communications for truly immersive experiences [11-13]. Consequently, there has been a significant increase in the demand of high-speed wireless communications in personal areas, such as working and living spaces. In this respect, the optical wireless communication technology has attracted considerable interests in the field of indoor high-speed communications. Compared to other competing technologies including ultra-wideband (UWB), millimetre-wave (mm-wave), and Wi-Fi, optical wireless communications (OWC) systems benefit from the ability to exploit a huge amount of unregulated bandwidth. In addition, OWC systems have the capability of eliminating the interference with other radio frequency (RF) systems and are capable of serving areas where RF have harmful effects such as in hospitals and in airplanes [14]. Furthermore, optical waves cannot penetrate objects like walls in the transmission path due to their short wavelengths. While this characteristic limits the coverage range, a narrow optical beam provides physically secure communications within the immediate

vicinity of working and living spaces. Consequently, an effective multi-user access scheme with robust security support for indoor OWC systems is still elusive whilst high data rate has been achieved.

A comprehensive review on the related literature is provided in this chapter, which is organised as follows:

Section 2.2 first provides a brief discussion about several candidates that are suitable for short-range wireless applications, including Wi-Fi, mm-wave, UWB and OWC systems. Together with the advantages of OWC, previous studies of OWC with single channel transmission are also reviewed in this section, including the comparisons amongst different optical sources and system configurations and challenges in OWC systems. Since multi-user scenario for practical applications has attracted considerable attention, traditional multiple access techniques in both electrical and optical domain are introduced in Section 2.3. Previous studies of adaptive loading techniques to improve system flexibility of multiple access networks are also reviewed. In addition to the need of high-speed wireless multi-user connections, it is also significant to provide each user with a private and secure communication link. Therefore, in Section 2.4, the previous research on communication security, especially in the systems that support multiple user access, is further summarised and discussed.

2.2 High-speed Indoor Communication Systems

As mentioned in the previous section, there are massive demands for high-speed communications in personal area such as working and living spaces. Compared with providing connectivity in personal area networks via wired physical connections such as copper cables and optical fibres, wireless communication system is superior due to the capability of offering the mobility feature. Communication systems based on Wi-Fi, mm-wave, UWB and optical wireless are reviewed and summarised in the following subsections.

2.2.1 Wi-Fi systems

Wi-Fi has been widely deployed in the indoor scenarios to replace the Ethernet cable over the past decades all over the world, which provides relatively high speed connections between electronic devices and network. The conventional Wi-Fi systems occupying 2.4 GHz and 5 GHz frequency bands are standardised in IEEE 802.11 Wireless Local Area Networks (WLANs) standards. The development of physical layer specifications in IEEE 802.11 for Wi-Fi networks is summarised in Table 1 [15-20].

802.11 Protocol	RF Region	Channel Bandwidth	No. of Streams	Maximum Data Rate
a	5 GHz	20 MHz	1	54 Mb/s
b	2.4 GHz	22 MHz	1	11 Mb/s
g	2.4 GHz	20 MHz	1	54 Mb/s
n	2.4 GHz & 5 GHz	20 & 40 MHz	4	600 Mb/s
ac	5 GHz	20, 40, 80 & 160 MHz	8	3.47 Gb/s
ax	2.4 GHz & 5 GHz	Not specified	No specified	10.53 Gb/s

Table 1 IEEE 802.11 physical layer standards summary

The longer wavelength signals employed in the 2.4 GHz Wi-Fi technology are able to travel farther compared to those in 5 GHz solutions. However, it is more likely to interfere with other devices using the same frequency band such as microwave ovens, blue-tooth devices and so on [21]. What is more, the available bandwidth in the 2.4 GHz band is limited to around 20 MHz. Employing broader channel bandwidth in the 5 GHz frequency band provides opportunity to further improve the system data rate. In the later versions from IEEE 802.11ac, the 5 GHz band together with multiple-input multiple-output (MIMO) technique makes gigabit transmission possible, where multiple antennas are equipped at both transmitter and receiver sides to transmit spatially divided signal streams simultaneously. In addition to the multiple-antenna

system, higher order modulation formats like 256-QAM (Quadrature Amplitude Modulation) is adopted in IEEE 802.11ac to boost the system throughput [22]. The standard of IEEE 802.11ax is expected to achieve 10.53 Gb/s by the end of year 2018 by using MIMO with orthogonal frequency division multiplexing (OFDM) technique (MIMO-OFDM) [23]. However, the number of antennas installed at the receiver side is restricted by the size of device and employing advanced modulation formats such as 256-QAM and OFDM increases the complexity of signal processing at both transceiver sides.

2.2.2 Millimetre-wave Systems

As discussed in the last section, the conventional Wi-Fi system employing 2.4 GHz and 5 GHz radio frequency bands confront the serious problem of spectrum scarcity, which drives the trend of using high frequency spectrum in the millimetre-wave range. Millimetre-wave using the 60 GHz band is another attractive technology for short-range communications with the ability to achieve gigabit-per-second (Gbps) range speed. Millimetre-wave systems are supported by the development of WLAN standards, i.e. the IEEE 802.11ad and IEEE 802.11ay [5, 24, 25]. Fig. 2.1 shows the allocation of 60 GHz band in selected countries.

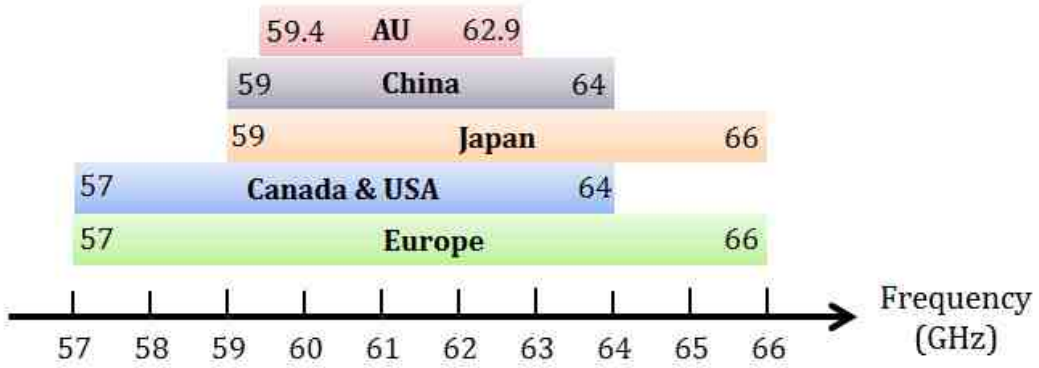

Fig. 2.1 Spectrum allocation around 60 GHz

As shown in Fig. 2.1, there is approximately 7 GHz bandwidth available. One major advantage of 60 GHz mm-wave systems is that the corresponding radio frequency components including antennas are more compact due to the short wavelength (~ 5 mm)

[26]. This remarkable feature allows the entire transceiver to be integrated onto one millimeter-sized chip and thus, makes massive MIMO achievable using the complementary metal oxide semiconductor (CMOS) technology for next-generation communication networks [27-29]. High data rate of up to 21 Gb/s 60 GHz transmission has been experimentally achieved over 1-meter wireless link with the help of 512-QAM-OFDM in [30]. Furthermore, a frequency-interleaved architecture has been employed in the 60 GHz CMOS transceiver for IEEE 802.11ay to realise 42.24 Gb/s transmission [31].

However, the propagation loss of mm-wave in the free space is much higher compared to lower RF bands. Since the free-space path loss scales as $1/\lambda^2$ (λ is the carrier wavelength), 60 GHz links have 21.6 dB higher loss than 5 GHz and 28 dB higher loss than 2.4 GHz band [32]. What is more, mm-wave generation and distribution is complex and challenging [33-35]. The mm-wave over fibre could be one of possible solutions to facilitate the signal distribution, however, the high-bandwidth optoelectronic devices such as modulators and photodiodes are required in such systems [36, 37]. Digitised radio-over-fibre (RoF) is also proposed for mm-wave signal distribution, whilst the performance is restricted by the bandwidth of analog-to-digital convertor (ADC) and digital-to-analog convertor (DAC) or the electronic sampling systems in practical implementation [38].

2.2.3 Ultra-wide Band Systems

The Federal Communication Commission (FCC) issued the first report and order (RAO) related to ultra-wideband (UWB) systems in 2002 and allocated the unlicensed band from 3.1 – 10.6 GHz for UWB applications [3]. Although the UWB spectrum allocation is diverse worldwide, the maximum mean equivalent isotropic radiated power (EIRP) for UWB transmitter or the transmitted power spectrum density (PSD) is limited to less than – 41.3 dBm/MHz [4]. This is designed to avoid interference as UWB systems employ a broadband spectrum to carry signals and share the RF spectrum with other existing standards. The spectrum allocation and corresponding PSD are illustrated in Fig. 2.2. In previous studies, a bit rate of 500 Mb/s with one metre transmission distance has been achieved with the help of a spectrum-efficient frequency hopping (FH)

technique [39], where the link propagation distance is restricted by the low transmitted signal power [40].

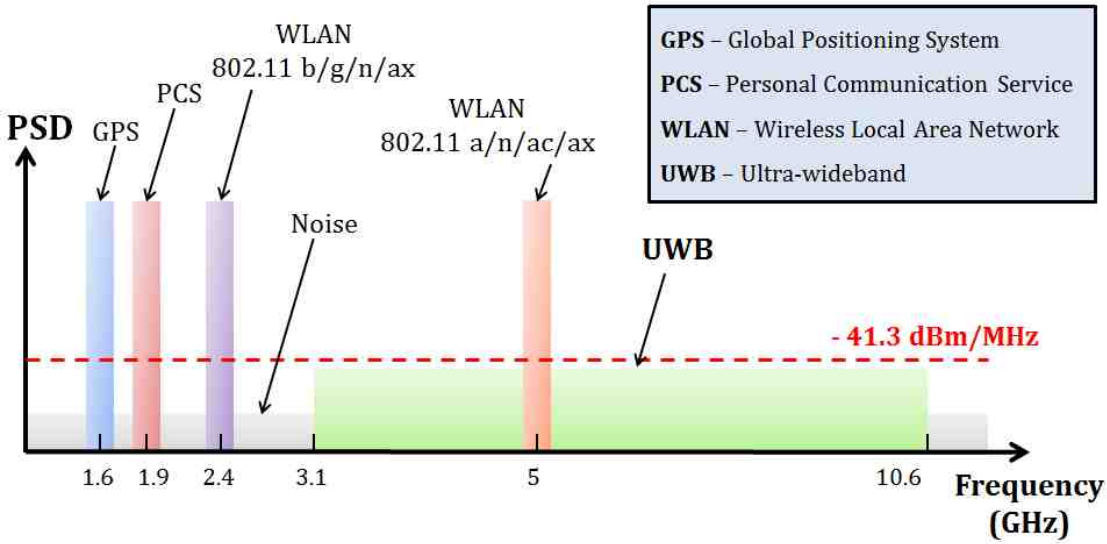

Fig. 2.2 UWB spectrum with other conventional standards

In order to extend the transmission distance, UWB over fibre transmissions have been widely investigated. Authors in [41] have recently proposed an adaptive UWB communication system for multiple users to meet the high data rate requirement in 5G wireless communications, where both optical frequency combs and multiband OFDM are employed. Experiments have been carried out for 15 users over 50 km standard single-mode fibre transmission and the maximum data rate of 5.343 Gb/s has been achieved. However, in addition to the complex system involving multiple external modulators, optical amplifiers, and wavelength-selective switch (WSS), there is no free-space transmission demonstrated. To the best of our knowledge, a new record of UWB wireless transmission has been made in [42] by employing 8 bands UWB signal modulated with carrierless amplitude phase (CAP) modulation format. A 10 Gb/s transmission over 3.5 m has been achieved while complying with FCC standard. However, there is a trade-off between the achievable data rate and the link propagation distance while complex signal processing techniques are normally required to achieve high data rate in UWB systems.

2.2.4 Optical Wireless Communication Systems

In addition to Wi-Fi, mm-wave and UWB systems as reviewed above, the optical wireless communications (OWC) system has emerged as a promising technique to provide high speed wireless connections for indoor applications, in conjunction with today's well-developed fibre based broadband access networks. A summary table is provided as below to explicitly illustrate a comparison between RF techniques and OWC techniques regarding the aspects of frequency spectrum availability, signal processing complexity, immunity to EMW and line-of-sight blockage.

	Frequency Spectrum	Signal Processing	Immunity to EMW	line-of-sight blockage
RF techniques	scarce	complex	No	low
OWC techniques	huge amount	simple	Yes	high

In OWC system, the optical radiation with huge unregulated bandwidth is firstly distributed through optical fibre and then transmits in the free space [43]. Fig. 2.3 illustrates the block diagram of typical optical wireless communication systems with externally modulated optical sources.

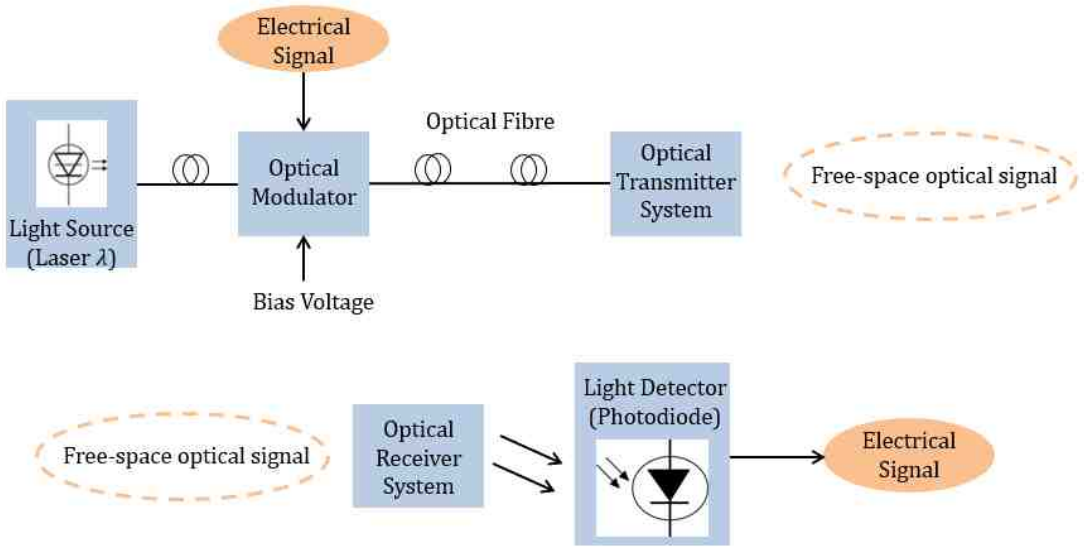

Fig. 2.3 Typical optical wireless communication system

The light source is modulated with electrical data either directly or externally and the light wavelengths range from ultra-violet (UV) to infrared as shown in Fig. 2.4. The utilisation of visible light as the light source, also known as visible light communication (VLC) has drawn a lot of attention from both academic and commercial sides due to the low cost of light emitting diodes (LED) compared to laser diodes (LD) [44]. It can also provide the illumination function simultaneously with data communications and it is generally considered as eye-safe [45].

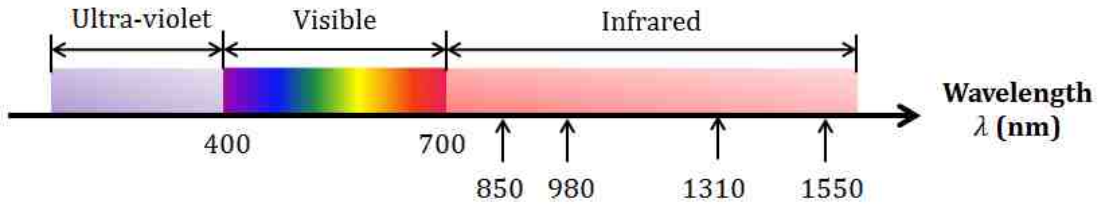

Fig. 2.4 Light source spectrum

However, the modulation bandwidth and electrical-to-optical (E/O) conversion efficiency are the key factors that limit the performance of VLC systems. Complex signal processing such as OFDM [46, 47], MIMO [48, 49], pre-equalisation and post-equalisation techniques [50, 51] are necessary to boost the VLC system capacity. In addition, the compatibility with the normal illumination function needs to be considered as well [52], where the illumination level might have negative impacts on the communication capability, especially for the VLC systems employing intensity modulation and direct detection (IM/DD) [53, 54]. Consequently, dimming control techniques need to be implemented in VLC applications [55-57].

Instead of using LED, LD is preferable over LED due to the approximately 1000 times higher modulation bandwidth and more than 3 times higher E/O conversion efficiency [44]. Comparison now goes to ultraviolet optical source and infrared optical source, where damage to human eye and skin from the ultraviolet radiation is more likely than from longer infrared wavelength [58]. The optical source in the infrared band is therefore considered in this thesis.

Before being transmitted in the free space, the optical signal normally passes through an optical system at the transmitter side, which is employed to control the optical radiation power and direction. After travelling through a certain free space distance,

another optical system is used at the receiver side, which typically contains an optical filter to limit the ambient light noise and lenses to concentrate the input light. Then the optical receiver such as a photodiode converts the optical signal into the electrical domain for further detection or offline post-processing [59].

The most notable advantage of the optical wireless communication technology is the huge amount of unregulated bandwidth. The high-speed communication in the Gbps range can be easily achieved even with simple modulation formats such as On-Off Keying (OOK). Error-free (BER < 10^{-9}) transmission of downlink 200 Gb/s (5×40 Gb/s) has been successfully demonstrated over 2.39 km single mode fibre and 2 m free space link with the help of wavelength division multiplexing (WDM) technology and an integrated cascaded aperture optical receiver in [60]. Bi-directional transmission with 3 m wireless link with the maximum aggregate bit rate of 224 Gb/s has been achieved with digital coherent WDM and wide field-of-view (FOV) at both transmitter and receiver, where liquid crystal spatial light modulators (SLMs) are employed [61]. With the demonstrated high data rate, the OWC technology has great potential in real-time applications which require high speed data transmission and low latency. In addition, OWC systems can eliminate the interference with other radio frequency (RF) systems. With its immunity of electro-magnetic wave (EMW), the OWC technology can also be deployed in circumstances where RF signal causes harmful effects such as in hospitals since some RF signals interfere with medical electronic devices [14], and in airplanes.

In terms of link configuration in OWC systems, there are generally two major types. One of the solutions is the line-of-sight (LOS) link and the other is the diffused link [62]. As shown in Fig. 2.5 – (a), the LOS scheme builds a point-to-point communication link with a narrow optical beam. The performance does not suffer from multi-path distortion [63], which enables high-speed communications with high energy efficiency. However, it requires a precise alignment between transmitter and receiver and precise localisation with tracking system is needed to provide connections and mobility to terminal users. In addition, this LOS configuration fails to provide multi-user services and is vulnerable to any blockage in the transmission link.

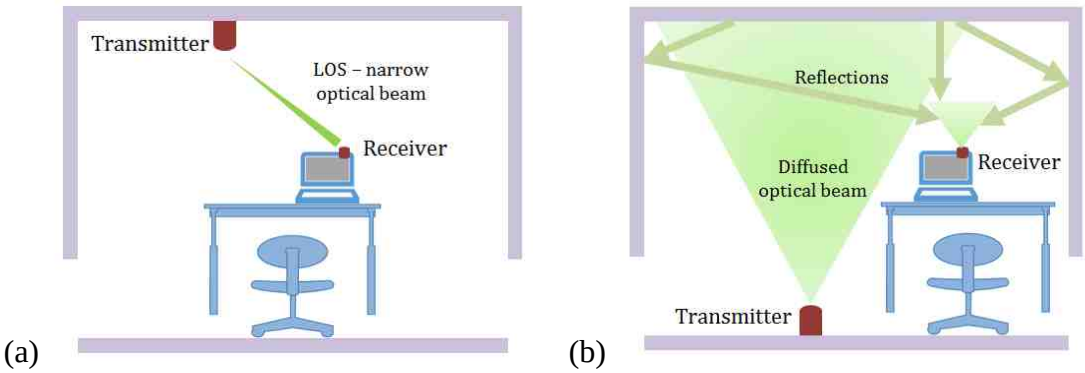

Fig. 2.5 Two typical link configurations of indoor OWC systems: (a) LOS link and (b) diffused link

Fig. 2.5 – (b) illustrates a typical diffused link based system. A divergent beam is emitted from the transmitter and it is reflected back to the receiver by surroundings such as walls, ceilings and the floor. It improves the system robustness and minimises the effect of shadowing [64]. The diffused link configuration also enables for point-to-multipoint services as the coverage of the entire room can be realised to provide sufficient mobility to end users. However, the performance of this diffused scheme is intuitively degraded by the multi-path dispersion, the relatively low energy efficiency, and the ambient noise.

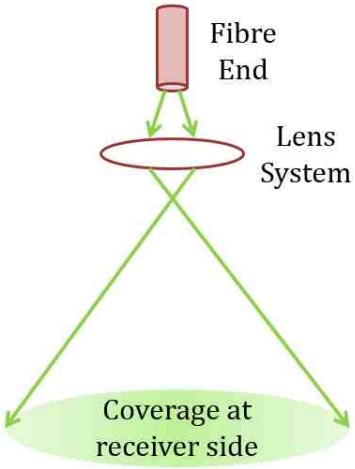

Fig. 2.6 Transmitter structure with LOS expanded optical beam

Consequently, a hybrid configuration employing a LOS expanded optical beam has been proposed in [65, 66] to offer both high-speed communication (> 10 Gb/s with OOK) as well as limited mobility. The structure of the fibre transmitter is illustrated in

Fig. 2.6, where a lens system is employed to expand the optical beam from the fibre end so that a certain area can be covered at the receiver side. The multipath dispersion study has shown that multipath dispersion is negligible with this scheme, and multiple users within the coverage can be served with mobility [65].

2.3 Multiple Access Techniques

In previous studies, high-speed optical wireless communications for single user access have been extensively investigated. Providing services for multiple users in indoor OWC systems requires more attention and better solutions in practical implementations. The multiple access techniques and the techniques for adaptive loading amongst multiple users are described and reviewed in this section.

2.3.1 Electrical Multiple Access Techniques

In relation to achieving multi-user access through electrical domain, multiple access can be achieved similarly to RF systems by employing specific multiplexing techniques such as time-division multiple access (TDMA), frequency-division multiple access (FDMA), code-division multiple access (CDMA) or the combination of them. The fundamentals of the aforementioned conventional multiple access techniques are illustrated in Fig. 2.7.

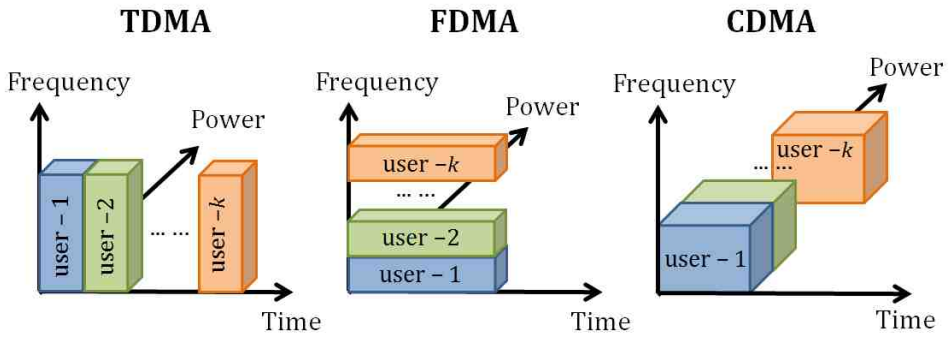

Fig. 2.7 Illustrations of TDMA, FDMA and CDMA

In optical-CDMA (OCDMA) system, optical orthogonal codes (OOC) are generally applied to spread signal spectrum and thus allow multiple users to share the same channel simultaneously [67]. The Walsh-Hadamard (WH) codes have been adopted in [68] to support up to 10 users each with 3 Mb/s data rate. However, experimental results have shown that the BER performance degrades with increasing number of users in the system. Random optical codes (ROC) can be also employed with additional processing techniques such as shifting the code bit [69], however, it generally requires codes with long lengths and thus complicate signal processing. The achievable data rate in [69] is only 1.67 Mb/s for total 20 users each with a 50-bit code.

For FDMA system, each user is assigned with a unique frequency band with no overlapping to ideally eliminate the multi-user interference (MUI) [70]. It is also termed as subcarrier multiplexing (SCM). Authors in [71] have demonstrated OWC system with SCM technique to support 2 users with larger space (10 GHz) between the RF carrier of each user and an aggregate bit rate of 5 Gb/s (2 × 2.5 Gb/s). A 6 GHz bandwidth Fabry-Perot interferometer based optical bandpass filter is employed to select a specific subcarrier at each user terminal. However, the performance is restricted by the narrow band optical filter and the bandwidth requirement of optoelectronic devices including modulators and photodetectors.

Another possible solution to achieve multiple access is the multi-carrier code-division multiple access (MC-CDMA) technique, which intrinsically is a combination of OFMD and CDMA, as reported in [72]. With such a scheme, 16 users have been supported with the help of unique orthogonal 16-bit code and 128 subcarriers for each user, and the overall bit rate has been successfully demonstrated as 750 Mb/s over 1.5 m free space transmission. As the scheme involves complex processing at both transmitter and receiver sides such as parallel-to-serial (P/S) and S/P, adding and removing cyclic-prefix, Fast Fourier Transform (FFT) and inverse FFT (IFFT), it increases the system complexity, overall system size and cost, hindering the commercial use in the future.

Due to the fact that high signal-to-noise ratio (SNR) is always challenging to achieve in OWC systems, TDMA technique, which assign different time slots to different users, is favoured compared to the other two conventional electrical multiplexing techniques, i.e. FDMA and CDMA, due to its higher power efficiency, according to [73]. Authors

in [74] have experimentally demonstrated a point-to-point link with 2 m free space link to support up to 10 users. An aggregate bit rate of 4 Gb/s has been achieved with TDMA based on 16-CAP modulation format. However, the synchronisation requirement at the receiver side is strict for a specific end user to obtain the corresponding signal. It is particularly challenging in high-speed transmissions for next-generation communication systems.

In addition to the conventional electrical multiple access techniques as discussed above, which assign orthogonal resource blocks (time slots in TDMA, frequency bands in FDMA and spreading codes in CDMA) to multiple users in order to eliminate the MUI, another promising technique named as non-orthogonal multiple access (NOMA) has attracted considerable attention [75-77] due to its remarkable spectral efficiency. One of the key ideas in NOMA technique is power domain multiplexing, which allocates different power levels to different end users while transmitting their message in the same time slot and frequency band [78]. As shown in Fig. 2.8, NOMA normally allocates the highest power to the user with the poorest channel condition and vice versa while maintains the total power constant.

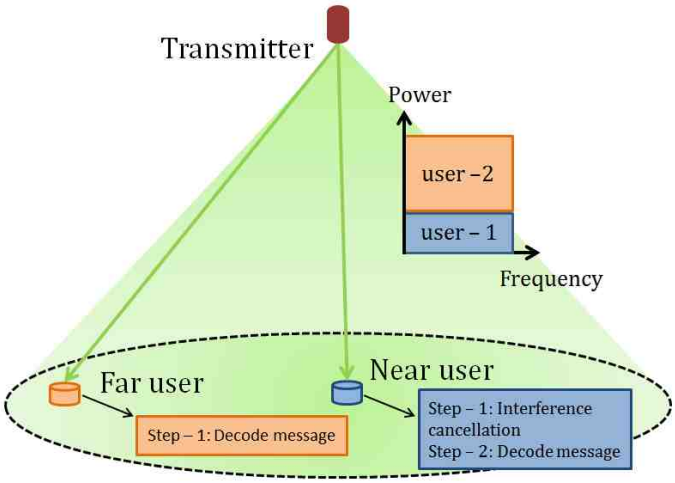

Fig. 2.8 The simplest example of 2 users with NOMA technique

In terms of the decoding part at each user terminal, the user allocated with the highest power decodes its message straight away by treating others' signal as noise. On the other hand, the near user (referred to user-1 in Fig. 2.8) requires to first decode the far user's (user-2's) message and then subtracts it, which is termed as successive

interference cancellation (SIC), to further decode its own message. Although it improves system fairness and spectral efficiency, the system complexity at the receiver side increases with the increasing number of end users [79, 80]. In addition, the error propagation during the process of SIC degrades the system performance, which is more serious when more users are served [81]. In the meantime, SIC also leads to significant delay in acquiring the corresponding data and the lack of communication security.

2.3.2 Optical Multiple Access Techniques

In addition to the multiple access techniques from the electrical side, wavelength-division multiplexing (WDM), space-division multiplexing (SDM), polarisation-division multiplexing (PDM), and orbital angular momentum (OAM) multiplexing are promising multiple access implementations from the optical side. Authors in [82] have experimentally demonstrated SCM-WDM visible light communications for multiple users, where different optical wavelengths are employed to provide communication services for different users. Downlink transmission with BER < 3.8×10-3 has been achieved for 4 users with 575 Mb/s aggregate bit rate. However, in the overlapping area at the receiver side which is covered by more than two wavelengths, the interference from other users is still an issue. The performance is also limited by the narrow bandwidth of optical band-pass filter. As another optical multiplexing technique, SDM is able to angularly transmit multi-user signal and thus requires angular diversity receivers at each user terminal to diminish the interference, which intuitively increases system complexity [83, 84].

Modulating independent messages onto different polarisation states has been reported to improve the spectral efficiency, and multiple access could be achieved by serving a specific user with a certain polarisation state [85-87]. However, the PDM system performance is significantly dependent on the accurate alignment of polarisation between transmitter and receiver [88]. What is more, coherent detection with equalisation is generally required for PDM system to alleviate polarisation mode dispersion (PMD) [89, 90].

Furthermore, by employing light with Laguerre-Gaussian (LG) mode, orbital angular momentum has been reported as another degree of freedom for multiplexing at the optical side, which can be employed to either increase the system capacity or provide

multi-user services [91-93]. Ten OAM modes have been generated and transmitted over a free-space distance of 0.6 m to serve multiple users in [94], where each OAM mode carries 20 Gbaud quadrature phase shift keying (QPSK) modulated signal. The OAM multiplexing is capable of being integrated with other conventional multiplexing techniques including TDM, FDM, WDM, SDM and PDM, irrespective of any baseband modulation format [94]. However, the performance of OAM multiplexing system is affected by atmospheric turbulence, which leads to the transfer of part of the energy of one OAM mode to another mode [95]. In addition, it requires sophisticated setup to either generate OAM states or efficiently separate different OAM states at the detection side [96-98].

2.3.3 Adaptive Loading Techniques

In order to increase the system flexibility, several adaptive loading techniques have been widely investigated for single transmitter system [99-101]. In multi-user OWC networks, it is also more realistic and efficient to provide multiple data rates to users with diverse demands and priority levels while maintaining satisfactory service coverage with limited transmitter power level [102].

In the frequency domain, the discrete multitoned (DMT) modulation technique is generally employed with the multi-carrier technique such as OFDM in the system with non-flat frequency responses. The idea of DMT is to finely optimise the modulation format and/or electrical power of each sub-carrier according to a specific frequency-selective channel, in order to overcome the frequency response roll-off effect and to maximise the system capacity for a single terminal [103-105]. Experimental results in [106] have demonstrated that the employment of OFDM with DMT technique in VLC system is feasible of maximizing the system throughput beyond system 3 dB bandwidth limitation. Nevertheless, it requires accurate channel state information (CSI) at the receiver, which increases the overhead in the uplink.

Another technique to achieve adaptive data rate is time-division hybrid modulation formats (TDHMF) which periodically alternates two modulation formats in the time domain [107]. In addition to system capacity improvement, the TDHMF technique is typically employed to accommodate dynamic data traffic volumes and to extend transmission reach in long-haul transport networks [108]. Up to 1.15 Tb/s has been

successfully demonstrated with the spectral efficiency of 7.68 b/s/Hz over 500 km fibre transmission by employing time-division hybrid QAM signals including QPSK, 8-QAM and 16-QAM [109]. This technique has been extended in a 2 × 2 MIMO VLC system where 2 users are equipped with maximum likelihood detectors [110]. Simulation results have shown that the BER of both users can be minimised by adapting the transmitted symbol constellations, which results in optimizing the transmission power of two light sources. However, the constant switching between two modulation formats and the synchronisation can be problematic in practice. The delay in feedback significantly degrades the system performance.

Another technique named rate adaptive coding (RAC) has abilities to adapt the spectral efficiency and data rate by varying code redundancy with fixed or variable constellations [111]. In order to maximise the achievable data rate while maintaining satisfactory BER requirement in optical fibre transmission systems, authors in [112] proposed an algorithm to adapt the forward error correction (FEC) code rate by observing the received SNR or BER. However, it requires more complex implementations and the net data rate is sacrificed compared to TDHMF with the same bandwidth [108]. In addition to the aforementioned techniques, seamless rate adaption technique using rate compatible modulation formats is proposed to provide continuously variable bit rate and smooth spectral efficiency [113]. However, the decoding algorithm requiring iterative process increases the computational complexity [114].

2.4 Secure communications

It is widely known that OWC has the ability to offer secure communications physically since an optical wave with short wavelength cannot penetrate objects such as walls in its transmission path [73]. However, this assumption is only valid in the immediate vicinity of very narrow optical beams. Communication security in OWC systems, especially those supporting multiple user access, has yet to be widely studied. When

multiple users are covered with a single but wider optical beam, security issues arise, such as eavesdropping, tampering, imitation, forgery, etc [115]. Our focus in this study is on alleviating eavesdropping, which is one of the most widely existing issues in multi-user telecommunication systems.

In previous studies, nulling strategies have been proposed in [116] for free space optical communications whereby illegal interception is prevented by controlling both amplitude and phase from each element of a transmitter array to realise destructive interference at locations where potential eavesdroppers may locate. However, to employ this null steering method, knowledge of locations of potential illegal users are required. What is more, security problem still exists for users located in the constructive interference area.

Without the knowledge of an eavesdropper's channel state information (CSI), artificial noise is added in the intended user's null-space to degrade the received signal-to-noise ratio (SNR) of eavesdropper [117]. However, by using this method, users in the null area cannot be served due to low SNR.

In [118], a chaotic-CDMA based visible light communication (VLC) system has been proposed for multiple access whereby spreading codes in CDMA system are generated based on chaotic sequences. Since the code length is limited, security has be further enhanced by employing advanced encryption standard (AES) to interleave the spread information. However, this technique incurs additional bandwidth and complex computation. Further, simulation results show degradation in BER performance with increasing number of users.

In terms of using chaotic sequence to provide secure connections, the authors in [119] have employed a chaotic series of elements that locate between -1 and 1 and applied a sign function to this sequence to obtain a new sequence of discrete values with only -1 and 1. The new sequence is applied to *I* and *Q* components of each OFDM carrier in passive optical networks (PONs). A power gain of 0.3 dB has been achieved with 16-QAM due to the coding, however, the coded symbol data can only have four possible patterns including its original version and it is relatively less resistive to brute force or exhaustive computation.

Furthermore, some quantum based solutions including Quantum Key Distribution (QKD) methods are able to provide ultimate security due to the non-cloning theorem

and the fact that any disturbance will result in quantum state collapse [120, 121]. However, quantum based methods are much more complicated to implement in indoor OWC systems currently, and one of the reason is the challenge of realising single photon sources and single photon detectors. At the time of writing, there are limited studies addressing the security issue for indoor OWC systems supporting multiple access.

2.5 Conclusions

In this chapter, several techniques which are promising to support the ever-growing bandwidth intensive applications for indoor scenarios, including Wi-Fi, millimetre-wave, ultra-wide band and optical wireless communications systems, have been comprehensively reviewed and summarised. With the outstanding features of huge amount of unregulated bandwidth and immunity to EWM signals, different types and configurations of OWC system have been discussed in Section 2.2.4. In our work of infrared laser based indoor OWC system, a hybrid configuration with a LOS expanded optical beam is employed for theoretical analysis and experimental demonstration. In addition to high data rates, multiple access with flexibility is also crucial for practical OWC deployment. Both multiple access techniques and adaptive loading techniques have been reviewed in Section 2.3. Furthermore, although OWC system is widely acknowledged with the capability of providing physically secure telecommunications due to the short wavelength of optical wave, such security is only valid for point-to-point links where narrow optical beams are employed. For multi-user accessed OWC system where a wide optical beam is deployed to connect multiple users, the security issue is still relatively elusive to date. The limited literature has been reviewed in Section 2.4.

Chapter 3 System Model for Indoor Optical Wireless Communications with Square QAM

3.1 Introduction

With the huge amount of unregulated bandwidth and immunity to electro-magnetic waves, the optical wireless communications (OWC) technology has been widely acknowledged as a promising candidate to provide high-speed wireless connections [7]. The analytical model for OWC channel has been widely studied to perform general system analysis. The theoretical model of bit error rate (BER) with On-Off Keying (OOK) for indoor OWC with single user access is built in [122] by using the conventional co-error function. In [123], the system BER is derived using photon-counting approach in the presence of shot noise to study the performance of multiple-input multiple-output (MIMO) underwater wireless optical communication (UWOC) systems with OOK modulation. In order to achieve high spectral efficiency, advanced modulation formats, such as Quadrature Amplitude Modulation (QAM), are employed in [124] with micro electro mechanical systems (MEMS) based single channel imaging receiver (SCIR). The analytical BER in terms of signal SNR is conventionally presented using co-error function. However, only the noise from natural and artificial light is considered. The derived BER in [124] is only valid for signal with additive white Gaussian noise (AWGN) channel and does not have potential to be manipulated to fit with other interfered signal.

Instead of using the conventional method to calculate SER and BER, we first derive the SER equation based on the received signal constellation with the intended original symbol and the standard deviation of the noisy received symbols. The standard

deviation is related to the signal SNR after transmission and detection in indoor OWC system. The models of major noise sources from optical source, channel and detector, including intensity noise, background light induced noise and preamplifier induced noise, are provided to calculate the standard deviation. Lastly, the BER is linked with SER by finding the relationship between BER and SER. Both the standard deviation and BER are measured in indoor OWC experiments based on 1.25 Gb/s – 5 Gb/s 4-QAM modulation format and 2.5 Gb/s – 10 Gb/s 16-QAM modulated system. A satisfactory agreement is achieved between experimental and analytical results, the latter calculated from the derived system model. As importantly, the system analytical model developed in this chapter has the potential to be modified and thus provide fundamentals for theoretical analysis in the following chapters.

The rest of this chapter is organised as follows:

Section 3.2 describes the general system architecture of a typical indoor optical wireless communications system with square QAM modulation format, including both off-line processing and free space transmission configuration. In Section 3.3, a comprehensive analytical model is presented with symbol error rate, standard deviation and bit error rate. Finally, the experimental setup used to demonstrate and verify the proposed system model is presented in Section 3.4, followed by extensive comparisons between experimental and analytical results.

3.2 System Architecture

The block diagram of a typical square QAM based indoor optical wireless communications system is described in Fig. 3.1. A sequence of binary bits is first generated in the central office (CO) and then mapped into symbol patterns based on a certain square M-ary QAM modulation format ($M = 2^{2l}$, where l is a natural number, i.e. 1, 2, 3, etc.). The symbol sequence travels through a raised-cosine pulse shaping filter

which is responsible for up-sampling and for controlling the inter-symbol interference. The signal before up-conversion is denoted as s_m and expressed as:

$$s_m = \sum_{j=-\infty}^{\infty} v^j h\left(m - jT_s\right) \tag{3.1}$$

where v is the symbol sequence before the pulse shaping filter, $h(m)$ is the pulse shaping function and T_s is the symbol period. The baseband QAM signal is then up-converted to a carrier frequency f_c to form a series of passband signals. After digital-to-analog conversion (D/A), the electrical signal modulates the laser source via an external modulator.

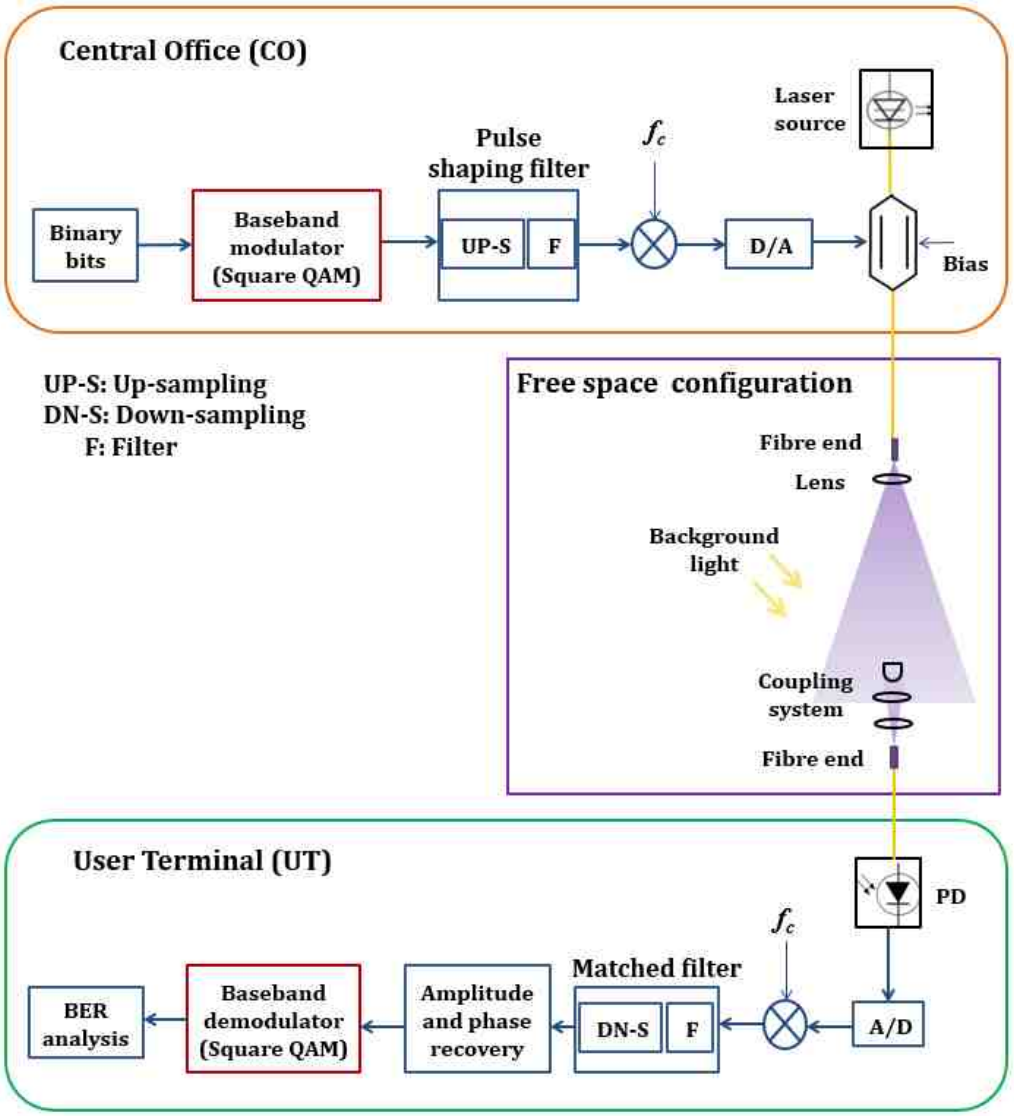

Fig. 3.1 Block diagram of a typical indoor wireless communications system with square QAM modulation format.

In a typical indoor free space configuration, a lens is placed after the single mode fibre end at the transmitter side. The distance between the fibre end and the lens can be adjusted to form an optical beam with a certain beam width at the receiver side. Since the output of the single mode fibre has a close approximation of Gaussian intensity profile [125], the equivalent beam focal length is denoted as f in order to decide the beam waist at the receiver plane:

$$f = \frac{\pi\omega_0^2}{\lambda} \tag{3.2}$$

where λ is the wavelength of laser source. The original beam waist at the output beam plane of the fibre end is denoted as ω_0, which is reasonable to be estimated as the radius of the standard single mode fibre (5.2 μm) [126-D.P65-[15]].

The new Gaussian beam waist after a lens with a focal length of f' is expressed as:

$$\omega_0' = \frac{\omega_0}{\sqrt{\left(1-\frac{L}{f'}\right)^2 + \left(\frac{f}{f'}\right)^2}} \tag{3.3}$$

where L is the distance between the fibre end and the lens. After travelling through the lens, the optical beam remains Gaussian and the beam waist at the receiver plane can be calculated as:

$$\omega'(z) = \omega_0' \sqrt{1+\left(\frac{\lambda z}{\pi\omega_0'}\right)^2} \tag{3.4}$$

The distance between the location of the new beam waist after the lens and the receiver plane is denoted as z. With a certain lens and a determined free space transmission distance, the beam waist at the receiver plane can be adjusted by controlling the parameter L. Furthermore, background light is incorporated during the free space transmission.

At the receiver side, a coupling system is generally employed to collect and focus optical signal. With Gaussian distribution, the received optical power (P_r) is related to the beam waist after free space transmission and the distance from the beam centre at the receiver plane, which can be estimated as:

$$P_r = S_{Rx} \frac{2P_t}{\pi\omega^2} \exp\left(-\frac{2r^2}{\omega^2}\right) \tag{3.5}$$

where S_{Rx} is the equivalent receiver area, P_t is the output optical power at the transmitter side, ω is the beam waist at the receiver plane, and r is the distance from beam centre to the user's location. The approximation of the received optical power with Gaussian distribution is held when the receiver's aperture is smaller compared to the beam diameter and when the field-of-view of the receiver is larger than the incidence angle of the beam on the receiver.

After free space transmission, a photodiode (PD) is employed at the user terminal side to detect the optical signal and convert it to electrical signal for post-processing. After analog to digital conversion (A/D), the first step of post-processing is frequency down-conversion using the same carrier frequency employed in CO. The received signal after frequency down-conversion can be described as:

$$r_m = \sum_{j=-\infty}^{\infty} S \cdot v^j \cdot h\left(m - jT_s\right) + n_m \tag{3.6}$$

where S is the signal amplitude and n_m is the noise introduced from the transmitter, free space transmission and detection. A matched filter is used to down-sample the signal as well as to filter out the baseband signal. The received p^{th} symbol can be expressed as:

$$y\left[p\right] = S \cdot v^p + n' \tag{3.7}$$

where v^p represents the original p^{th} symbol and n' is the noise for one symbol. In the process of amplitude and phase recovery, a factor of $\sqrt{P_{tx}/P_{rx}}$ is multiplied with the received symbol sequence for amplitude compensation, where P_{tx} is the average power of the transmitted symbols and P_{rx} is the average power of the received symbol sequence. In addition, a conventional decision feedback equaliser is employed for phase recovery. After amplitude and phase recovery, baseband demodulation is carried and the corresponding bit error rate (BER) is evaluated.

3.3 Analytical Model with Square QAM

3.3.1 Symbol Error Rate

In the system of a typical indoor optical wireless communications, the noise applied to the received symbols after detection is assumed to follow a Gaussian distribution. The first quadrant of *I*-*Q* plane with 4-QAM modulation format is shown in Fig. 3.2 for illustrative purpose since all four *I*-*Q* quadrants are symmetrical.

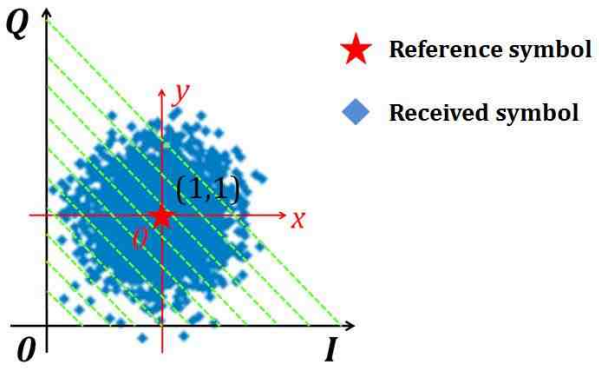

Fig. 3.2 Illustration of symbol error rate derivation example

The locations of received symbols are around the corresponding reference symbol and follow 2-dimension (2-D) Gaussian distribution $f(x, y)$, which treats the reference symbol as the origin of a new $x - y$ coordinate. The variables x and y are independent and have the same Gaussian distribution with zero mean and standard deviation σ:

$$\begin{aligned} f(x,y) &= f(x)\cdot f(y) \\ x,y &\sim N\left(0,\sigma^2\right) \end{aligned} \tag{3.8}$$

It should be noted that the Gaussian nature of the noise after detection is reasonably assumed when thermal noise is dominant in the system. The rate (R_1) that received symbols can be demodulated correctly as the reference symbol (1, 1) is calculated by integrating x and y over the decision region of symbol (1, 1), as shown in the green-dash-line region in Fig. 3.2:

$$R_1 = \int_{-1}^{\infty}\int_{-1}^{\infty} f(x,y)\,dxdy \tag{3.9}$$

Consequently, the symbol error rate (SER) for 4-QAM is calculated as:

$$SER_{4-QAM} = 1 - \int_{-1}^{\infty}\int_{-1}^{\infty} f(x,y)\,dxdy \tag{3.10}$$

The derivation of SER for higher-order QAM, e.g. 16-QAM, is presented in Appendix A in detail. After applying the same procedure to higher order square QAM modulation formats, the SER equation can be generalised for 2^{2l} – ary QAM as follows:

$$\begin{aligned} SER(l,\sigma) &= 1 - \frac{4}{2^{2l}} \cdot \left[\begin{array}{l} \left(4^{l-1} - 2^{l} + 1\right) \cdot \int_{-1}^{1}\int_{-1}^{1} f(x,y)\,dxdy \\ +2 \cdot \left(2^{l-1} - 1\right) \cdot \int_{-1}^{\infty}\int_{-1}^{1} f(x,y)\,dxdy + \int_{-1}^{\infty}\int_{-1}^{\infty} f(x,y)\,dxdy \end{array} \right] \\ &= 1 - \frac{4}{2^{2l}} \cdot \left[\begin{array}{l} \left(4^{l-1} - 2^{l} + 1\right) \cdot \left(F(1,\sigma) - F(-1,\sigma)\right)^2 \\ +2 \cdot \left(2^{l-1} - 1\right) \cdot \left(F(1,\sigma) \cdot \left(F(1,\sigma) - F(-1,\sigma)\right)\right) + \left(F(1,\sigma)\right)^2 \end{array} \right] \end{aligned}$$

$$F(\nu,\sigma) = \int_{-\infty}^{\nu} \frac{1}{\sigma\sqrt{2\pi}} \exp\left(-\frac{x^2}{2\sigma^2}\right) dx \tag{3.11}$$

3.3.2 Standard Deviation in indoor OWC system

In order to obtain the standard deviation σ expression for indoor OWC system, we first describe the root-mean-square (RMS) average of error vector magnitude (EVM_{RMS}) in terms of σ. The EVM_{RMS} is defined as [127]:

$$EVM_{RMS} = \sqrt{\frac{\frac{1}{N}\sum_{n=1}^{N}\left|I_n - I_{0,n}\right|^2 + \left|Q_n - Q_{0,n}\right|^2}{\frac{1}{J}\sum_{j=1}^{J}(I_{0,j})^2 + (Q_{0,j})^2}} \tag{3.12}$$

where I_n and Q_n are the normalised in-phase and quadrature voltage, respectively, for received symbols after amplitude compensation and N is the number of received symbols. The parameters $I_{0,n}$ and $Q_{0,n}$ denote the in-phase and quadrature component for corresponding ideal symbols in the constellation, respectively. In the denominator, $I_{0,j}$ and $Q_{0,j}$ constitute ideal constellation point and J is the number of symbol patterns

in the constellation. Considering the Gaussian noise model first, Eq. (3.12)can be further simplified as:simplified as:

$$EVM_{RMS} = \sqrt{\frac{\sigma_I^2 + \sigma_Q^2}{P_{avg}}} \tag{3.13}$$

where P_{avg} is the average power of the ideal constellation. The notations of σ_I and σ_Q represent the standard deviation of *f (x)* and *f (y)* shown in Eq. (3.8) Since the variables *x* and *y* are independent and have the same Gaussian distribution, we have: are independent and have the same Gaussian distribution, we have:

$$\sigma_I = \sigma_Q = \sigma \tag{3.14}$$

The average power of the ideal constellation $P_{avg}(l)$ for 2^{2l} – ary QAM is calculated as:

$$P_{avg}(l) = \frac{2}{3}\left(4^l - 1\right) \tag{3.15}$$

Based on Eq. (3.14)(3.15) (3.13)re-written as:can be thus re-written as:

$$EVM_{RMS}(l,\sigma) = \sqrt{\frac{3\sigma^2}{4^l - 1}} \tag{3.16}$$

In addition, EVM_{RMS} can be approximated in form of signal-to-noise ratio (SNR) as [127]:

$$EVM_{RMS} \approx \sqrt{\frac{1}{SNR}} \tag{3.17}$$

The standard deviation σ thus has an obvious relationship with SNR, which is described according to Eq. (3.16)(3.17) as:

$$\sigma = \sqrt{\frac{4^l - 1}{3 \cdot SNR}} \tag{3.18}$$

As a significant parameter for system performance indicator, SNR for 2^{2l} – ary QAM in indoor OWC system is defined as:

$$SNR = \frac{\left(R \cdot P_r\right)^2}{\beta \cdot N_{total}^2} \tag{3.19}$$

where R is the photodetector responsivity and P_r is the average received optical power at the receiver side. The modulation format-dependent factor, which is denoted as β, is included in our system since the output peak-to-peak voltage (V_{pp}) of the D/A equipment is fixed for all modulation formats with different orders. It can be calculated as the ratio of peak power (P_{peak}) and average power (P_{avg}) of the corresponding constellation:

$$\beta(l) = \frac{P_{peak}}{P_{avg}} = \frac{3 \cdot \left(2^l - 1\right)^2}{4^l - 1} \tag{3.20}$$

Furthermore, the total noise variance is represented by N^2_{total}. Previous studies have found that noise sources including background light induced shot noise and receiver preamplifier induced noise from transmission and detection dominate in typical indoor optical wireless communications system [8, 128]. Considering the non-ideal laser source, intensity noise is also included in our derived system model, in which relative intensity noise (*RIN*) describes the instability in the power level of a laser [129, 130]. Hence, the total noise variance N^2_{total} can be expressed as:

$$N^2_{total} = N^2_{bn} + N^2_{pre} + N^2_{rin} \tag{3.21}$$

where N^2_{bn}, N^2_{pre} and N^2_{rin} represent the background light induced noise variance, the preamplifier induced noise variance and RIN noise variance component, respectively. The background light induced noise can be calculated as:

$$N^2_{bn} = 2eRP_{bn}A_2B \tag{3.22}$$

where e is electron charge, A_2 is a weighting function of 0.562, and B is the electrical signal bandwidth. The received background light power is denoted by P_{bn}. In many practical office environments, tungsten lamps and fluorescent lamps are widely used. Those lamps can be modelled as a Lambertian source, where the optical power can be approximated to be evenly distributed with a relatively large mode number [131].

In addition to the background light induced noise, the preamplifier employed in our system is a positive intrinsic negative diode (p-i-n) receiver with an integrated field-effect-transistor (FET) based transimpedance preamplifier. The major noise sources in this type of preamplifier consist of Johnson noise associated with the FET channel conductance, Johnson noise from the load or feedback resistor, shot noise arising from

gate leakage current and *1/f* noise [132]. According to [133], the FET gate leakage and *1/f* noise can be ignored for simplicity. The preamplifier induced noise can therefore be approximated by:

$$N_{pre}^2 = \frac{4kT}{R_f} A_2 B + \frac{4kT\Gamma}{g_m} \left(2\pi C_T\right)^2 A_3 B^3 \tag{3.23}$$

where k is the Boltzmann's constant, T is the absolute temperature, R_f is the feedback resistance, Γ is a noise factor associated with channel thermal noise and gate induced noise in the FET and has a range from 1.1 to 1.8 [132], g_m is the transconductance of FET, C_T is the total capacitance consisting of photodetector and stray capacitance, and A_3 is another weighting function with the value of 0.0868 [132]. Both weighting functions A_2 and A_3 are dependent on the input optical pulse shape to the receiver and the equalised output pulse shape. Furthermore, RIN noise variance is calculated as:

$$N_{rin}^2 = B\left(RP_r\right)^2 RIN \tag{3.24}$$

Based on Eq. (3.16)– (3.24)dependent standard deviation can be determined by system parameters of indoor OWC system as:of indoor OWC system as:

$$\begin{aligned} \sigma(l) &= \frac{2^l - 1}{RP_r} \sqrt{N_{bn}^2 + N_{pre}^2 + N_{rin}^2} \\ &= \frac{2^l - 1}{RP_r} \sqrt{2eRP_{bn} A_2 B + \frac{4kT}{R_f} A_2 B + \frac{4kT\Gamma}{g_m} \left(2\pi C_T\right)^2 A_3 B^3 + B\left(RP_r\right)^2 RIN} \end{aligned} \tag{3.25}$$

3.3.3 Relationship between SER and BER

As we have now derived the expression of SER, the next step is to link the SER with BER. In 2^{2l} – ary QAM modulation with gray coding, the relationship between BER and SER (α=SER/BER) is dependent on E_b / N_0 , which is the energy per bit to noise power spectral density ratio. According to [134, 135], the ratio of SER and BER for a general square QAM can be calculated as:

$$\alpha\left(l,\frac{E_b}{N_0}\right)=\frac{\left(\begin{array}{l}2\left(2^l-1\right)\cdot l\cdot Q\left(\sqrt{\frac{3}{2^{2l}-1}\frac{2lE_b}{N_0}}\right)-\\2\left(2^l-2+2^{-l}\right)\cdot l\cdot Q^2\left(\sqrt{\frac{3}{2^{2l}-1}\frac{2lE_b}{N_0}}\right)\end{array}\right)}{\left(\sum_{(2l)=1}^{l}\sum_{i=0}^{\left(1-2^{-2l}\right)2^l-1}\left\{\begin{array}{l}(-1)^{\left\lfloor i2^{l-1}\right\rfloor}\cdot\left(2^{2l-1}-\left\lfloor i2^{l-1}+\frac{1}{2}\right\rfloor\right)\cdot\\Q\left(\left(2i+1\right)\sqrt{\frac{6l}{2^{2l}-1}\frac{E_b}{N_0}}\right)\end{array}\right\}\right)} \tag{3.26}$$

where $Q(.)$ is the Gaussian co-error function. Fig. 3.3 shows several examples of α in terms of E_b/N_0 for square 2^{2l} – ary QAM, where l is 1, 2 and 3 for 4-QAM, 16-QAM and 64-QAM, respectively.

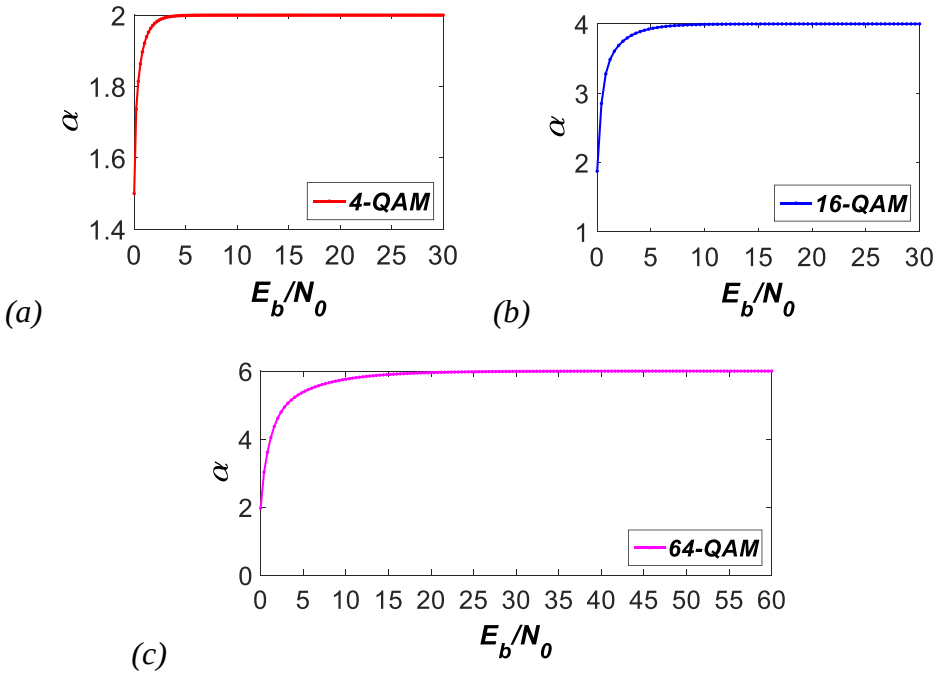

Fig. 3.3 Ratio of SER and BER (α) respect to E_b/N_0 for (a) 4-QAM, (b) 16-QAM and 64-QAM

It can be seen that the common approximation used in [124], where $BER=SER/(2l)$ is only valid for relatively high SNR. The next step to link SER with BER is to find E_b/N_0 in the form of modulation format parameter (l) and standard deviation (σ). The signal-to-noise ratio (SNR) is defined as:

$$SNR = \frac{E_s}{N_0} \tag{3.27}$$

where E_s is the energy per symbol and has a relationship with the energy per bit (E_b) as:

$$E_s = 2l \cdot E_b \tag{3.28}$$

Therefore, E_b / N_0 for a general square QAM modulation format can be derived in terms of σ according to Eq. (3.16)(3.17) (3.27): (3.28):

$$\frac{E_b}{N_0}(l,\sigma) = \frac{4^l - 1}{6 \cdot l \cdot \sigma^2} \tag{3.29}$$

The BER for typical indoor optical wireless communications system with a general square QAM modulation format is consequently shown as:

$$BER(l,\sigma) = \frac{1}{\alpha} - \frac{4}{\alpha \cdot 2^{2l}} \cdot \left[\begin{array}{l} \left(4^{l-1} - 2^l + 1\right) \cdot \left(F(1,\sigma) - F(-1,\sigma)\right)^2 \\ +2 \cdot \left(2^{l-1} - 1\right) \cdot \left(F(1,\sigma) \cdot \left(F(1,\sigma) - F(-1,\sigma)\right)\right) \\ +\left(F(1,\sigma)\right)^2 \end{array} \right] \tag{3.30}$$

$$F(\omega,\sigma) = \int_{-\infty}^{\omega} \left[1 \Big/ \left(\sigma\sqrt{2\pi}\right) \right] \exp\left(-x^2 / 2\sigma^2\right) dx$$

3.4 Experimental Demonstration

3.4.1 Experimental Setup

As analysed and derived in Section 3.3, the modulation format dependent BER is expressed in terms of standard deviation of the received signal distribution and the standard deviation can be calculated according to Eq. (3.25)experiment and compare experimental measurements of σ and BER with those calculated using the analytical model. and BER with those calculated using the analytical model.

Experimental verification was carried out using the setup shown in Fig. 3.4. In the experiments, different orders of square QAM modulated data were separately generated off-line in MATLAB and sent to an arbitrary wave generator (AWG). After passing through an electrical amplifier (EA), the amplified electrical signal modulated a tunable laser centred at 1553.01 nm (RIN ~ -118 dB/Hz) via a Mach-Zehnder modulator (MZM). The optical polarisation state was modified by a fibre polarisation controller (PC). At the output of the MZM, the modulated optical signal was launched into a 5.6 km single-mode fibre to emulate the distribution process from the central office to the indoor transmitter. A single channel free space transmission link was established in our experiments. At the transmitter side, a lens with focal length of 4.5 mm was placed after the fibre end to collimate the output optical beam. The optical power after the transmitter fibre end was set to 7.5 dBm to comply with eye and skin safety regulations [136]. After 2 m of free space transmission, another lens (focal length: 4.5 mm) was employed to collect and focus the optical signal into the fibre end. Background light power was measured by a free space optical power meter as -30.12 dBm when the signal was not transmitted. An optical attenuator (OA) for 1550 nm band was employed to adjust the received optical power level. Then a 10 GHz photodiode (PD) integrated with a FET based transimpedance preamplifier and with ~0.8 A/W responsivity at 1550 nm band was used to convert the optical signal to the electrical signal. A digital storage oscilloscope (DSO) performed analog to digital conversion (A/D) for off-line processing.

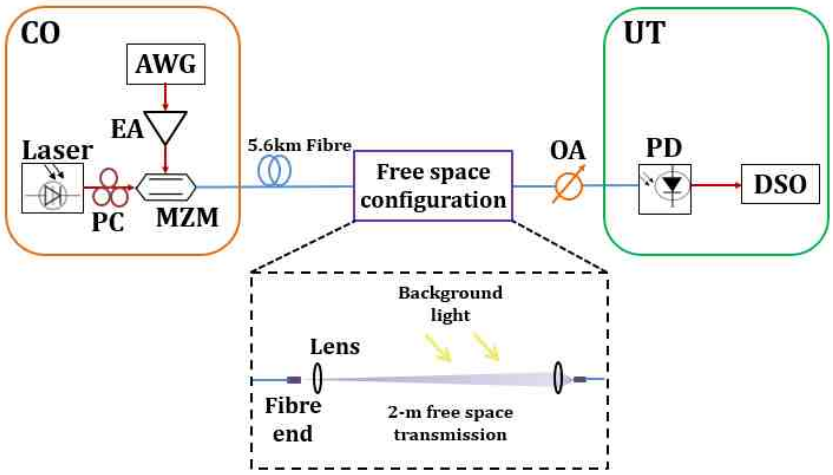

Fig. 3.4 Experimental setup for indoor optical wireless communications system with a single channel

3.4.2 Results and Discussions

Without loss of generality, both 4-QAM (l = 1) and 16-QAM (l = 2) modulation formats were experimentally evaluated, each with multiple data rates and thus with multiple signal bandwidths (B). For a signal modulated based on a 2^{2l} – ary QAM modulation format, the symbol rate (R_s) is $2l$ times of the bit rate (R_b), i.e. $R_s = 2l \times R_b$. The 3 dB passband signal bandwidth at the electrical side (B) considered in the system model has a relationship with R_s whereby: $B = 2 \times 0.75 \times R_s$. In our experiments, the symbol rates of 2.5 Gbaud/s, 2 Gbaud/s, 1.67 Gbaud/s, 1.25 Gbaud/s, 1 Gbaud/s, 0.833 Gbaud/s and 0.625 Gbaud/s were employed for both 4-QAM and 16-QAM modulation formats while the highest symbol rate was restricted by the sampling frequency of AWG. Apart from the parameters as discussed throughout the text above (e.g., A_2, A_3, B, P_{bn}, RIN, R, etc.), other key parameters are given as below:

k (W/(K×Hz)	$10^{(-228.5991678/10)}$	R_f (Ω)	50
T (K)	300	C_T (pF)	4
e	1.60217662e-19	g_m (mS)	15
Γ	1.8		

Furthermore, due to nonlinear distortion effect, the standard deviations of in-phase and quadrature components (σ_I and σ_Q) are not identical in practice. Measured standard deviation (σ) was taken as an average of measured σ_I and σ_Q in the experiments. Fig. 3.5 shows both experimental and analytical results of standard deviation based on 4-QAM modulation format with multiple data rates.

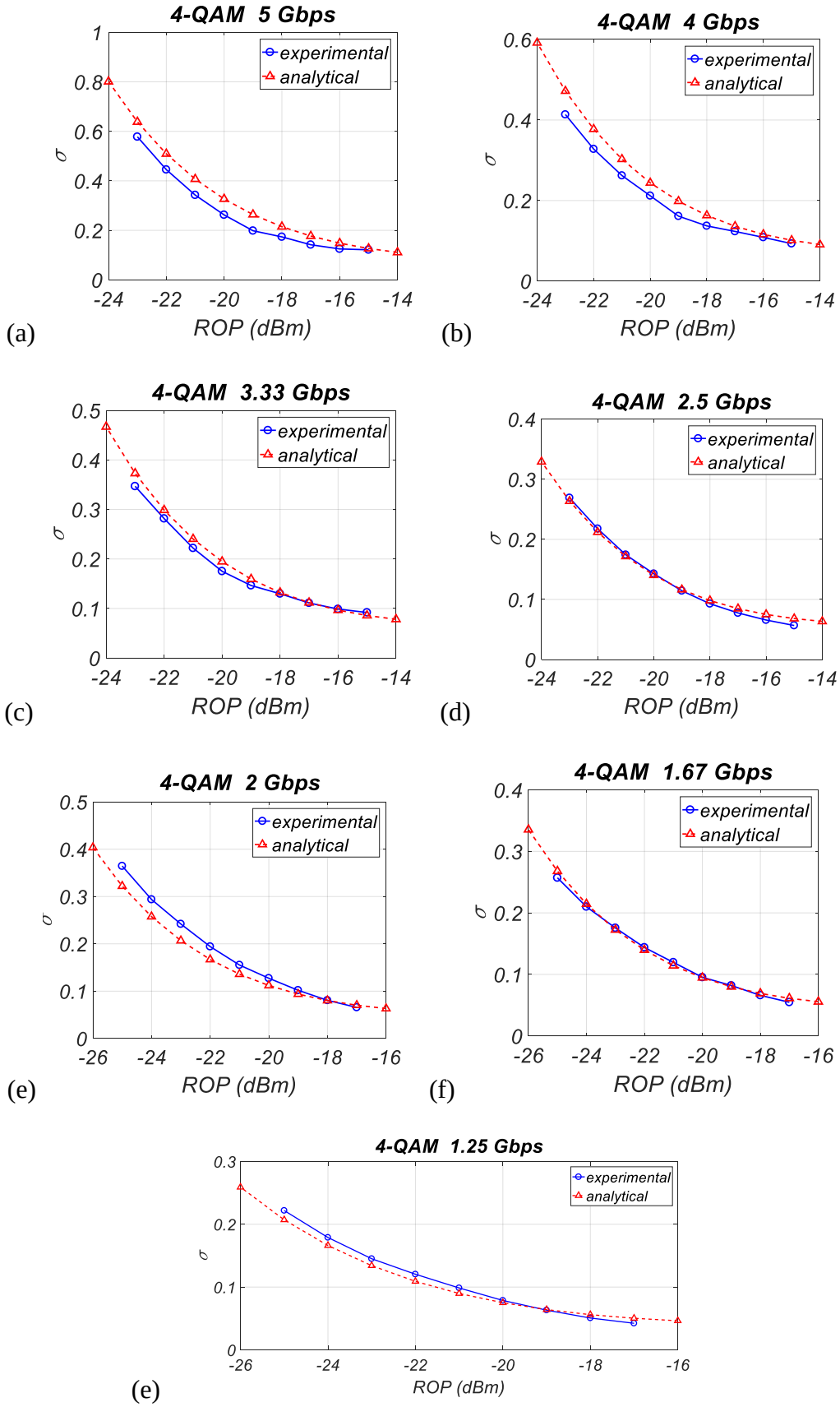

Fig. 3.5 Comparison between measured and analytical standard deviations based on 4-QAM modulation format with (a) 5 Gb/s, (b) 4 Gb/s, (c) 3.33 Gb/s, (d) 2.5 Gb/s, (e) 2 Gb/s, (f) 1.67 Gb/s, and (g) 1.25 Gb/s

Results in Fig. 3.5 show that the experimentally measured standard deviation approximately matches with the analytical result calculated using Eq. (3.25) The offsets between experimental results and those simulated using analytical model might be attributed to nonlinear distortion arising in the experiments and the approximation employed during analytical model derivation process. Furthermore, it can be seen that a signal with higher data rate provides a larger σ when the average received optical power (ROP) is identical. That is because the major noise sources including background light noise, preamplifier induced noise and intensity noise increase with the signal bandwidth. It is also observed that the standard deviation reaches a floor as the received optical power level is increased further. This is due to RIN noise that is proportional to the optical power. Thus, the signal-to-noise ratio cannot be infinite with increasing optical power. .

(a)

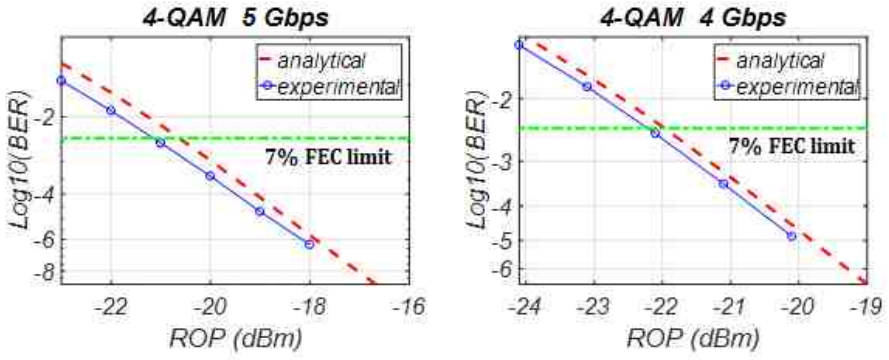

(b)

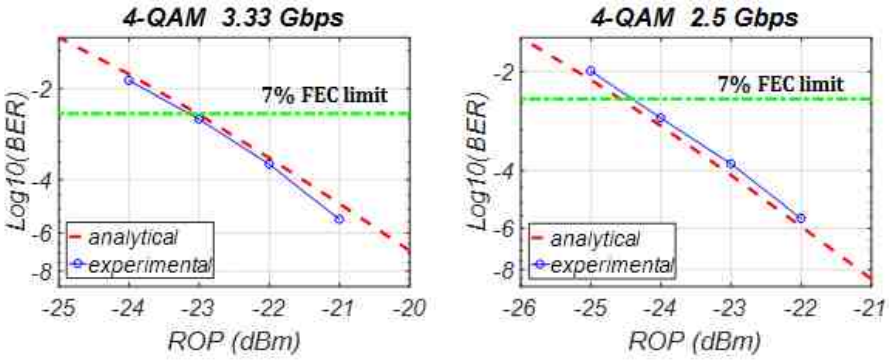

(c)

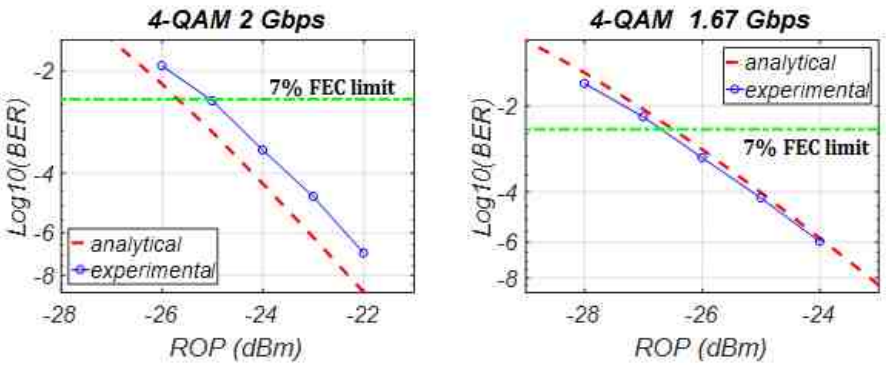

(d)

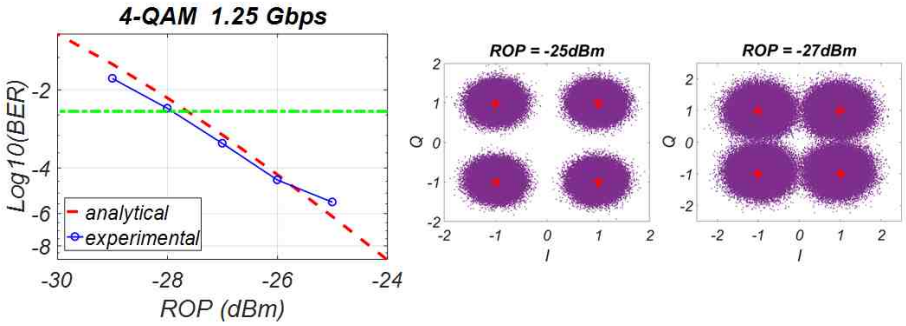

Fig. 3.6 Comparison between measured and analytical BER based on 4-QAM modulation format with (a) 5 Gb/s and 4 Gb/s, (b) 3.33 Gb/s and 2.5 Gb/s, (c) 2 Gb/s and 1.67 Gb/s, and (d) 1.25 Gb/s with experimental signal constellations for -25 dBm and -27 dBm

The BER performance measured in the experiments and calculated using the combination of Eq. (3.25)(3.26), (3.29)further (3.30)Fig. 3.Fig. 3.6% forward error correction (FEC) limit [137]. Since the number of transmitted symbols is limited by the memory of the AWG used in our experiments, the minimum BER that we were able to measure was around 1×10^{-7}. It can be seen that the largest offset between the measured and calculated results is about 0.5 dBm, which is satisfactory to claim that the analytical model is successfully demonstrated for 4-QAM modulation format. In Fig. 3.Fig. 3.6 also included for illustration. It is intuitive that the received signal with smaller standard deviation has lower BER due to more concentrated signal distribution. The receiver sensitivity, which is defined as the minimum average received optical power required by the photodetector to achieve error-free detection (BER $\leq 3.8 \times 10^{-3}$), for higher speed system is worse than that for lower bit rate. For a specific bit rate, BER increases with decreasing received optical power, although a lower level of received optical power provides less RIN noise. This occurs because the degradation in SNR due to decreasing ROP is more dominant. Detailed investigations of key system parameters, such as *RIN*,

background light power, etc., will be further explored in Chapter 6.further explored in Chapter 6.

In addition to the 4-QAM modulation format, we also evaluated the indoor OWC system based on the 16-QAM modulation format (l = 2) both analytically and experimentally. The calculated and measured standard deviations are shown in Fig. 3.7

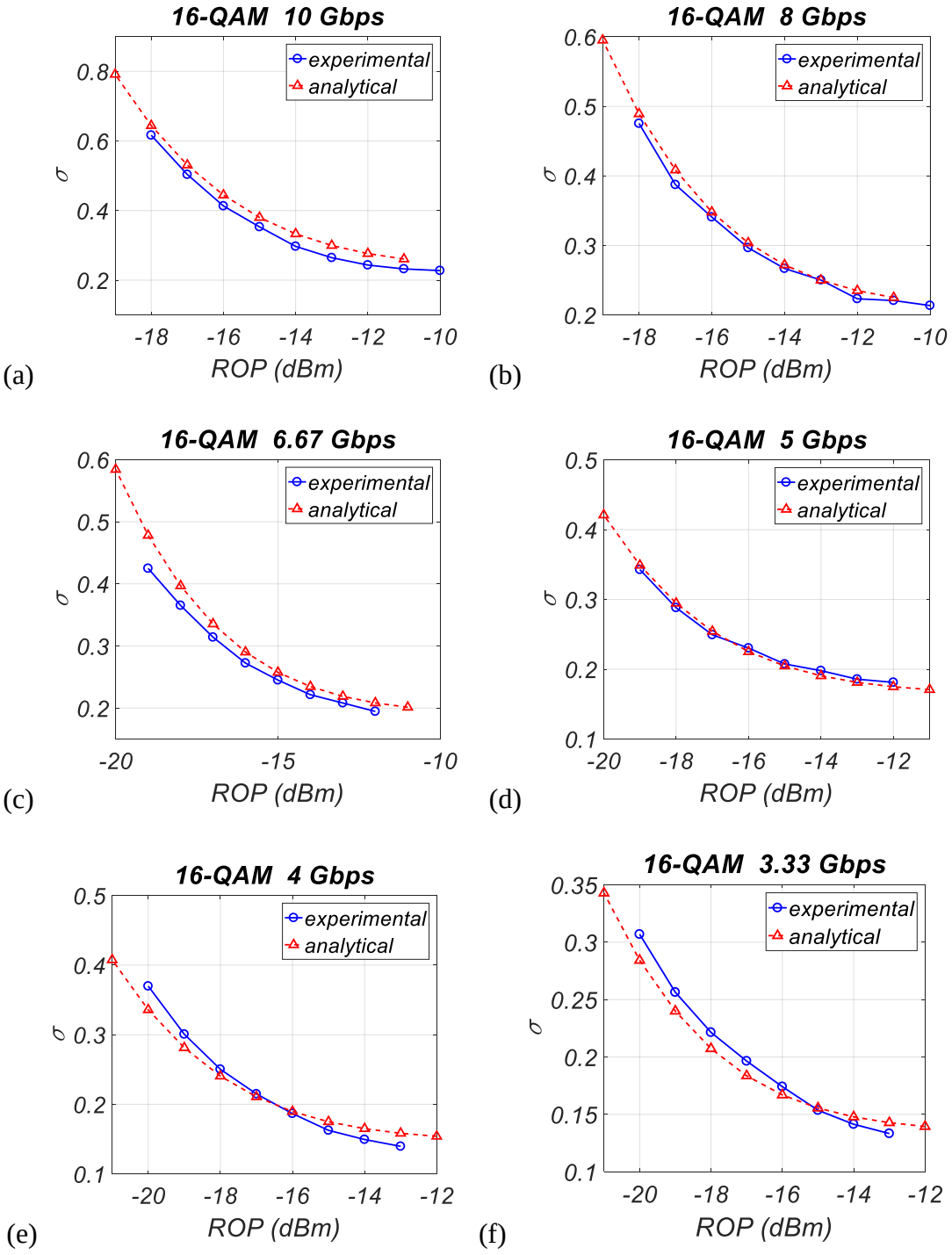

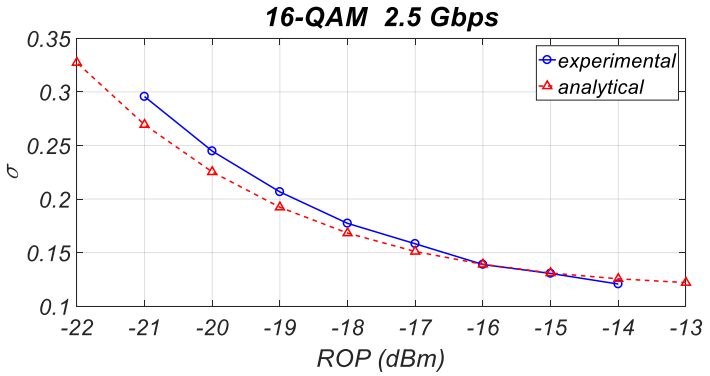

(g)

Fig. 3.7 Comparison between measured and analytical standard deviations based on 16-QAM modulation format with (a) 10 Gb/s, (b) 8 Gb/s, (c) 6.67 Gb/s, (d) 5 Gb/s, (e) 4 Gb/s, (f) 3.33 Gb/s, and (g) 2.5 Gb/s

The parameter l is responsible for controlling the order of QAM modulation format in the analytical system model. For 4-QAM and 16-QAM modulated data with the same symbol rate (R_s), i.e. the same electrical signal bandwidth (B), the amount of major noise sources are the same. However, comparing the results shown in Fig. 3.5 and Fig. 3.7, it can be seen that the 16-QAM modulation format produces a larger standard deviation than that of the 4-QAM modulation format since the 16-QAM modulated data has less average signal power with a fixed output V_{pp} of the AWG. The receiver sensitivity results for the 16-QAM modulated data with different data rates are further investigated and illustrated in Fig. 3.8.

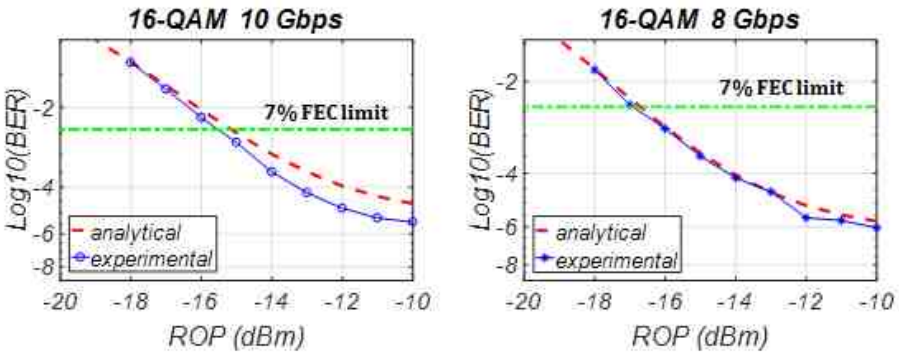

(a)

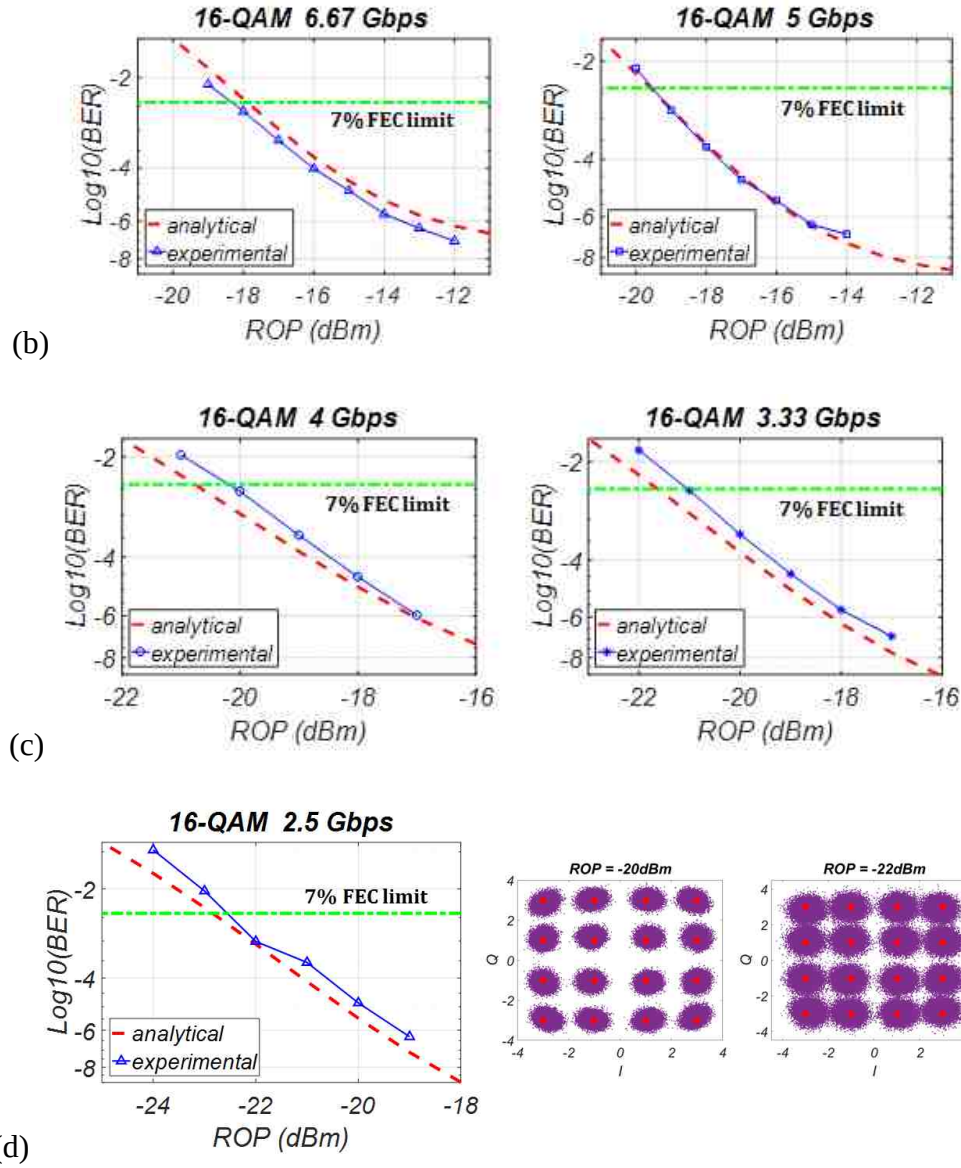

Fig. 3.8 Comparison between measured and analytical BER based on 16-QAM modulation format with (a) 10 Gb/s and 8 Gb/s, (b) 6.67 Gb/s and 5 Gb/s, (c) 4 Gb/s and 3.33 Gb/s, and (d) 2.5 Gb/s with experimental signal constellations for -20 dBm and -22 dBm

It can be seen that the analytical results also agree well with the experimentally measured BER results for the 16-QAM modulation format, where the maximum receiver sensitivity difference for data rates ranging from 2.5 Gb/s to 10 Gb/s is around 0.5 dBm. What is more, the 4-QAM modulated signal has better receiver sensitivity than the 16-QAM modulated signal in our system due to a less stringent requirement of SNR. For example, for a data rate of 5 Gb/s, 4-QAM has a receiver sensitivity of around -21 dBm while the receiver sensitivity for 16-QAM is -19.5 dBm.

3.5 Conclusions

In this chapter, we have derived the SER equation based on the signal constellation with the intended received symbol and the noise around the corresponding symbol, which was represented by the standard deviation of the distribution of the noisy received symbols. Three major noise sources encountered from the unstable laser source, the free space transmission channel and the preamplifier integrated photodetector have been considered and modelled for indoor OWC system with general QAM modulation format. The system BER was further linked with the SER by establishing a relationship between them. Both standard deviation and BER were measured in the demonstration experiments for 4-QAM and 16-QAM modulated system with multiple data rates, i.e. 1.25 Gb/s, 1.67 Gb/s, 2 Gb/s, 2.5 Gb/s, 3.33 Gb/s, 4 Gb/s and 5 Gb/s for 4-QAM and 2.5 Gb/s, 3.33 Gb/s, 4 Gb/s, 5 Gb/s, 6.67 Gb/s, 8 Gb/s and 10 Gb/s for 16-QAM, to evaluate the generality of the derived system analytical model. The comparison between measured results and analytical results obtained via the analytical model showed good agreement in BER, where the maximum receiver sensitivity offset between them is within 0.5 dBm. The verified system model in this chapter provides fundamental grounds for more theoretical analyses to be discussed in the subsequent chapters.

Chapter 4 Time-slot Coding Scheme for Multiple Access for Indoor Optical Wireless Communications

4.1 Introduction

In-building high-speed OWC has been widely studied and demonstrated with single user access exceeding 200 Gb/s using SDM or WDM techniques [6, 7]. Despite the ability of supporting high data rates per single user, it is critical and vital for indoor OWC to also support multiple users to ensure practical and realistic deployment. In previous studies, multiple access in OWC systems has been demonstrated using specific multiplexing techniques such as FDMA, CDMA, TDMA, or the combination of these techniques. As discussed in the previous sections, however, the adoption of traditional multiplexing techniques has limitations, including the requirements of high bandwidth requirements of optoelectronic devices such as modulators and photodiodes in FDMA systems, the need for long-length code and complex processing techniques in CDMA systems, and strict timing requirements in TDMA systems [69, 71, 74], respectively.

In order to overcome limitations of the aforementioned conventional multiplexing techniques, in this chapter we propose the time-slot coding (TSC) scheme to support multiple users simultaneously. Since time synchronisation issues are prevalent in the conventional TDMA implementation [138] and often requiring additional guard intervals or a scheduling framework to manage the issue of time synchronisation [139 – 141], we propose a technique that simplifies this issue by using "pre-assignment code" (referred to as time-slot code). Our scheme does not require scheduling framework or guard intervals to allow transmission of symbols over different slots. In TSC, each user has a dedicated code to acquire its symbol sequence instead of using a timing window

as in the conventional TDMA implementations. We have experimentally shown the proposed scheme for an aggregate bit rate of 2.5 Gb/s serving 5 users simultaneously based on the transmission of 4-QAM modulation format. We further improved the spectral efficiency (SE) and increased the aggregate bit rate to 4 Gb/s by using higher order modulation format (16-QAM).

In OWC systems, the service coverage area is typically within several meters, resulting in small variance in transmission distances to different terminals. However, the transmission optical power is not only restricted by eye and skin safety regulations but also degrades rapidly from the beam centre to the boundary. Therefore, realising a larger coverage from a single transmitter is always challenging. Adaptive loading technique is thus necessary in OWC systems to accommodate for various signal-to-noise ratio (SNR) conditions by tailoring the transmitted signal accordingly to ensure all users performance are maintained. In this chapter, we also investigate the capability of TSC scheme to support adaptive loading function by employing both 4-QAM and 16-QAM simultaneously to serve multiple users at different locations. Besides providing multiple data rates, satisfactory coverage can be extended by a maximum of 61.2% compared to employing 16-QAM only. Furthermore, compared to the system only employing 4-QAM, satisfactory coverage is similar while the system capacity can be increased by 20% to 80% for 5-user case, depending on the number of users employing 16-QAM.

In addition, since the adoption of time-slot code eliminates inter-user interference, the code misalignment will have a significant impact on the user's performance. Thus, the analysis of code overlapping ratio for a general square QAM modulation format needs to be investigated. Both analytical results and experimental results show that the code misalignment tolerance can be more than 92.3% for 4-QAM and 26.9% for 16-QAM with received optical power levels greater than -19.7 dBm.

The rest of this chapter is organised as follows:

In section 4.2, the principle and system architecture of the proposed TSC scheme are described. Section 4.3 presents the experimental results of multiple access employing the TSC scheme, including the BER result of each user and the average BER of all users transmission based on 4-QAM and 16-QAM modulation formats. The impact of the number of users in the system is also experimentally investigated. In Section 4.4, the

principle of the TSC scheme with adaptive loading function is proposed and experiments are carried out for two strategies of adaptive loading implementation. Finally, the code misalignment tolerance of the TSC scheme for a general square QAM modulation format is theoretically analysed in Section 4.5. Theoretical comparison of the tolerance to imperfect timing issue is presented between the proposed TSC and the conventional TDMA. The code misalignment tolerance is also experimentally evaluated for 4-QAM and 16-QAM, respectively.

4.2 Principle and System Architecture of Time-slot Coding

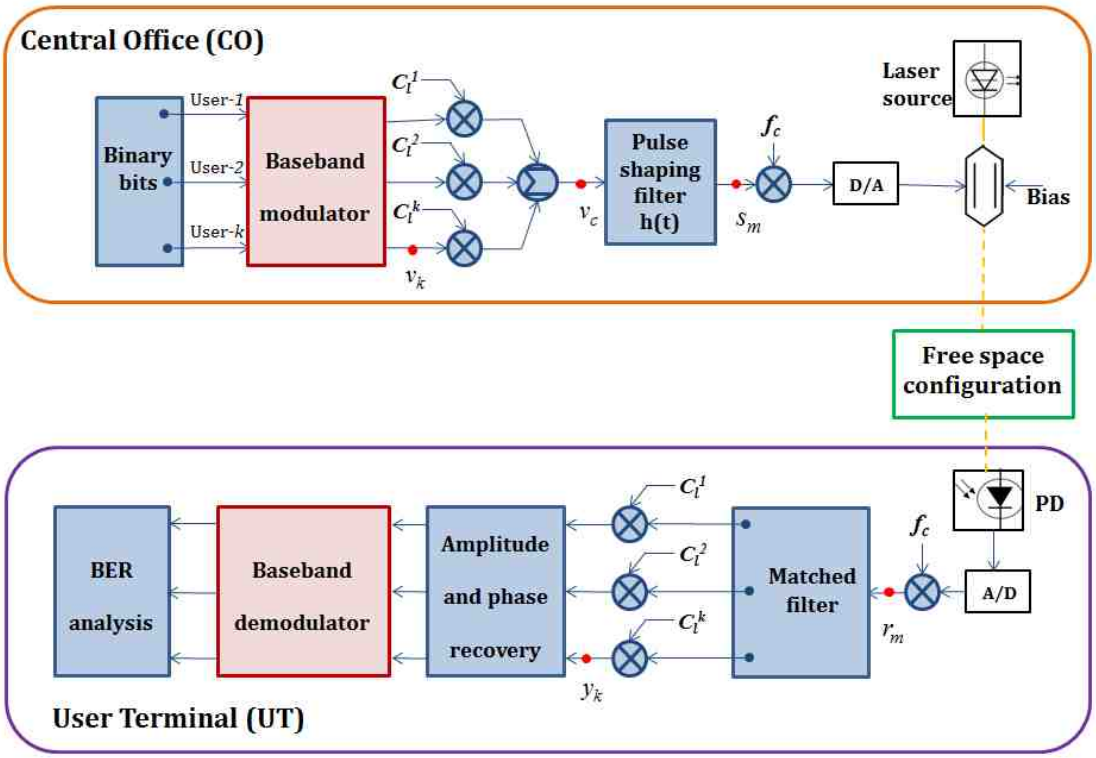

Fig. 4.1 Block diagram of time-slot coding scheme for optical wireless communications system

The system block diagram of time-slot coding (TSC) scheme is explained in Fig. 4.1. As illustrated, the downlink binary data is firstly generated for *k* users in the central office before baseband modulation. After symbol pattern mapping, Fig. 4.2 shows the multiuser scenario that considers *k* active users, each with *N* symbols to transmit. The original symbol period of each user is T_s and all users are fairly treated. To apply the proposed time-slot coding scheme, we generate a set of simple *k*-bit codes with only two unipolar values (0 and 1). Each code has a unique location for the value of 1 as described in Eq. (4.1)where each row of the *k*-by-*k* identity matrix represents the time-slot code for an individual user. identity matrix represents the time-slot code for an individual user.

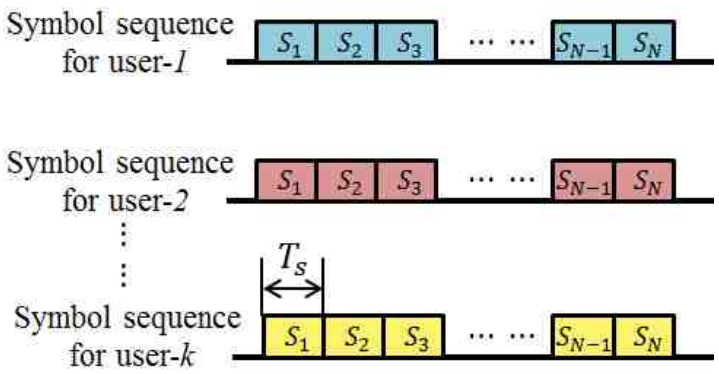

Fig. 4.2 Original symbol data for *k* users

$$C_k = \begin{bmatrix} 1 & 0 & 0 & \cdots & 0 & 0 \\ 0 & 1 & 0 & \cdots & 0 & 0 \\ \vdots & & & & & \\ 0 & 0 & 0 & \cdots & 1 & 0 \\ 0 & 0 & 0 & \cdots & 0 & 1 \end{bmatrix} \tag{4.1}$$

The i^{th} user can be assigned by the i^{th} row where the i^{th} code bit is the location for the value of 1. After multiplying each user's symbol sequence v_k with the dedicated code, the resultant coded symbol data sequences of each user are illustrated in Fig. 4.3. The coded data sequences from all the users are then added together to form the transmission data. With these codes, each user is ideally capable of occupying one non-overlapping

time slot to avoid multi-user interference (MUI), when all the users are served at the same time. The summed symbol sequence v_c travels through a raised-cosine pulse shaping filter and output sequence is denoted as s_m and can be expressed as:

$$s_m = \sum_{j=-\infty}^{\infty} v_c^j h\left(m - jT_s\right) \tag{4.2}$$

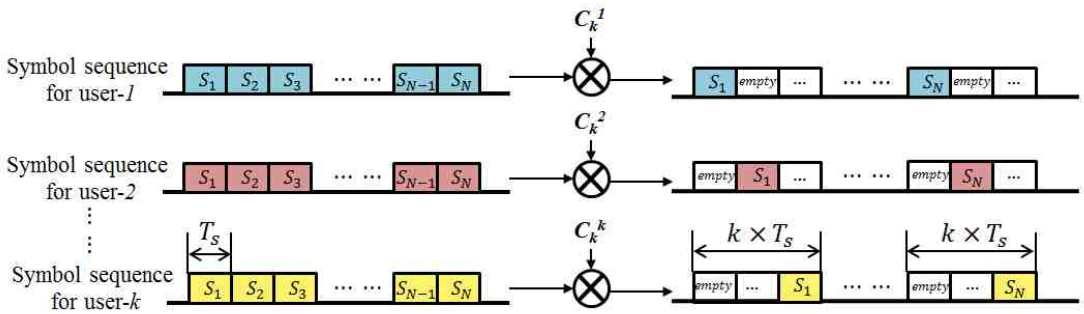

Fig. 4.3 Original symbol data for *k* users and coded symbol sequence of each user

Due to the lack of IQ mixer and IQ modulator, the baseband QAM signal is up-converted to a carrier frequency f_c (1 GHz) in MATLAB for demonstration purposes. After digital-to-analog conversion, the transmitted signal modulates the laser source via an external modulator. The PD is employed at the user terminal to detect the optical signal after free space transmission. The detected signal will be down-converted to baseband and processed using a matched filter. The user-specific time-slot code is then applied to each user to obtain its original symbol sequence. The performance of the scheme is quantified via BER analysis after the amplitude and phase recovery process.

4.3 Experimental Multi-user Demonstration

4.3.1 Experimental Setup

To demonstrate multi-user access using the proposed time-slot coding scheme, the experimental setup shown in Fig. 4.4 was employed to emulate the different locations of active users in real indoor scenarios. Instead of ceiling-mounted free space transmitter and ground-located receiver in real applications, we employed all optical components that were horizontally mounted on the bench top in this experimental demonstration. Here we demonstrate multiple access for 5 users.

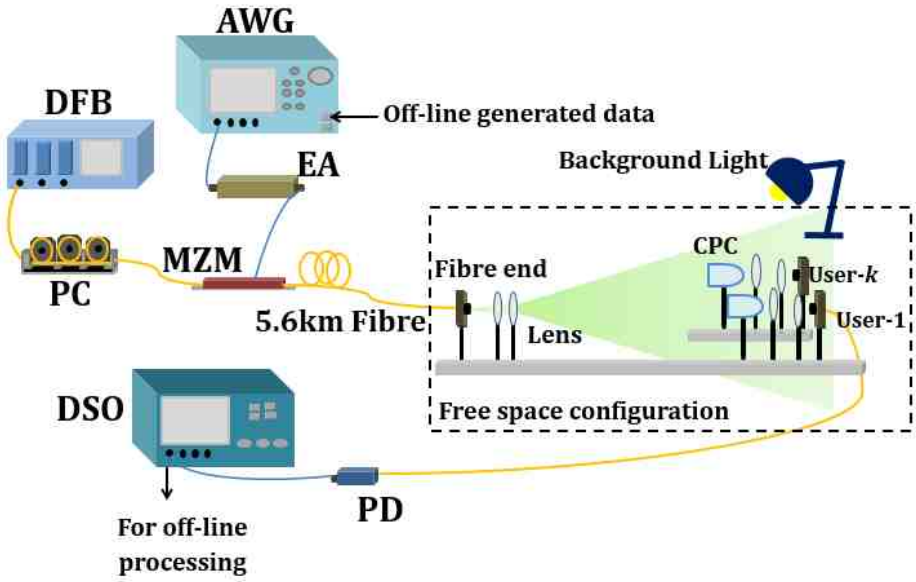

Fig. 4.4 Experimental setup with beam-expanding link for multi-user connections

The 4-QAM modulated TSC signal for 5 users was first generated in MATLAB and then loaded into the AWG for proof-of-concept demonstration. The output of the AWG was amplified by an EA and used to externally modulate a distributed feedback (DFB) laser with a wavelength of 1548 nm. The external modulator in the experiment was a MZM with 10 GHz modulation bandwidth. A PC was employed to control the polarisation state at the input of the MZM. After 5.6 km of single-mode fibre (SMF) distribution, the output optical beam from the fibre end was diffused by an adaptive lens system at the transmitter end so that multiple users can be served within a certain area. Due to the inavailability of shorter fibre in the laboratory, the 5.6 km of SMF was used to emulate the distribution fibre network within the building. In the adaptive lens system, three lenses were used with the focal lengths of 4.5 mm, 13 mm and 15 mm,

respectively. As discussed in Section 3.2, the beam waist at the receiver plane can be adjusted by controlling the distance between each lens. At the receiver, a coupling system consisting of a compound parabolic concentrator (CPC) with 45°field-of-view (FOV) and a number of lenses was used to collect and focus the optical signal into the fibre end of the photodetector. The receiver area diameter in our experiments was about 4 cm. Due to the device limitation, a pigtailed PD was used as the receiver rather than a free-space PD. The fibre-pigtailed PD has a 2 GHz 3 dB bandwidth and an integrated FET based transimpedance preamplifier. We also incorporated strong background light of -25.12 dBm at the receiver end. The DSO was used to capture the received electrical signal for off-line processing.

The transmitted optical power (the power output of the fibre end at the transmitter side) was 3.5 dBm, which was lower than the restriction set by eye and skin safety regulations [136], and no optical power amplifier was used in the experiment. Since the 1550 nm band has a typical free-space propagation loss ranging from 0.2 dB/km to 3 dB/km in a clear weather condition [142], there was negligible loss over several meters in typical indoor environments. As shown in [143], the receiver sensitivity did not vary with the free-space transmission propagation distance. With the low propagation loss in indoor environment, the free space transmission distance in our demonstration was fixed to 1.25 m. We have investigated different optical beam sizes (20 cm and 30 cm) for the transmission of 4-QAM signal over free-space. Our free space transmission distance and beamwidth expansion is limited by the availability of lenses in our laboratory.

4.3.2 Results and Discussions

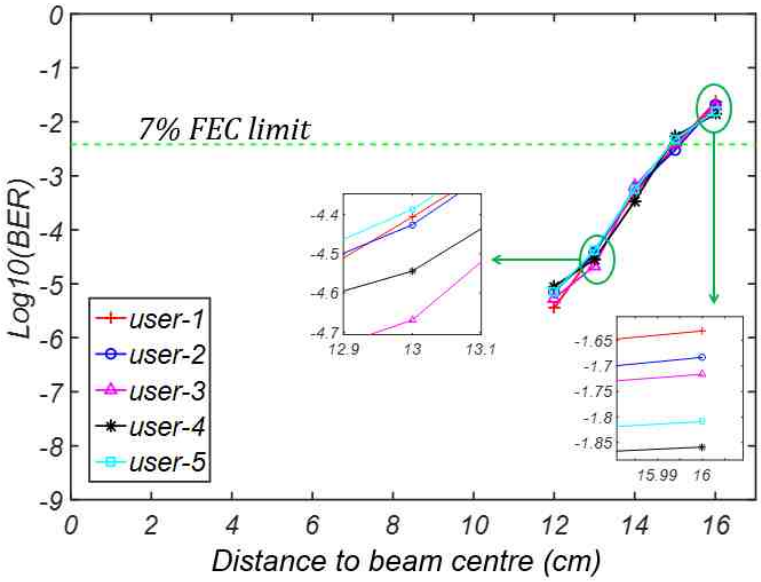

Fig. 4.5 BER performance of each user with beam waist of 20 cm

Fig. 4.5 shows the BER performance of all the 5 users at different locations when the aggregated bit rate was 2.5 Gb/s and the beam width was 20 cm. As shown, there is negligible penalty among the users with all users exhibiting similar performance. The results can be attributed to the fact that all users are treated fairly, as specified in the proposed TSC scheme.

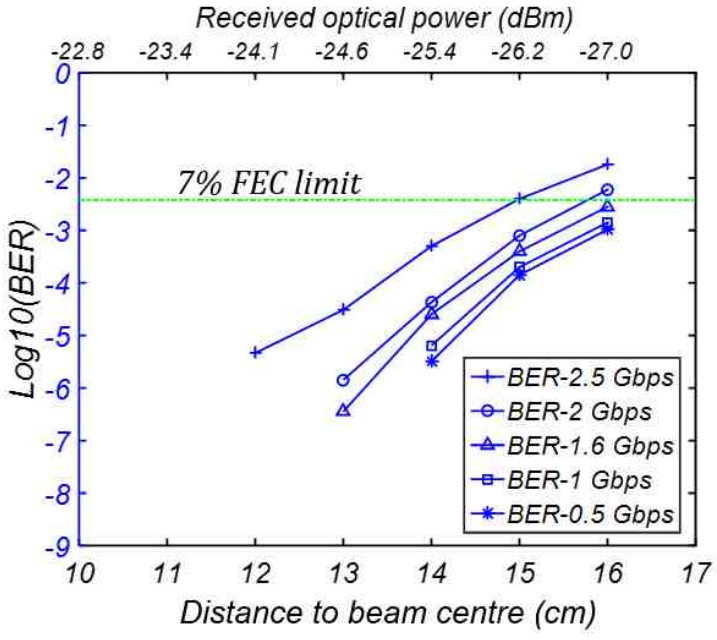

(a)

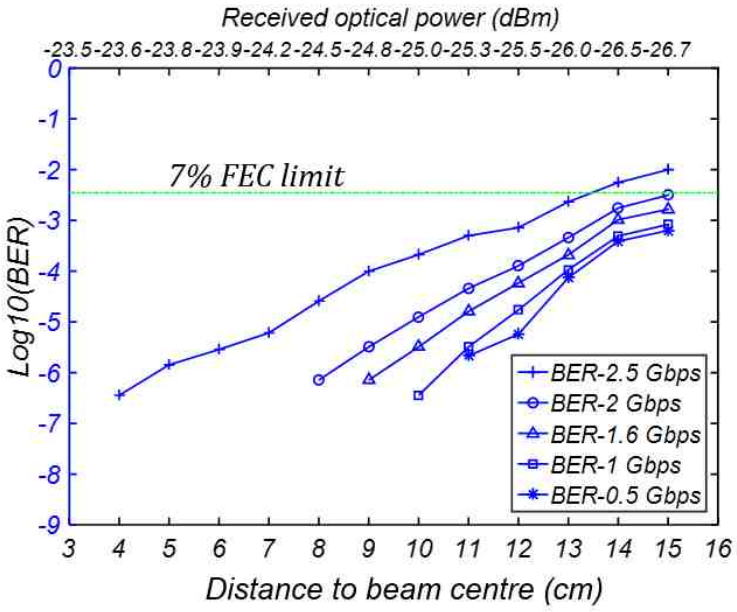

(b)

Fig. 4.6 Average BER for five users with different bit rates and the beam waist of (a) 20 cm and (b) 30 cm

We further investigated the impact of different aggregate data rates (2.5 Gb/s, 2 Gb/s, 1.6 Gb/s, 1 Gb/s and 0.5 Gb/s) on the overall performance. Fig. 4.6 shows the average BER for all five users and the received optical power with respect to the distance from the beam centre for beam widths of 20 cm and 30 cm. It can be seen that the error-free distance to the beam centre for 30 cm beam waist is smaller than that of 20 cm. For a specific bit rate, it is obvious that the BER increases when the user moves away from the beam centre. This happens because of the reduction in signal-to-noise ratio where the noise level does not differ much while the received optical power decreases with the distance from the beam centre. Similarly, with the same received optical power, the link with a lower bit rate has better BER performance. This is due to the noise originated from the instability in the laser transmitted power, background light and preamplifier in the optical receiver. These noise levels are increased with signal electrical bandwidth. Consequently, there is a trade-off between satisfactory coverage (which is defined as the area where users are able to achieve a BER of less than 3.8×10^{-3}, i.e. 7% FEC limit) and the achievable data rate.

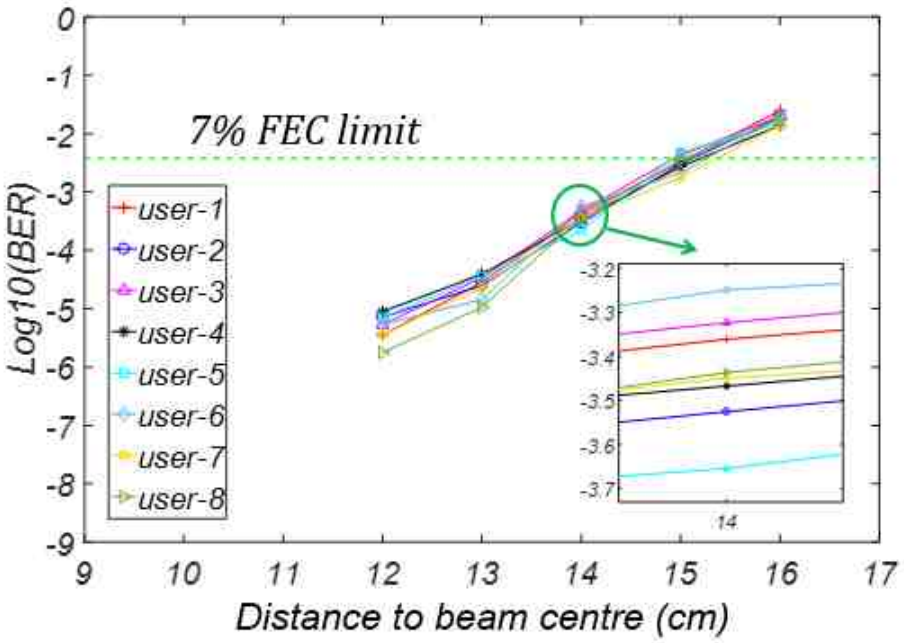

Fig. 4.7 BER of each user in 8-user and 2.5 Gb/s system

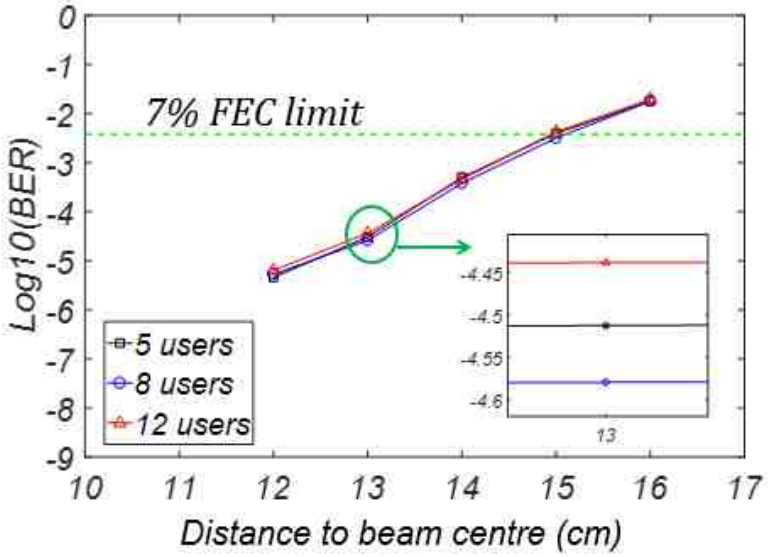

Fig. 4.8 Average BER with 4-QAM 2.5 Gb/s for 5, 8, and 12 users

In order to evaluate the impact of the number of served users in the system, we also evaluated the proposed TSC with 8 users and 12 users with OWC connections at a data rate of 2.5 Gb/s and a beam width of 20 cm for 4-QAM modulation format. The BER performance of each user was measured for the 8-user case. As illustrated in Fig. 4.7, there is also no significant difference amongst the BER performance of all users, similar

to the 5-user case. More measurements were carried out with 12 users and the average BER for 12-user case was plotted in Fig. 4.8 together with that for 5 users and 8 users. Results show that the average BER does not degrade when the number of user increases. However, it is obvious that the data rate that can be provided to each individual decreases with more users when the system capacity is fixed.

We further improved the spectral efficiency (SE) and the system capacity by employing 16-QAM modulation format, where 5-user case was considered in proof-of-concept experiments for simplicity. The measured BER of each user at an aggregate bit rate of 4 Gb/s with respect to the distance from beam centre is shown in Fig. 4.9.

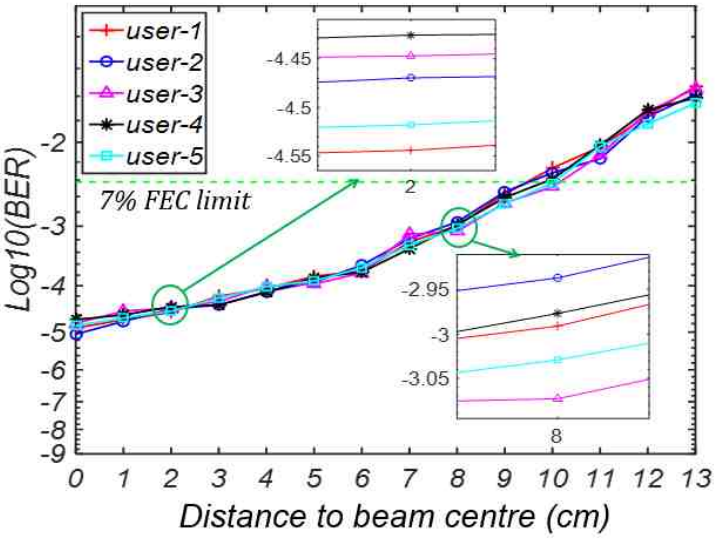

Fig. 4.9 BER performance (16-QAM) of each user with a beam width of 20 cm

There is a small variation in all the users' BER which is similar to the results of 4-QAM shown in Fig. 4.5. This can be attributed to the fairness of the TSC scheme regardless of the modulation format. We have also evaluated the performance of different system capacities, i.e. 4 Gb/s, 3.33 Gb/s, 2 Gb/s, 1 Gb/s and 0.4 Gb/s. The average BER of all five users for the corresponding aggregate data rate was plotted in Fig. 4.10. We can also observe that error-free coverage reduced with higher data rate.

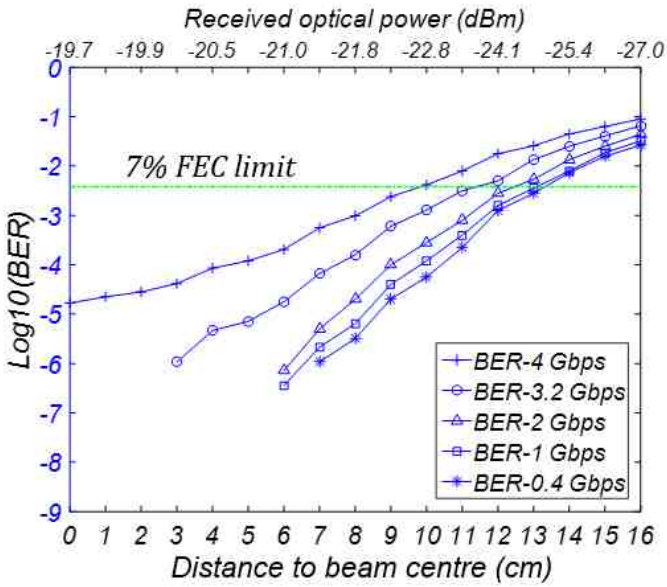

Fig. 4.10 Average BER performance (16-QAM) of 5 users under different system capacities and beam width of 20 cm

4.4 Adaptive Loading Function Demonstration

In the original TSC scheme, we compared error-free coverage using 16-QAM and that of 4-QAM with the beam width fixed at 20 cm under two conditions: the same symbol rate (1 Gbaud/s) and the same bit rate (2 Gb/s). The average BER based on 4-QAM for 5 users with 2 Gb/s (1 Gbaud/s) capacity is illustrated in Fig. 4.6 – (a) while the average BER results for 16-QAM in the 5-user case with 4 Gb/s (1 Gbaud/s) and 2 Gb/s are shown in Fig. 4.10. To improve the visibility and to quantitatively compare the two modulation formats, we re-plotted the results mentioned above in Fig. 4.11.

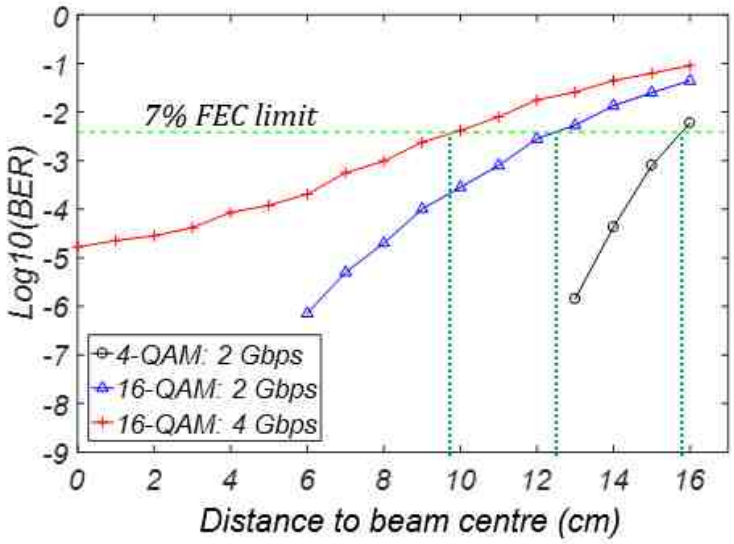

Fig. 4.11 Comparison between systems based on 16-QAM and 4-QAM with the same symbol rate and the same bit rate

It can be seen that the coverage provided by 16-QAM under both conditions (9.89 cm and 12.56 cm, respectively) is smaller than that based on 4-QAM, which is 15.79cm. Consequently, we modify the original TSC scheme to adaptively integrate both 4-QAM and 16-QAM modulation formats simultaneously so that the error-free coverage provided by a single transmitter can be further extended while serving more users with multiple data rates.

By employing the optical wireless localisation function [144], the knowledge of each user's location can be obtained. The transmitter is capable of assigning higher data rates with more spectral efficient advanced modulation format to users closer to the beam centre and lower data rates using lower modulation format to users further away from the beam centre. The 5-user case as illustrated in Fig. 4.12 is used as an example for ease of discussion. Here user-2, user-4 and user-5 who are located closer to the beam centre are assigned with 16-QAM modulated data, while user-1 and user-3 who are located further away are assigning 4-QAM modulation format.

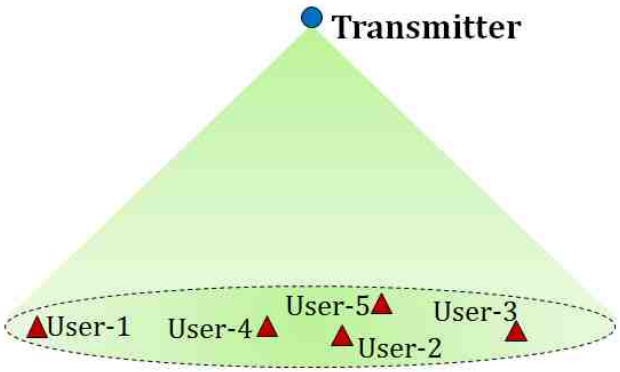

Fig. 4.12 Multi-user scenario for demonstration

In the experiment, two transmission strategies were evaluated via the experimental setup shown in Fig. 4.4. The first strategy (S_1) is that the minimum Euclidean distance of 4-QAM (d_1) is normalised to three times of that in 16-QAM (d_2), i.e. $d_1 = 3d_2$, to fully use the transmission power for both 4-QAM and 16-QAM; the other strategy (S_2) employs standard 4-QAM where both modulation formats have the same minimum Euclidean distance ($d_1 = d_2$), as shown in Fig. 4.13.

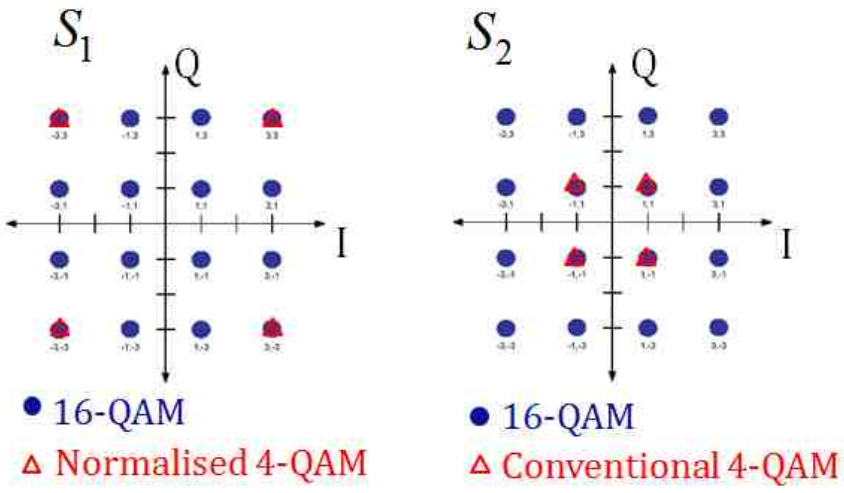

Fig. 4.13 Illustration of S_1 ($d_1 = 3d_2$) and S_2 ($d_1 = d_2$)

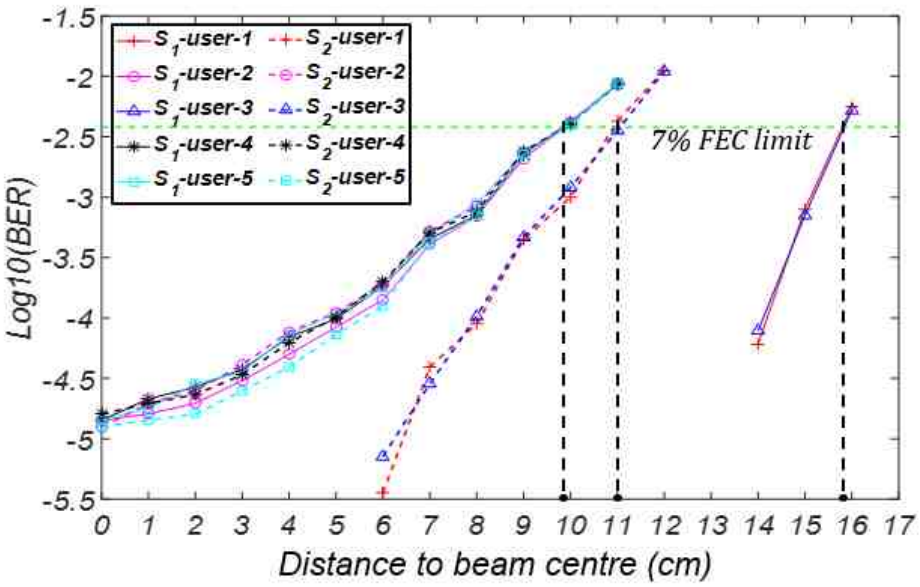

Fig. 4.14 The TSC BER performance of each user with adaptive loading function and a beam width of 20 cm, user-1 (4-QAM), user-2 (16-QAM), user-3 (4-QAM), user -4 (16-QAM), user-5 (16-QAM)

The BER curves of each user with these two strategies are illustrated in Fig. 4.14, where the symbol rate is 1 Gbaud/s. It can be observed that the performances of user-2, user-4 and user-5 served with 16-QAM do not vary noticeably from strategy S_1 to S_2. The results are similar to those of the original TSC scheme based on 16-QAM only, as shown in Fig. 4.11. Compared to the original TSC 16-QAM only, S_1 improves the error-free coverage by 61.2% and S_2 enlarges it by 12.2%. However, the system capacity decreases from 4 Gb/s to 3.2 Gb/s. It is intuitive that the more user served by 4-QAM, the less capacity the system can provide. Error-free coverage of around 11 cm provided by S_2 is smaller than that using purely 4-QAM (~15.79 cm in Fig. 4.11). This is because the 4-QAM modulation format in S_2 does not take full advantage of the transmission power due to the smaller minimum Euclidean distance. In addition, S_1 provides 15.81 cm error-free coverage, which is similar to that using 4-QAM only while the system capacity is increased from 2 Gb/s to 3.2 Gb/s. Evidently, there is a trade-off between total capacity and error-free coverage.

4.5 Code Misalignment Tolerance Analysis

In the previous sections, we have experimentally demonstrated the proposed TSC scheme with the ideal code set for indoor OWC system. As discussed in the principle of TSC scheme, active users can employ ideal time-slot code as shown in Fig. 4.15 – (a) and thus avoid the interference from each other by occupying non-overlapping time slots as shown in Fig. 4.15 – (b). During non-ideal hardware implementation procedures for code generation, however, timing issues can potentially lead to partial overlap within the time-slot code set as shown in Fig. 4.15 – (c). Consequently, it is imperative that performance degradation from code overlapping is critically investigated. In particular, we study the effect of the code overlapping ratio on the BER performance of a general square QAM modulation format, the analytical process can be transferred to other modulation formats. The advantage of using the proposed time-slot coding scheme as compared to the conventional time-division multiple access is also analysed in this section.

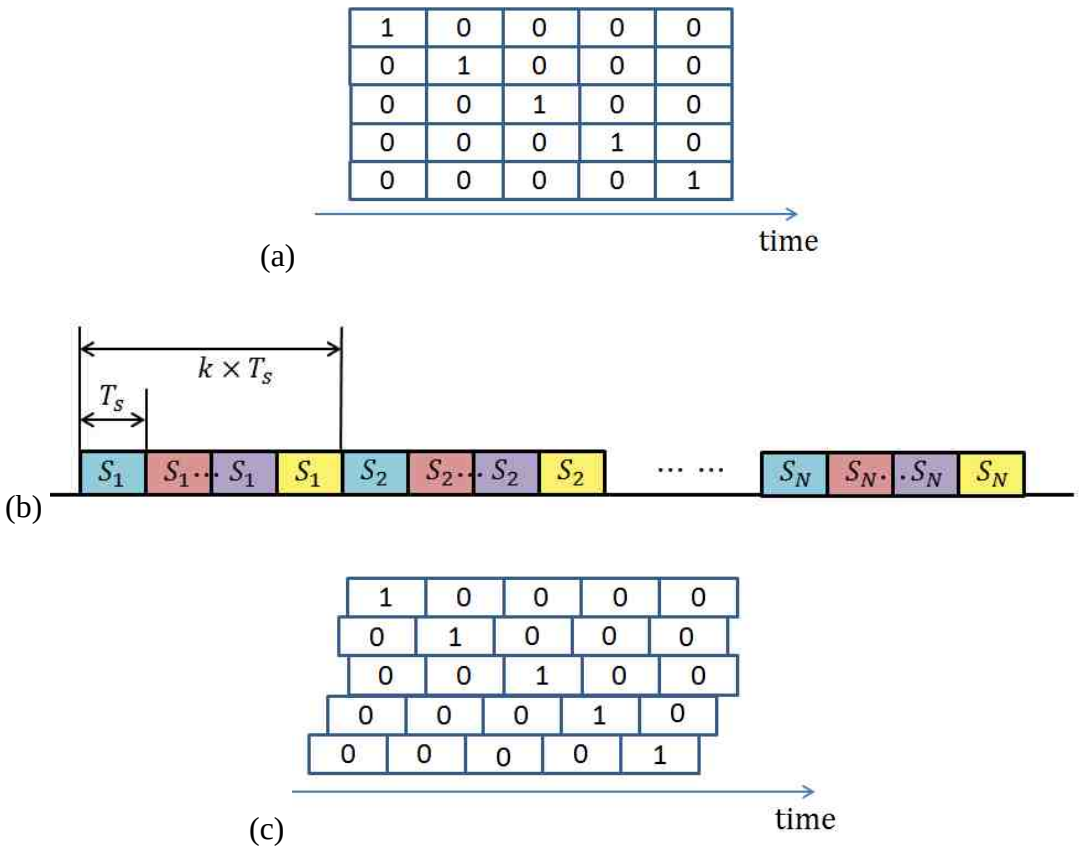

(d)

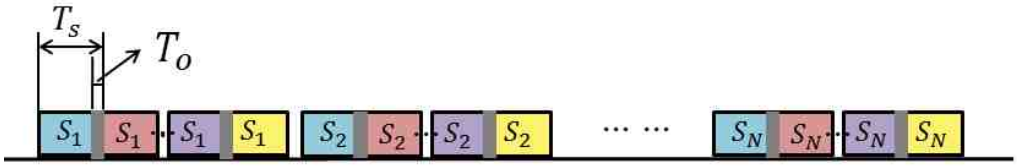

Fig. 4.15 (a) ideal code for 5-user case, (b) summed symbol sequence with ideal code, (c) code with misalignment issue, and (d) summed symbol sequence with code misalignment issue

4.5.1 Theoretical Analysis and Simulation Results

The summed symbol sequence when users employ the dedicated code with misalignment issue and the concept of code overlapping are illustrated in Fig. 4.15 – (d). The grey shaded area is the overlapping between neighbouring symbols and T_o denotes the total time duration of overlapping symbols from adjacent users. The overlapping ratio R_o is therefore defined as the ratio of the total overlapping period and the original symbol period:

$$R_o = \frac{T_o}{T_s}, \quad R_o \in [0,1] \tag{4.3}$$

The code misalignment tolerance is thus defined as the maximum value of R_o when error-free performance is still achieved. The received signal suffering from code overlapping after frequency down-conversion can be described as:

$$r_m = \sum_{j=-\infty}^{\infty} S \cdot (R_o^{\,j-1} v_c^{\,j-1} + v_c^{\,j} + R_o^{\,j+1} v_c^{\,j+1}) h(m - jT_s) + n_m \tag{4.4}$$

where S is the signal amplitude, R_o^{j-1} represents the overlapping ratio causing from the preceding symbol v_c^{j-1} while R_o^{j+1} is the overlapping ratio introduced by the following symbol v_c^{j+1}, and n_m is the noise introduced from the free space transmission and detection. The received p^{th} symbol of k^{th} user can be expressed as:

$$y_k[p] = S \cdot (R_o^{\,j-1} v_{k-1}^{\,p} + v_k^{\,p} + R_o^{\,j+1} v_{k+1}^{\,p}) + n' \tag{4.5}$$

where v_k^p represents the original p^{th} symbol of k^{th} user, v_{k-1}^p denotes the original p^{th} symbol of $(k\text{-}1)^{th}$ user and n' is the noise for one symbol. The value of overlapping percentage between locations of "1" within the time-slot code set can be different as shown in Fig. 4.15 – (c). However, once the code generation process is completed, the

superposition between adjacent symbols will be deterministic. That is because each symbol sequence of individual users is multiplied with the dedicated code chosen from the time-slot code set and then all symbol sequence are summed up, the partial superposition between adjacent symbols is fixed and determined by the existing overlapping percentage generated in the code generation process. The noise applied to the overlapped symbol sequence after detection is assumed to follow a Gaussian distribution.

Consequently, the analytical model derived in the previous chapter can be further manipulated to accommodate the received signal containing both code misalignment interference and the noise from transmission and detection in the system. Here, we provide an example to show the process of derivation of SER with code overlapping ratio:

For simplicity, two users with 4-QAM modulation format are considered. Since the four *I*-*Q* quadrants are symmetrical, Fig. 4.16 only shows the first quadrant for explanation.

Step – 1: After the code generation process, the overlapping ratio R_o is fixed. The symbol (1, 1) is possibly overlapped by all four symbol patterns in 4-QAM modulation format. As illustrated in Fig. 4.16 – (a), the green star represents the original symbol while the red icons with four shapes (rhombus, square, triangle, and circle) represent the ideal overlapped symbols without system noise, respectively. For example, the original symbol (1, 1) is overlapped by another symbol (1, -1) with the percentage of R_o, the resultant overlapped symbol can be then expressed as $(1 + 1 \cdot R_o, 1 - 1 \cdot R_o)$.

Step – 2: Fig. 4.16 – (b) shows the noisy version of overlapped symbols after transmission and detection. Noise around each ideal overlapped symbol follows 2-D Gaussian distribution $f(x, y)$ where variables x and y are independent and have the same Gaussian distribution with zero mean and standard deviation σ.

Step – 3: As illustrated in Fig. 4.16 – (c), take one ideal overlapped symbols, e.g. $(1 - 1 \cdot R_o, 1 - 1 \cdot R_o)$, as the origin of a new x-y coordinate. Similarly with the derivative step introduced in Section 3.3.1, the rate that received symbols are able to be correctly demodulated as symbol (1, 1), which is denoted as R_1, can be calculated by taking an integration of both x and y over the decision region of the reference symbol (1, 1) as shown in the green-dash-line region:

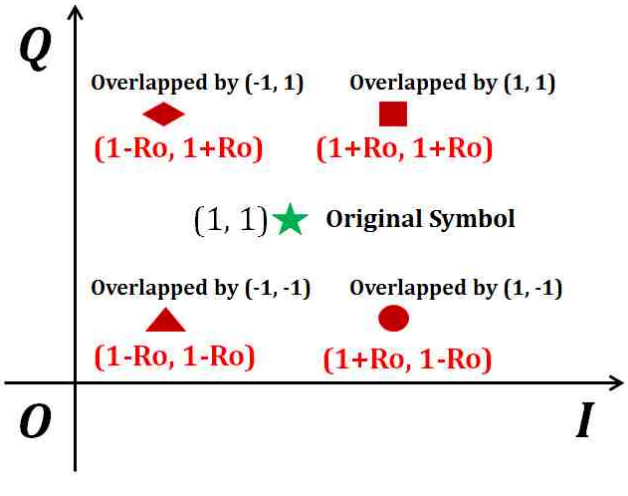

(a)

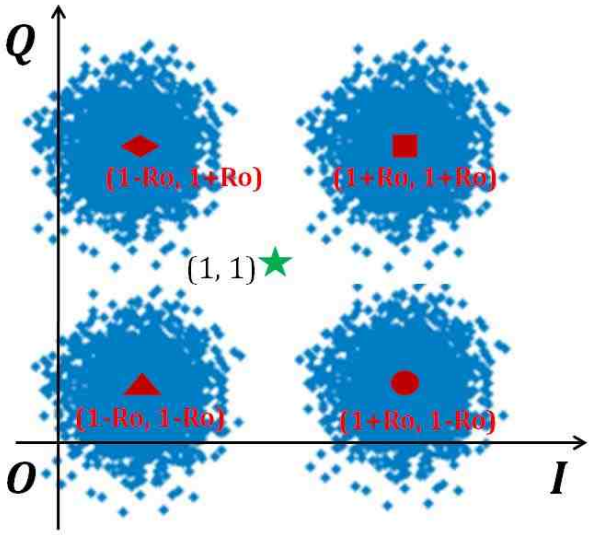

(b)

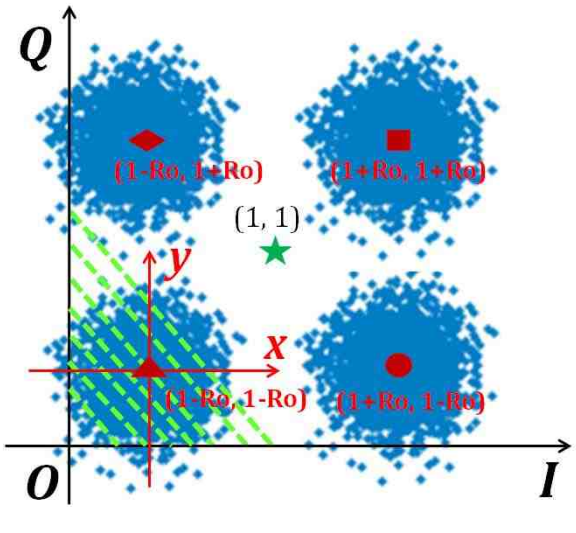

(c)

Fig. 4.16 Illustration for SER derivation example

$$R_1 = \int_{-(1-R_o)}^{\infty}\int_{-(1-R_o)}^{\infty} f(x,y)\,dxdy \tag{4.6}$$

Step – 4: Apply the same procedures as described above to the other three ideal overlapped symbols and also to the rest of quadrants, SER with overlapping ratio for 4-QAM modulation format can be calculated as:

$$SER_{4-QAM}(R_o,\sigma) = 1 - \frac{1}{4}\sum_{I,Q}\int_{-(1+I\cdot R_o)}^{\infty}\int_{-(1+Q\cdot R_o)}^{\infty} f(x,y)\,dxdy \tag{4.7}$$

where *I* and *Q* can be either 1 or -1 in 4-QAM modulation format.

Consequently, the symbol error rate for a general 2^{2l} – ary QAM is derived in Eq. (4.8) $f(x, y)$ is the probability density function of the received signal position. As discussed in Section 3.3.2 especially in Eq. (3.18) is dependent on the signal-to-noise ratio (SNR) and a smaller σ corresponds to a larger SNR and vice versa.σ corresponds to a larger SNR and vice versa.

$$\begin{aligned} SER(l,R_o,\sigma) &= 1 - \frac{4}{\left(2^{2l}\right)^2}\left[\begin{array}{l} \sum_{c=1,d=1}\sum_{I_2,Q_2}\int_{Q_{1,d}-1-y_{N,d}}^{Q_{1,d}+1-y_{N,d}}\int_{I_{1,c}-1-x_{N,c}}^{I_{1,c}+1-x_{N,c}} f(x,y)\,dxdy \\ +2\sum_{c=1,d=2}\sum_{I_2,Q_2}\int_{Q_{1,d}-1-y_{N,d}}^{\infty}\int_{I_{1,c}-1-x_{N,c}}^{I_{1,c}+1-x_{N,c}} f(x,y)\,dxdy \\ +\sum_{c=2,d=2}\sum_{I_2,Q_2}\int_{Q_{1,d}-1-y_{N,d}}^{\infty}\int_{I_{1,c}-1-x_{N,c}}^{\infty} f(x,y)\,dxdy \end{array}\right] \\ &= 1 - \frac{4}{\left(2^{2l}\right)^2}\left[\begin{array}{l} \sum_{c=1,d=1}\sum_{I_2,Q_2}\left(F\left(Q_{1,d}+1-y_{N,d},\sigma\right)-F\left(Q_{1,d}-1-y_{N,d},\sigma\right)\right)\cdot \\ \left(F\left(I_{1,c}+1-x_{N,c},\sigma\right)-F\left(I_{1,c}-1-x_{N,c},\sigma\right)\right) \\ +2\sum_{c=1,d=2}\sum_{I_2,Q_2} F\left(-\left(Q_{1,d}-1-y_{N,d}\right),\sigma\right)\cdot \\ \left(F\left(I_{1,c}+1-x_{N,c},\sigma\right)-F\left(I_{1,c}-1-x_{N,c},\sigma\right)\right) \\ +\sum_{c=2,d=2}\sum_{I_2,Q_2} F\left(-\left(Q_{1,d}-1-y_{N,d}\right),\sigma\right)\cdot F\left(-\left(I_{1,c}-1-x_{N,c}\right),\sigma\right) \end{array}\right], \end{aligned}$$

$$F(\omega,\sigma) = \int_{-\infty}^{\omega}\frac{1}{\sigma\sqrt{2\pi}}\exp\left(-\frac{x^2}{2\sigma^2}\right)dx \tag{4.8}$$

In Eq. (4.8)$I_{1,c}$, $Q_{1,d}$, I_2 and Q_2 are expressed as follows for a general square 2^{2l} – ary QAM modulation format where *l* is a natural number, i.e. 1, 2, 3, etc.: is a natural number, i.e. 1, 2, 3, etc.:

$$
\begin{aligned}
I_{1,1} &= 2a-1-2^l, \quad 2^{l-1} < a < 2^l \\
Q_{1,1} &= 2b-1-2^l, \quad 2^{l-1} < b < 2^l \\
I_{1,2} &= 2^l - 1 \\
Q_{1,2} &= 2^l - 1 \\
I_2 &= 2p-1-2^l, \quad 1 \le p \le 2^l \\
Q_2 &= 2q-1-2^l, \quad 1 \le q \le 2^l
\end{aligned}
\tag{4.9}
$$

where *a*, *b*, *p* and *q* are natural numbers. The notation of $x_{N,c}$ and $y_{N,c}$ for time-slot coding scheme with code overlapping is derived as:

$$
\begin{aligned}
x_{N,c} &= I_{1,c} + R_o I_2 \\
y_{N,d} &= Q_{1,d} + R_o Q_2 \\
c, d &= 1, 2
\end{aligned}
\tag{4.10}
$$

where ($I_{1,c}$, $Q_{1,d}$) is denoted as the user's original symbol, (I_2, Q_2) can be considered as the symbol that partially overlaps with the original symbol due to code misalignment issue.

In order to analyse the advantage of using the time-slot coding scheme as compared to the conventional time-division multiple access technique, we further derive the SER equation for the conventional TDMA with imperfectly synchronised timing window when obtaining symbol data. In order to make a fair comparison, no guard interval is included in either TSC or TDMA implementations. The scenario with timing issue for TDMA is described in Fig. 4.17, where *k* users each with *N* symbols are considered and R_o is defined as in Eq. (4.3)

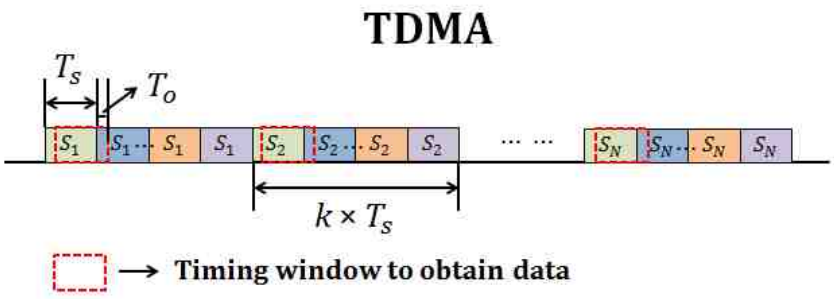

Fig. 4.17 The conventional TDMA with unsynchronised timing window when acquiring symbol data at the receiver side

Following the same convention, $x_{N,c}$ and $y_{N,c}$ for the conventional TDMA with imperfectly synchronised timing window can be derived as:

$$\begin{aligned} x_{N,c} &= (1-R_o)I_{1,c} + R_o I_2 \\ y_{N,d} &= (1-R_o)Q_{1,d} + R_o Q_2 \\ c,d &= 1,2 \end{aligned} \tag{4.11}$$

By respectively substituting Eq. (4.10)(4.11), SER with overlapping ratio (4.8) for the TSC scheme and the conventional TDMA can be calculated. The analytical SER results for both 4-QAM and 16-QAM modulation formats are plotted in Fig. 4Fig. 4.18is fixed as 0.08 to indicate the same signal-to-noise ratio for transmission and detection for both TSC and TDMA implementations. for transmission and detection for both TSC and TDMA implementations.

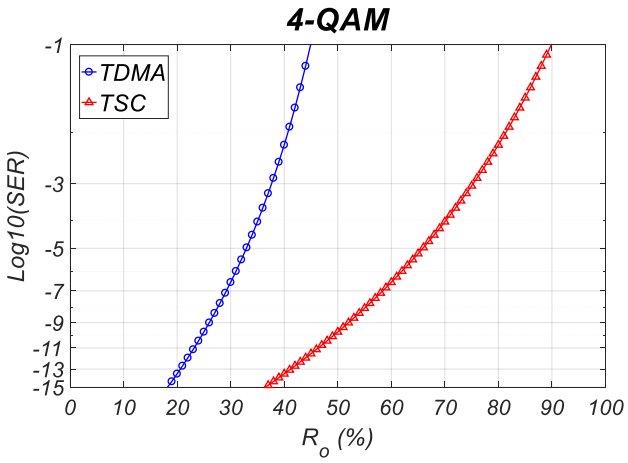

(a)

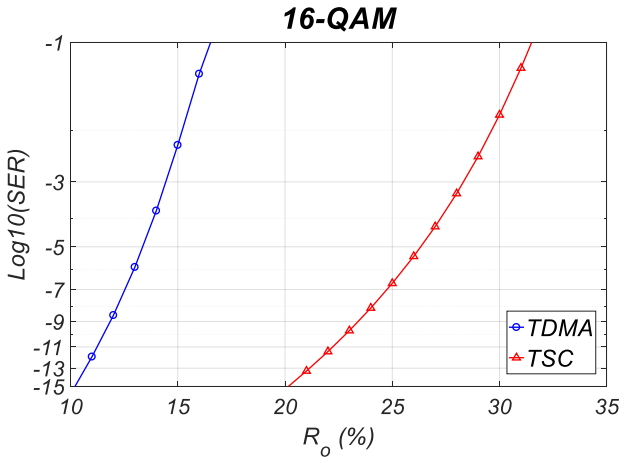

(b)

Fig. 4.18 Analytical SER performance of TSC and conventional TDMA with R_o and σ = 0.08 for (a) 4-QAM and (b) 16-QAM

From the analytical results, it can be seen that the proposed TSC scheme is much more tolerant to partial overlapping between adjacent symbols than the conventional TDMA. The reason arises from the difference of the received symbol sequence with imperfect timing/overlapping between the proposed TSC scheme and the conventional TDMA. In applications using the TSC scheme, the user is able to obtain its own entire symbol with the partial overlapping from the adjacent interfered symbol. In contrast, the user implemented with the conventional TDMA obtains partial own symbol and overlapping from the adjacent interfered symbol. What is more, imperfect timing issues during the non-ideal hardware implementation procedures for code generation is though less likely to happen than that during data acquiring process at the receiver side in the conventional TDMA, especially in high-speed communications.

With showing that TSC is superior over the conventional TDMA in terms of R_o tolerance when no guard interval is added to either scheme, we further link SER with BER for TSC scheme. As discussed in Eq. (3.26) Fig. 3.3 ($\alpha = SER/BER$ for 2^{2l} – ary QAM modulation with gray coding is dependent on the energy per bit to noise power spectral density ratio (E_b/N_0 The next step to link SER with BER is to find E_b/N_0 in TSC scheme which is affected by code overlapping issue. Since E_b/N_0 can be expressed in terms of root-mean-square (*RMS*) average of error vector magnitude (EVM_{RMS} as in Eq. (4.12), Eq. (3.17) (3.27) and Eq. (3.28):

$$\frac{E_b}{N_0} \approx \frac{1}{2l \cdot EVM_{RMS}^2} \tag{4.12}$$

We further derive EVM_{RMS} with code overlapping ratio in TSC scheme. The definition of EVM_{RMS} is consistent as shown in Eq. (3.12) I_n and Q_n are in-phase and quadrature parts of the received symbol with partial overlapping from adjacent symbols and noise from transmission and detection, respectively. The received symbol can be expressed as:. The received symbol can be expressed as:

$$I_n + iQ_n = \left(I_{0,n} + iQ_{0,n}\right) + R_o \cdot \left(I'_{0,n} + iQ'_{0,n}\right) + \left(N_I + iN_Q\right) \tag{4.13}$$

Thus, I_n and Q_n are given by:

$$\begin{aligned} I_n &= I_{0,n} + R_o \cdot I'_{0,n} + N_I \\ Q_n &= Q_{0,n} + R_o \cdot Q'_{0,n} + N_Q \end{aligned} \tag{4.14}$$

where $I_{0,n}$ is the in-phase component of the original symbol and $Q_{0,n}$ is the quadrature part. The symbol that partially overlaps with the original symbol is denoted as $\left(I'_{0,n}, Q'_{0,n}\right)$. The notations of N_I and N_Q are normalised noise in in-phase and quadrature components, respectively. Consequently, EVM_{RMS} can be rewritten as:

$$\begin{aligned} EVM_{RMS} &= \sqrt{\frac{E\left[\left|R_o \cdot I'_{0,n} + N_I\right|^2 + \left|R_o \cdot Q'_{0,n} + N_Q\right|^2\right]}{P_{avg}}} \\ &= \sqrt{\frac{E\left[R_o^2 \cdot \left(I'^{\,2}_{0,n} + Q'^{\,2}_{0,n}\right)\right] + E\left[2R_o \cdot \left(I'_{0,n} \cdot N_I + Q'_{0,n} \cdot N_Q\right)\right] + E\left[N_I^2 + N_Q^2\right]}{P_{avg}}} \end{aligned} \tag{4.15}$$

As the in-phase and quadrature parts of 2-D noise over *I*-*Q* plane are assumed to have the same distribution with zero mean, Eq. (4.15)with the aid of Eq. (3.15) as:

$$\begin{aligned} EVM_{RMS}\left(l, R_o, \sigma\right) &= \sqrt{\frac{R_o^2 \cdot P_{avg} + 0 + 2\sigma^2}{P_{avg}}} \\ &= \sqrt{R_o^2 + \frac{3\sigma^2}{4^l - 1}} \end{aligned} \tag{4.16}$$

Combining Eq. (4.12)(4.16)modulation format dependent E_b/N_0 described in terms of overlapping ration and standard deviation as:

$$\frac{E_b}{N_0}\left(l, R_o, \sigma\right) = \frac{1}{2l \cdot \left(R_o^2 + \frac{3\sigma^2}{4^l - 1}\right)} \tag{4.17}$$

The BER is consequently linked with SER using Eq. (3.26)(4.17), and is shown as:

$$BER(l,R_o,\sigma)$$

$$=\frac{1}{\alpha}-\frac{4}{\alpha\left(2^{2l}\right)^2}\left[\begin{array}{l}\sum_{c=1,d=1}\sum_{I_2,Q_2}\left(F\left(Q_{1,d}+1-y_{N,d},\sigma\right)-F\left(Q_{1,d}-1-y_{N,d},\sigma\right)\right)\cdot \\ \left(F\left(I_{1,c}+1-x_{N,c},\sigma\right)-F\left(I_{1,c}-1-x_{N,c},\sigma\right)\right) \\ +2\sum_{c=1,d=2}\sum_{I_2,Q_2}F\left(-\left(Q_{1,d}-1-y_{N,d}\right),\sigma\right)\cdot \\ \left(F\left(I_{1,c}+1-x_{N,c},\sigma\right)-F\left(I_{1,c}-1-x_{N,c},\sigma\right)\right) \\ +\sum_{c=2,d=2}\sum_{I_2,Q_2}F\left(-\left(Q_{1,d}-1-y_{N,d}\right),\sigma\right)\cdot F\left(-\left(I_{1,c}-1-x_{N,c}\right),\sigma\right)\end{array}\right]$$

$$F(\omega,\sigma)=\int_{-\infty}^{\omega}\left[1/\left(\sigma\sqrt{2\pi}\right)\right]\exp\left(-x^2/2\sigma^2\right)dx$$

(4.18)

where $x_{N,c}$ and $y_{N,c}$ are expressed in Eq. (4.10)$I_{1,c}$, $Q_{1,d}$, I_2 and Q_2 are shown in Eq. (4.9).

According to Eq. (4.18)R_o and σ for 4-QAM and 16-QAM are presented in Fig. 4.19. It is intuitively shown that higher noise from transmission and detection and larger overlapping ratio contribute to worse performance. When Ro is relatively small, receiver noise dominates in BER degradation; however, when Ro becomes larger, BER degradation is dominated by the partial superposition. Also, 4-QAM modulated data is able to tolerate more overlapping from adjacent users compared to 16-QAM modulation format. The experimental demonstration of tolerance analysis is provided in Section 4.4.2.

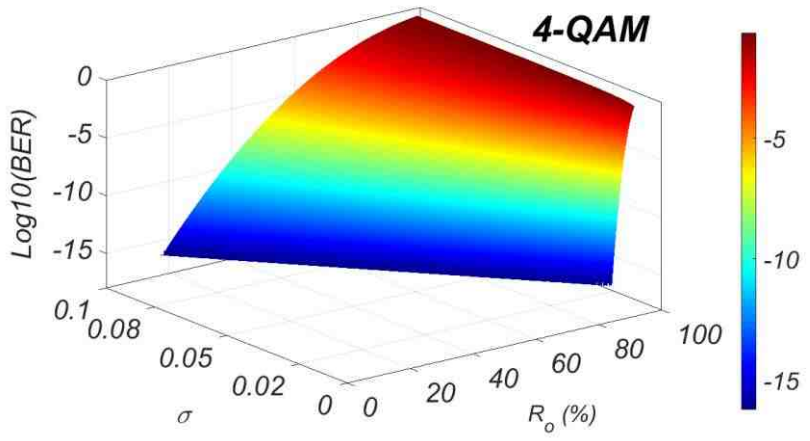

(a)

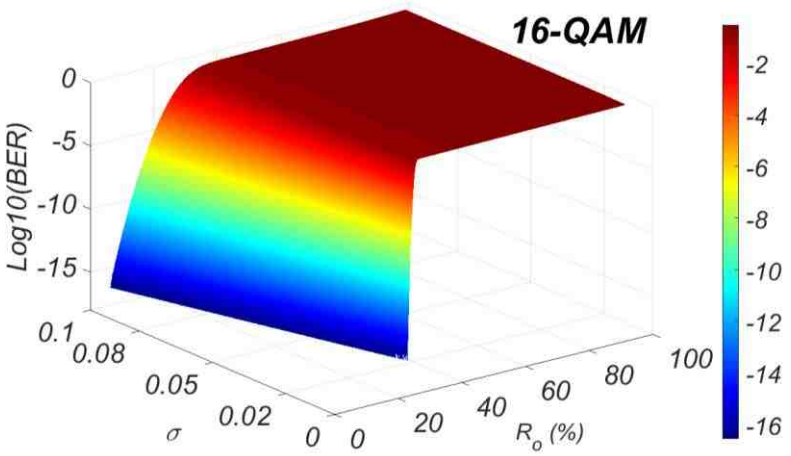

(b)

Fig. 4.19 Analytical BER performance with R_o and σ for (a) 4-QAM and (b) 16-QAM.

4.5.2 Experimental Verification

The tolerance of code overlapping was further investigated using the experimental setup shown in Fig. 4.4 with a beam width of 20 cm at the receiver plane. For simplicity, only two users were considered for demonstration. Each time-slot code was upsampled by 20 times to emulate the code bit period. We generated two users' data with different overlapping ratio in MATLAB and sent them to the AWG for transmission, respectively. Both 4-QAM and 16-QAM modulation formats were evaluated and the background light incorporated in the experiment was about -28.63 dBm. Fig. 4.20 shows the measured BER performance for neighbouring users as a function of the overlapping ratio at three different distances from the beam centre, i.e. 0 cm, 5 cm and 10 cm. The figure also shows the BER calculated from theoretical analysis using Eq. (4.18).

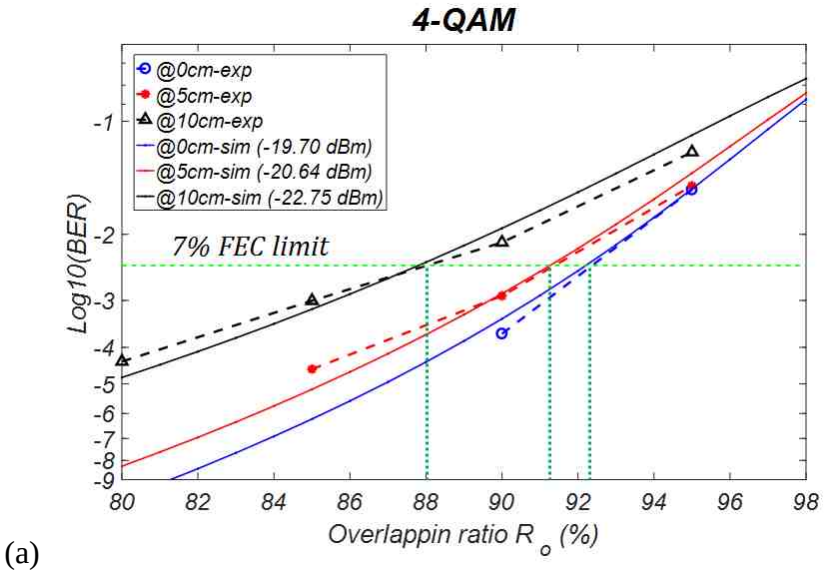

(a)

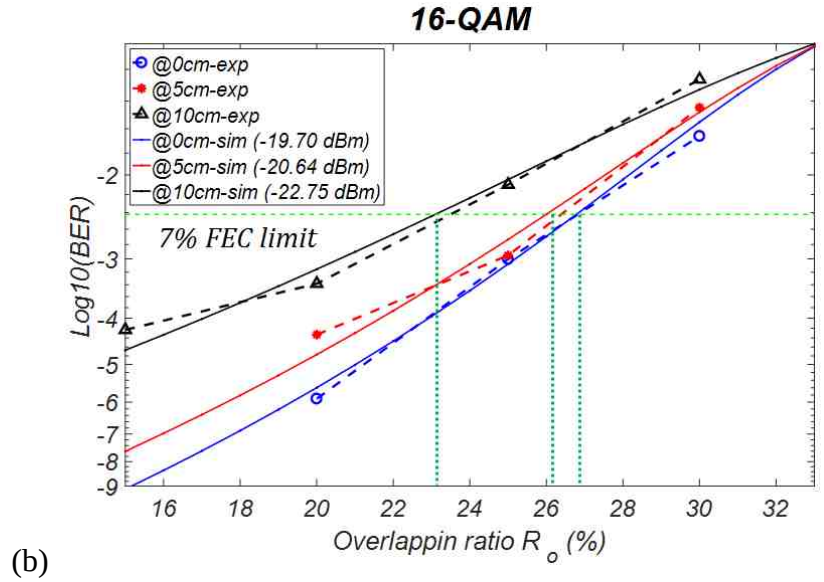

(b)

Fig. 4.20 BER performance at three locations with increased overlapping ratio based on (a) 4-QAM and (b) 16-QAM

It can be seen that for 4-QAM modulation format, the overlapping tolerance is 92.3%, 91.1%, and 88% when the user locates at 0 cm, 5 cm and 10 cm from the beam centre, respectively. In terms of 16-QAM modulation format, the tolerance is 26.9%, 26.1% and 23.2%, respectively. The error-free threshold is selected at the 7% FEC limit (BER $\leq 3.8 \times 10^{-3}$). We can observe that the experimental results are consistent with the theoretical calculation based on Eq. (4.18)decreases when user moves further away from beam centre. This is because that SNR degrades with decreased received optical power while the noise level does not differ much. Furthermore, compared to the

tolerance results based on 4-QAM modulation format, the TSC system with 16-QAM is less immune to code misalignment due to a more complex signal constellation.

4.6 Conclusions

In this chapter, the principle of the proposed TSC scheme for high speed multiple access in indoor OWC system has been introduced. We have developed and demonstrated the TSC scheme for 4-QAM modulation format and 16-QAM modulation format to improve the system capacity as well as the spectral efficiency. The proof-of-concept experiments have been conducted for 5-user, 8-user and 12-user with multiple data rates. When the number of users increases, the experimental results have shown that the BER performance for a certain system capacity is not affected by the number of users. The system has also shown the capability of providing multiple data rates to different users. The adaptive loading function of the original TSC scheme, where both 4-QAM and 16-QAM were simultaneously employed and selectively assigned to different users according to their locations, has also been experimentally demonstrated. Experimental results have shown that error-free coverage can be extended by 61.2% when users further away from the beam centre are modulated with 4-QAM. By using the proposed TSC scheme with adaptive loading function, the issues of requiring heavy overheads in discrete multitoned (DMT) modulation and code redundancy in rate adaptive coding (RAC) are alleviated. What is more, switching between different modulation formats and synchronisation problem in time-division hybrid modulation formats (TDHMF), as discussed in Section 2.3.3, can be eliminated by applying our time-slot code. The theoretical analysis of code misalignment issue and the effect on the performance of the TSC scheme based indoor OWC system has been verified with a general square QAM modulation format. Experimental results have highlighted that code misalignment tolerance larger than 26.9% with 16-QAM and 92.3% with 4-QAM modulation format can be achieved with a received optical power of more than -19.7 dBm.

Chapter 5 Enabling Physical Layer Security with Chaotic Phase Terms as Security Codes

5.1 Introduction

In the previous chapter, an effective multi-user access framework termed as time-slot coding (TSC) scheme has been proposed for indoor OWC system and experimentally shown to support multiple users simultaneously without sophisticated long-length codes or strict synchronisation requirements. However, communication security in OWC systems, especially supporting multiple user access, has yet to be widely studied. It is widely known that OWC has the ability to offer secure communications physically since an optical wave with short wavelength cannot penetrate objects such as walls in its transmission path [8]. However, such security is only considered practical for point-to-point links with narrow optical beams. When multiple users are covered within a single but wider optical beam, security issues arise, such as eavesdropping, tampering, imitation, forgery, etc [145]. Our focus in this chapter is on alleviating eavesdropping, which is one of the most widely existing issues in multi-user telecommunication systems. For example, in the TSC-based multi-user OWC system, each active user has the opportunity to eavesdrop messages from other users simply by shifting the location of code bit "1" in the time-slotted code. Hence, secure and private multiple-access cannot be guaranteed.

Based on limited literature of secure connections in OWC including visible light communications (VLC), the nulling strategy studied in [116, 117] fails to simultaneously offer both multiple access and security. A code-division multiple access

VLC system employing chaotic sequence to generate the spreading codes has been proposed in [118] and security has been enhanced by advanced encryption standard, at the cost of extra bandwidth and complex signal processing. To solve these issues, we present and demonstrate an indoor OWC system employing the TSC scheme together with chaotic phase added to each user's symbol data as a security code providing secure OWC connectivity for the transmitter (Alice) to the intended user (Bob). In such a system, the TSC scheme provides a stable interference-free multi-user access and the chaotic phase terms introduced over the entire signal constellation plane prevents unauthorised users from eavesdropping other channels. We use the logistic map iterative sequence derived with unique values for the initial value x_1 and the constant parameter r for each user. Most importantly, our proposed secure system does not require additional bandwidth and has no performance degradation on the original symbol quality. In addition, blind equalisation can be avoided as an option for the eavesdropper due to the chaotic manner, and the chaotic phase over the entire signal constellation plane makes the system resistive to brute force or exhaustive search of computation to identify the security key.

In this chapter, we first investigate the feasibility of a physical layer security mechanism using the chaotic phase. Power penalty introduced by the chaotic phase for legitimate user is experimentally demonstrated with multiple data rates based on both 4-QAM and 16-QAM modulation formats. The results show that signal quality of each legitimate user is not degraded by the chaotic phase. Furthermore, by analysing the performance of eavesdroppers without prior knowledge of the security key realised with the chaotic phase terms for each user, we demonstrate the effectiveness of the eavesdropper's inability to receive the transmitted data. In particular, as this mechanism realises the security key in the form of two unique values (r and x_1), the potential eavesdropper could theoretically conduct exhaustive searching for a set of r and x_1 that provides best performance, and thus may potentially be able to intercept Bob's information. Consequently, the sensitivity of the security key needs to be further evaluated, in particular to the extent that information needs to be close to the original value to achieve potential detection. At the same time, tolerance to the time-slot code misalignment incorporating chaotic phase requires investigation as it affects multi-user interferences substantially. For the first time, we provide comprehensive theoretical analysis and experimentally investigate these key aspects and demonstrate a robust and secure

indoor OWC system supporting multiple users. Experimental results show that the proposed mechanism is still valid even under eavesdropper's high searching accuracy of 10^{-10}, demonstrating transmission based on both 4-QAM and 16-QAM modulation formats. The code misalignment tolerance is shown to be high as well, where 68.6% and 22.6% misalignment tolerance is achieved for 4-QAM and 16-QAM modulated signals, respectively, at the received optical power over -20 dBm.

The rest of the chapter is organised as follows:

Section 5.2 introduces the principle of the proposed security key and its generation process of the chaotic sequences within a multi-user environment implementation of the system architecture and its feasibility to secure the transmission. In Section 5.3, proof-of-concept experiments are carried out to demonstrate the security capability for multiple users. Section 5.4 provides comprehensive investigation on robustness of the proposed mechanism based on both theoretical and experimental results.

5.2 Principle of Secure Multiple Access with Chaotic Phase

5.2.1 System Architecture

The architecture of the proposed indoor optical wireless system supporting secure multi-user access is described in Fig. 5.1. As illustrated, the data bits are firstly generated for k users and then mapped into symbol patterns. In this study, we adopt QAM modulation formats as the preferred method to achieve high bandwidth downstream links. The number of phase terms in the phase sequence is the same as the number of symbols for an individual user (N). After applying each phase term to the corresponding symbol, the i^{th} user's secured symbol sequence is multiplied with the unique k-bit time slotted code which is the i^{th} row of the identity matrix with the size of k, where k is the number of users as shown in Eq. (4.1).

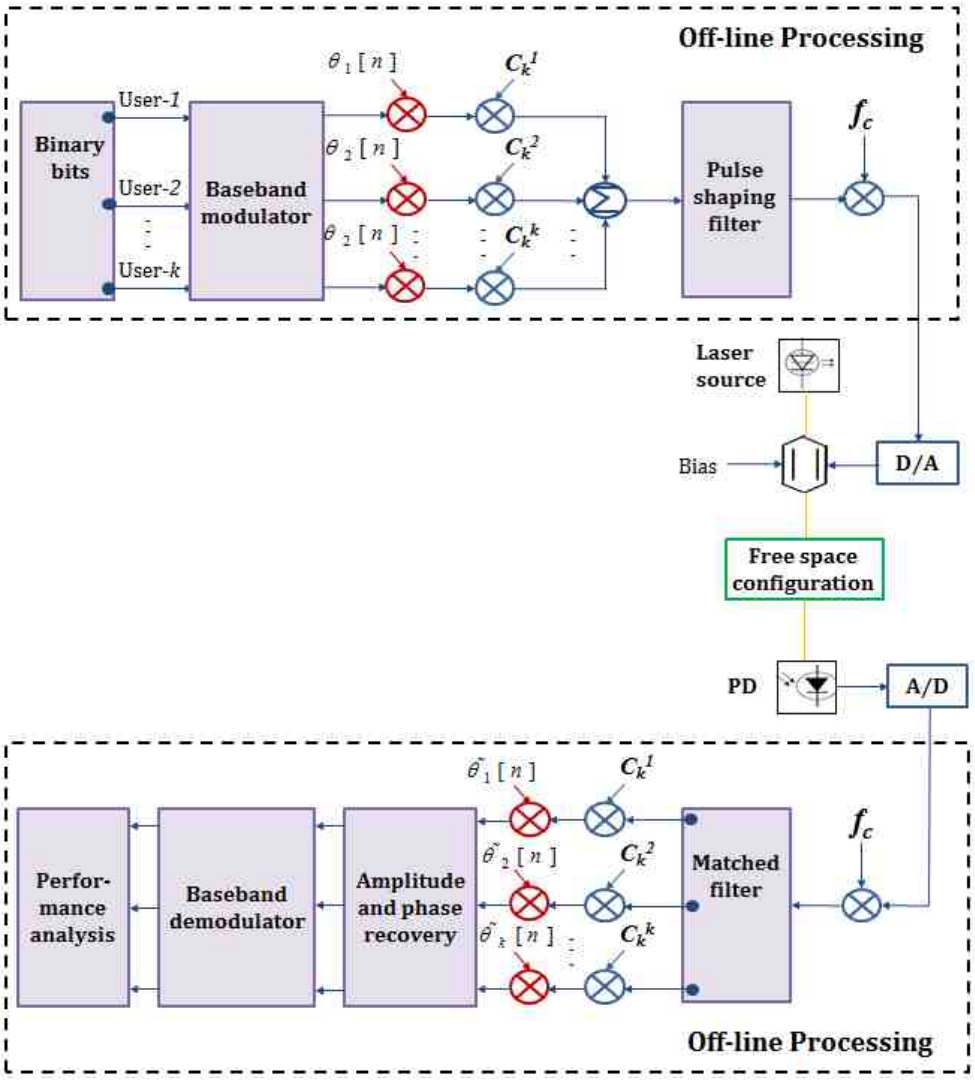

Fig. 5.1 Block diagram of secure OWC with TSC and chaotic phase

By employing the dedicated time-slot code, each user occupies non-overlapping specific symbol slots to avoid inter-user interference. The coded symbol sequences are summed up before passing through a pulse shaping filter for upsampling. The baseband signal is then up-converted to a carrier frequency f_c and is completed with the digital-to-analog conversion (DAC). The optical source is modulated by the electrical signal via an external modulator.

At the receiver side, the optical signal along with the background light is captured by the photodiode (PD) after free space transmission. The output of PD is converted to digital signal for post-processing. Each user receives the entire signal sequence which is firstly down-converted and passed through a matched filter for downsampling and

filtering out of the baseband signal. The signature time slot code is then applied to extract intended symbols for each user. Next, the artificial phase noise is cancelled by employing a phase compensation using the negative value of the original chaotic phase term used at the transmission side. Lastly, amplitude and phase changes introduced from transmission are recovered before demodulating the baseband signals and completing the evaluation of transmission and detection performance metrics.

5.2.2 Chaotic Phase Generation

The secure OWC connections in our work are provided by adding artificial phase noise to each symbol. In order to simplify the procedures for the end users to generate exactly the same phase as the transmitter, we employ a logistic map to build the chaotic sequence. The logistic map is mathematically written as:

$$\begin{aligned} x_{i+1} &= r x_i (1 - x_i). \\ r \in [0,4], \quad x_1 &\in (0,1). \end{aligned} \tag{5.1}$$

where r is a constant parameter and x_1 is the initial element. Since the chaotic manner of logistic map presents for r larger than 3.57 [146], the values of r ranging from 3.57 to 4 are considered in our work. After multiplying by 360 degrees, phases over the entire *I*-*Q* plane are generated as:

$$\theta[n] = 360 \cdot x[n], \quad n = 1, 2, \ldots, N. \tag{5.2}$$

where $x[n]$ is the original sequence generated from the logistic map, $\theta[n]$ is the phase sequence for *I*-*Q* plane and N is the number of symbols of each user, Each phase term is applied to the corresponding symbol by the transmitter, and then the original symbol sequence is encrypted by the chaotic sequence. Since reference symbols in a general QAM modulation format have typical decision region, in order to add phase noise, the chaotic phase sequence is expected to move the transmitted symbol outside the corresponding decision region of the reference symbol. Consequently, the resulting impact of additional phase noise is further evaluated.

5.2.3 Feasibility Analysis

As illustrated in Fig. 5.2, the range of phase noise terms falling within the decision region for a specific reference symbol is described by the summation of two angles – β and γ, since the amplitude of the symbol in our proposed system is not changed by introducing the chaotic phase terms.

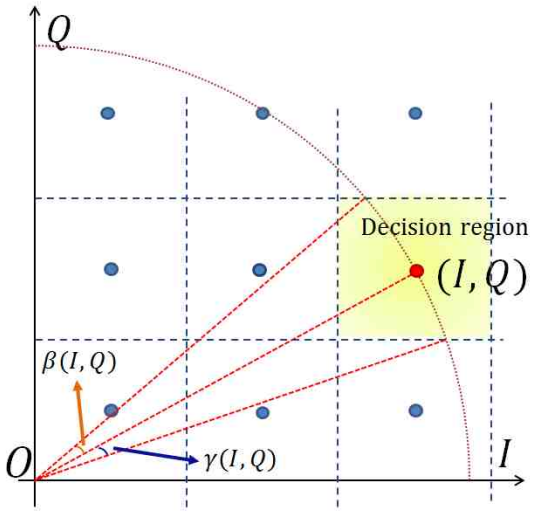

Fig. 5.2 Signal constellation for a general square QAM

Due to the symmetry of signal constellation, the impact is only illustrated for the first quadrant. For a reference symbol defined by its (I, Q) values in a general square M – ary QAM ($M = 2^{2l}$, $l = 1, 2, 3\ldots$) modulation format, β and γ can be derived (details presented in Appendix B) as:

$$\beta(I,Q)=\begin{cases}\cos^{-1}\dfrac{I^2-I+Q\sqrt{I^2+Q^2-(I-1)^2}}{I^2+Q^2}, & I\le Q\\ \cos^{-1}\dfrac{Q^2+Q+I\sqrt{I^2+Q^2-(Q+1)^2}}{I^2+Q^2}, & I>Q\end{cases}$$
$$\gamma(I,Q)=\begin{cases}\cos^{-1}\dfrac{I^2+I+Q\sqrt{I^2+Q^2-(I+1)^2}}{I^2+Q^2}, & I<Q\\ \cos^{-1}\dfrac{Q^2-Q+I\sqrt{I^2+Q^2-(Q-1)^2}}{I^2+Q^2}, & I\ge Q\end{cases} \tag{5.3}$$

where in-phase (I) and quadrature (Q) components are generalised as:

$$\begin{aligned} I &= 2a-1-2^{l}, \quad 1 \le a \le 2^{l} \\ Q &= 2b-1-2^{l}, \quad 1 \le b \le 2^{l} \end{aligned} \tag{5.4}$$

The parameters *a* and *b* are natural numbers (1, 2, 3, etc.). In order to add phase noise terms, the added chaotic phase should satisfy:

$$\beta(I,Q) < \theta[n] < 360^{\circ} - \gamma(I,Q) \tag{5.5}$$

As a result, the noise rate is defined as the percentage of added phase noise terms that satisfy Eq. (5.5), i.e. have the capability to move the original symbol outside the corresponding decision region, and is expressed as:

$$\mathrm{P}_{noisy} = \frac{1}{4^{l-1}} \sum_{I,Q} P\left(\beta(I,Q) < \theta[n] < 360^{\circ} - \gamma(I,Q)\right) \tag{5.6}$$

where *P* (.) is calculated as the ratio of the number of phase terms that satisfy the condition shown in Eq. (5.5)phase terms, which is equal to the number of symbols of each user (*N*).).

The numerical simulation results for 4-QAM and 16-QAM modulation formats are shown in Fig. 5.3 – (a) and (b) according to Eq. (5.6)with the number of symbols for a single user (*N*) set as 400,000..

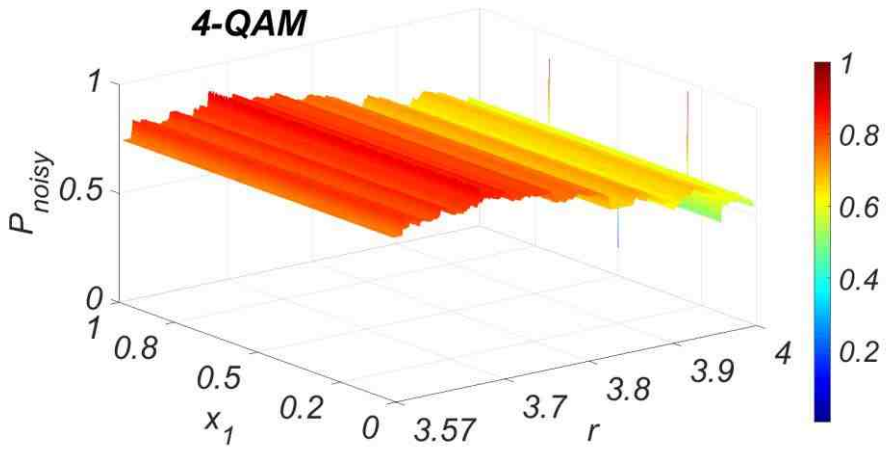

(a)

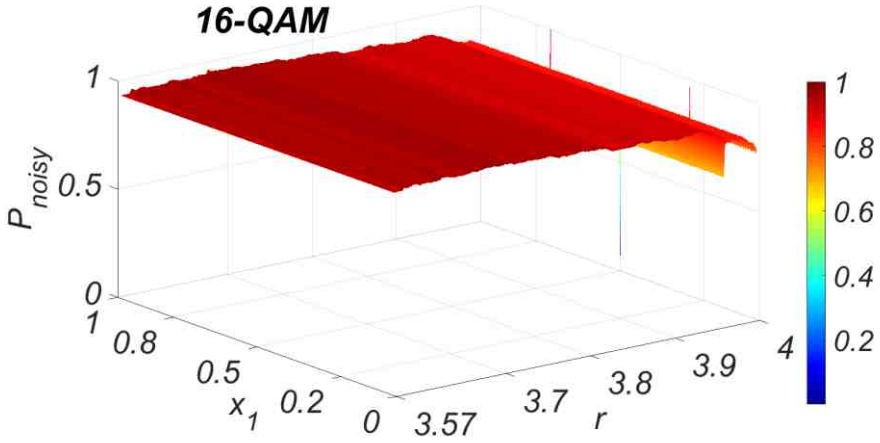

(b)

Fig. 5.3 Noise rate for (a) 4-QAM and (b) 16-QAM

It shows that the value of r dominates the noise rate while x_1 has negligible impact on the noise rate. The high noise rate which is larger than 0.5 is always guaranteed for both 4-QAM and 16-QAM modulation formats except three special sets. The first special set is constructed with the value of r equal to 4 and the initial element x_1 equal to 0.5, which gives out that the noise rate nearly reaches 0. This agrees with the nature of the logistic map described in Eq. (5.1)phase terms are plotted in Fig. 5.4all phase terms are generated as 0° the initial phase ($\theta[1]=360^\circ\times0.5=180^\circ$ and the second phase term ($\theta[2]=360^\circ\times\left(4\times0.5\times(1-0.5)\right)=360^\circ$), which indicates that almost all symbols are not affected by the generated phase.

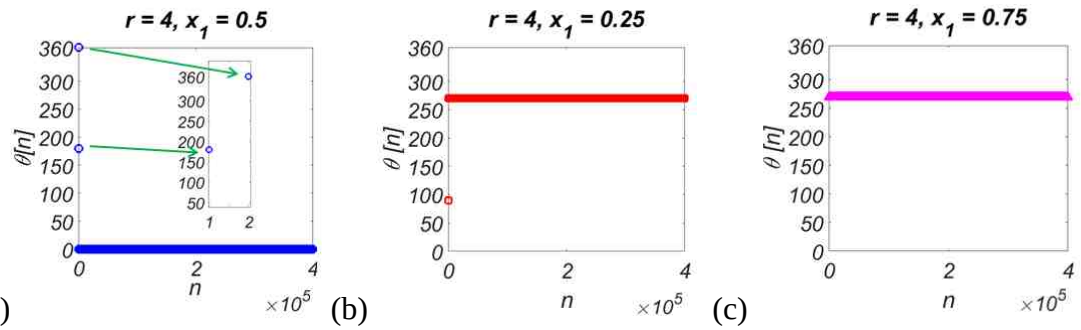

(a) (b) (c)

Fig. 5.4 Generated phase sequence with (a) r = 4 and x_1 = 0.5, (b) r = 4 and x_1 = 0.25, and (c) r = 4 and x_1 = 0.75

On the contrast, the other two special sets (r = 4, x_1 = 0.25 and r = 4, x_1 = 0.75, respectively) produces the noise rate that is closely equal to 1. However, the generated phase sequence loses chaotic behaviour as shown in Fig. 5.4 – (b) and (c), and thus should be avoided when selecting keys (r and x_1) for users. As a result, it is feasible to add phase noise by employing the chaotic phase generated by the logistic map. What is more, the noise rate for 16-QAM is higher than that for 4-QAM due to its higher complexity of the signal constellation.

At the receiver side, each user employs its dedicated key to generate the same phase sequence and decode the encrypted symbol data. Registered users within the coverage of OWC multiple access network are assigned with dedicated keys defined by their unique (r, x_1) pair. Chaffing and winnowing technique, which provides confidentiality via authentication, can be employed by Alice to transmit keys. By employing the chaffing and winnowing technique, eavesdropper has no ability to obtain other users' keys with a satisfactory Medium Access Control (MAC) algorithm [147]. Since the chaotic phase sequence generated by the logistic map is not periodic and is sensitive to the value of r and x_1 [148], blind equalisation at eavesdropper's side is also not effective in being able to extract the message, and hence the optical wireless connection from Alice to Bob can be secured against detection by Eve.

5.3 Experimental Demonstration

Fig. 5.5 illustrates the experimental setup employed for proof-of-concept demonstration. In the experiments, time-slot coded data with chaotic phase terms were generated off-line according to procedures described in Fig. 5.1. An AWG with 10 GHz sampling frequency and 0.5 V output peak-to-peak voltage (V_{pp}) was employed for D/A conversion. The output of AWG was amplified via an EA to modulate a 1553.01 nm tunable laser source through a 10 GHz MZM and a polarisation controller (PC) was also employed. After 5.6 km single-mode fibre signal distribution, the optical signal was sent over free-space. At the transmitter side, an adaptive lens system comprised of

a fibre termination coupled with a lens was employed to expand the optical beam to cover multiple users. The output power at the fibre end after MZM insertion loss and fibre transmission loss is about 7.5 dBm. The distance between the fibre end and the lens can be adjusted to control the beam width after beam expansion. In our experiments, the beam width was set to around 20 cm at the receiver plane. The selection of beam width was restricted by the optical transmission power as well as the availability of lenses. After 2 m of free space transmission, a coupling system including a compound parabolic concentrator (CPC) and a series of lenses was placed to collect and focus light into the fibre end. Then a 2 GHz bandwidth PD integrated with a FET based transimpedance preamplifier was used to convert the optical signal to electrical signal. A DSO performed A/D for off-line processing.

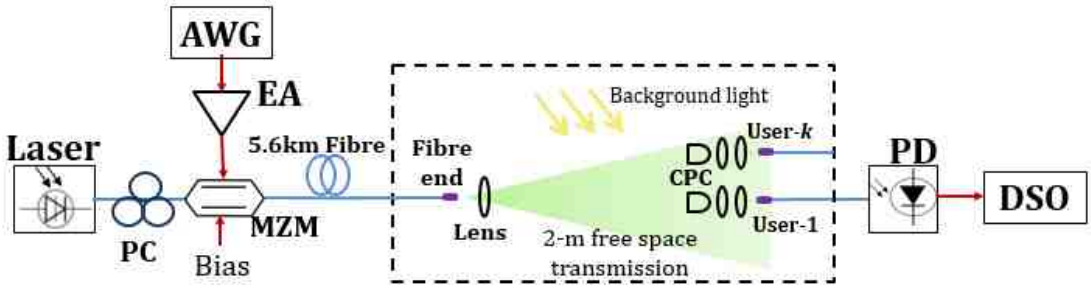

Fig. 5.5 Experimental setup

For the post-processing part, each user firstly identified the message tag to differentiate the beginning of the message sequence and down-converted the signal from the carrier frequency. Then a raised-cosine filter was employed for downsampling and filtering out the baseband signal. Then the summed symbol sequence was multiplied with the corresponding time-slot code for each user to retrieve its own chaotic phase coded symbol sequence. Each user then employed its security key consisting of the constant parameter r and the initial element x_1 to generate the chaotic phase sequence according to Eq. (5.1)–(5.2)s to the coded symbol sequence to securely decode the message. The traditional baseband demodulator and symbol error rate (SER) calculator were applied after amplitude and phase recovery.s to the coded symbol sequence to securely decode the message. The traditional baseband demodulator and symbol error rate (SER) calculator were applied after amplitude and phase recovery.

In terms of the proof-of-concept demonstration, the five-user scenario was considered. Four users were provided with the secure connection with chaotic phase, and the connection of the remaining user was unsecured as a reference. We selected four typical constant parameters of r for the four secure users, i.e. 3.95, 3.78, 3.61 and 3.67, which contribute to a higher noise rate successively according to the analytical results shown in Fig. 5.3 – (a) and (b). The initial value x_1 was fixed as 0.35 as it has ignorable impact on the noise rate according to results shown in Fig. 5.3 – (a) and (b) as well. The noise rate for these selected typical values of r with x_1 fixed 0.35 is re-plotted in for clearer illustration.

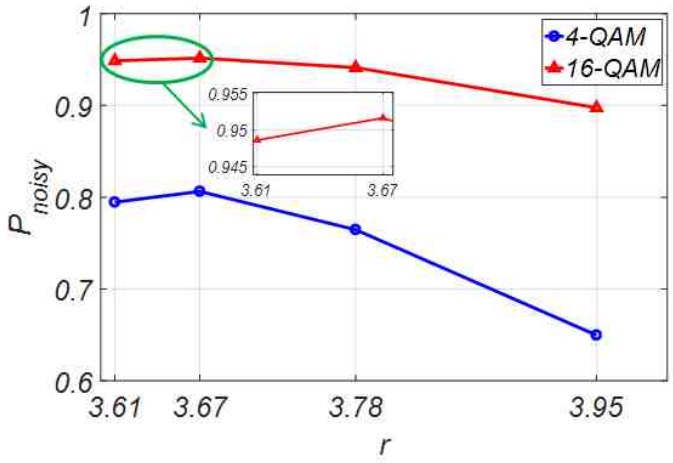

Fig. 5.6 Noise rate for r = 3.61, 3.67, 3.78 and 3.95 with x_1 fixed as 0.35

Measurements were first carried out to test the power penalty by comparing SER performances of the user without chaotic phase and the other four users with the chaotic phase. The secure capability of the proposed mechanism was then demonstrated by comparing SER performances with and without the knowledge of keys.

Multiple data rates for both 4-QAM and 16-QAM modulation formats were evaluated in our experiments, i.e. 1.25 Gb/s, 2 Gb/s and 2.5 Gb/s for 4-QAM, and 2.5 Gb/s, 3.33 Gb/s and 4 Gb/s for 16-QAM. The SER threshold is set according to 7% FEC limit (BER $\leq 3.8 \times 10^{-3}$) and the relationship between SER and BER is summarised in Table 2 according to [134] and [135] for some examples of general square QAM, e.g. 4-QAM, 16-QAM , 64-QAM and 256-QAM.

Modulation format	4-QAM (l = 1)	16-QAM (l = 2)	64-QAM (l = 3)	256-QAM (l = 4)
BER threshold	3.8×10^{-3}			
SER threshold	7.5859×10^{-3}	1.5142×10^{-2}	2.267×10^{-2}	3.0169×10^{-2}

Table 2 Relationship between BER threshold and SER threshold with 7% FEC limit for 4-QAM, 16-QAM, 64-QAM and 256-QAM

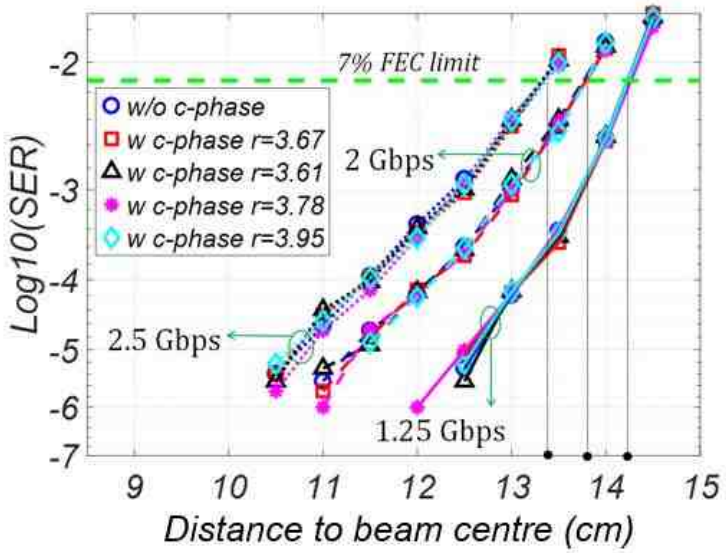

(a)

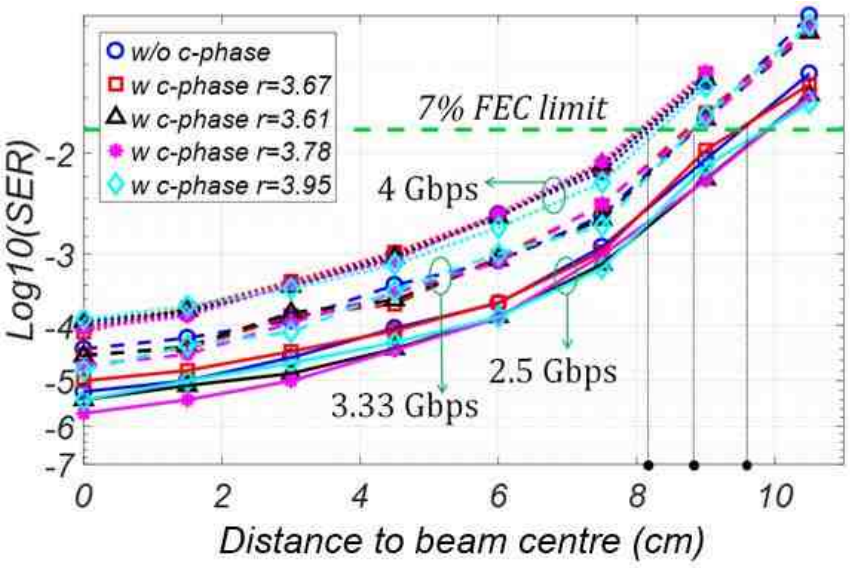

(b)

Fig. 5.7 Power penalty results with different bit rates for (a) 4-QAM and (b) 16-QAM

As illustrated in Fig. 5.7 – (a) and (b), there is no significant difference in the SER performance amongst users with different r and x_1 values for both 4-QAM and 16-QAM modulation formats. In addition, the users with and without the proposed chaotic phase for a specific system capacity also have similar performance. The reason is that the chaotic phase can be cancelled at the user terminal by applying the corresponding key (r and x_1) as stated in the principle. However, system with higher capacity provides smaller coverage since it suffers more from bandwidth related noise during transmission and detection while the chaotic phase noise is fully cancelled. Also, no superiority exists among users according to the rules of the TSC scheme.

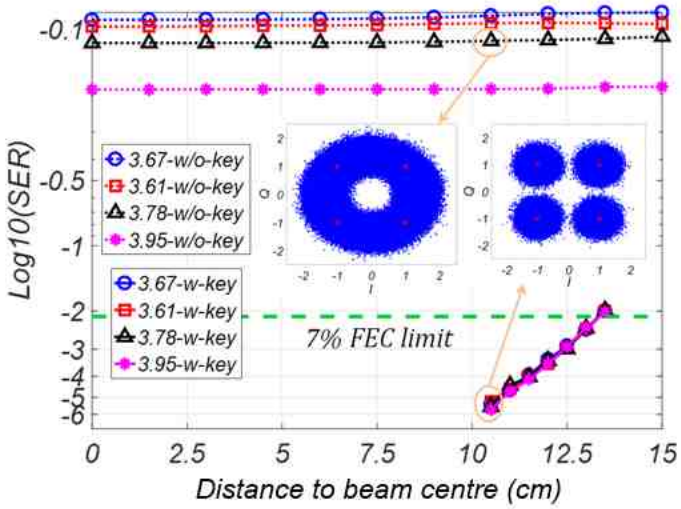

(a)

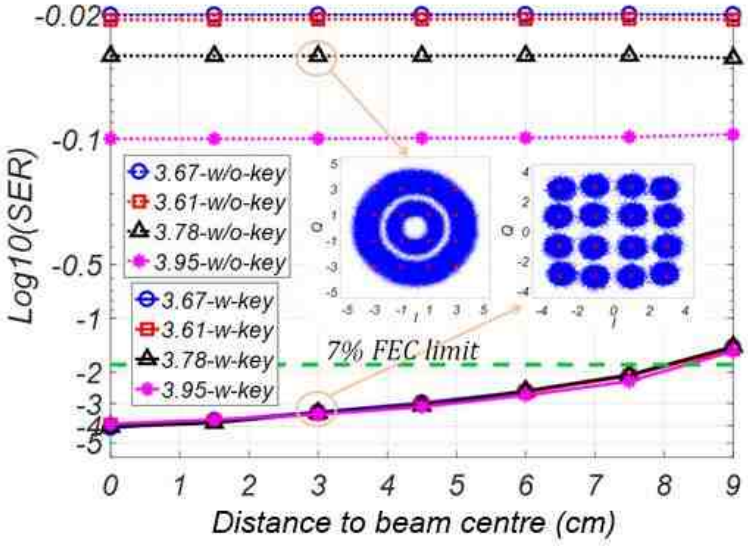

(b)

Fig. 5.8 SER performance and constellation with and without the key for (a) 2.5 Gb/s 4-QAM and (b) 4 Gb/s 16-QAM

In addition, we tested the SER performance without the knowledge of keys. The results of 2.5 Gb/s 4-QAM and 4 Gb/s 16-QAM scenarios are shown in Fig. 5.8 – (a) and (b). We can see from the figure that the SER without the knowledge of each key is always above the error-free threshold at any location, which means the transmitted data cannot be recovered and secure communication can be achieved. In addition, the key that contributes to higher noise rate shown in Fig. 5.6 (i.e. 3.95, 3.78, 3.61, and 3.67, which contribute to a higher noise rate successively) leads to higher SER without the knowledge of the corresponding key. For different locations, SER without knowledge of each key is almost flat as it is dominated by the phase noise added by the chaotic sequence rather than signal SNR.

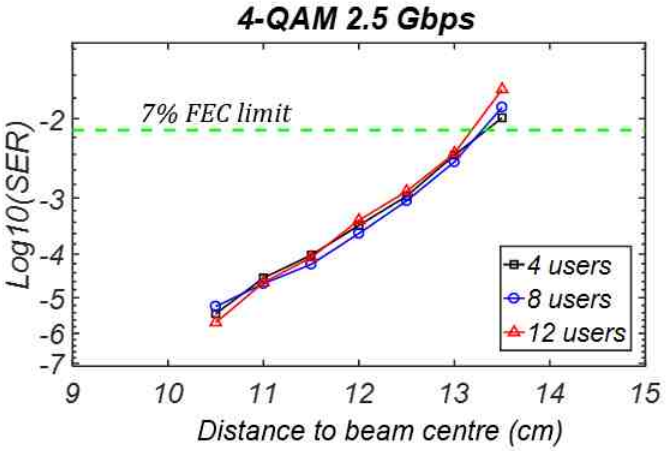

(a)

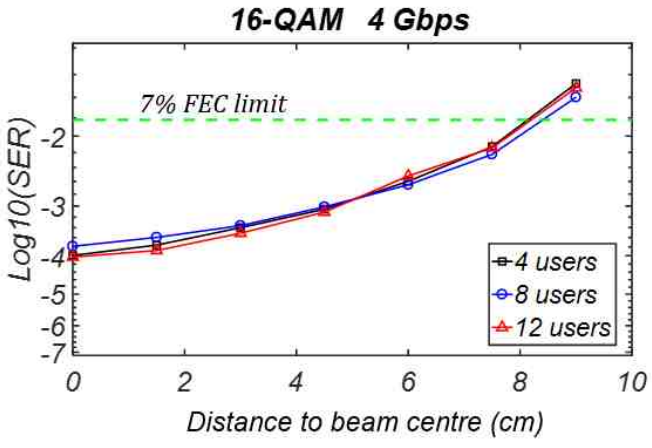

(b)

Fig. 5.9 Average BER of all users for 4-user, 8-user and 10 user cases with (a) 2.5 Gb/s 4-QAM and (b) 4 Gb/s 16-QAM

We also considered 8 users and 10 users registered to be served with secure connections in the system to evaluate the impact of the number of users on the system performance. For 8-user case, 3.61, 3.67, 3.72, 3.78, 3.81, 3.87, 3.95 and 3.97 are assigned to each user, respectively, for the value of r while x_1 is set as 0.35 for all users. In terms of 10-user case, the other two values of r are selected as 3.59 and 3.65. Fig. 5.9 shows the average SER of all legal users for each case based on 4-QAM with 2.5 Gb/s and 16-QAM with 4 Gb/s. It can be observed that the SER for each case with different amount of users does not differ much. As a result, the system performance with chaotic phase for legal user does not degrade with the increasing number of users in the secured system.

5.4 Investigation on System Robustness

5.4.1 Analysis of secured mechanism limitation

In order to provide secure multiple access in indoor OWC system, we have proposed a novel mechanism using time-slot coding for multiple access and chaotic phase for secure capability. Experimental results show that the intended user's signal quality is not affected by the addition of chaotic phase while the potential eavesdropper cannot obtain the message without the key. However, this mechanism provides security by the key consisting of two constants r and x_1 which have finite range and all users registered in OWC network know the security mechanism. Potential eavesdropper is thus able to theoretically conduct exhaustive searching for a set of r and x_1 that provides the lowest SER to intercept legal user's information.

It is thus significant to critically investigate resilience of the scheme against such an exhaustive search, where a higher searching accuracy tolerated by the mechanism represents a better robustness. Consequently, we first numerically evaluate the sensitivity of key. The legitimate user (Bob) has the key of r^b and $x_1{}^b$ while the potential

eavesdropper (Eve) prepares to eavesdrop the message using its own estimates for r^e and x_1^e at the decoding side:

$$r^e = r^b + \delta, \quad x_1^e = x_1^b + \delta \tag{5.7}$$

where δ is the difference between Bob's and Eve's keys and also stands for the searching accuracy. The chaotic phase sequence generated by Bob and Eve are denoted by $\theta^b[n]$ and $\theta^e[n]$ using Eq. (5.1)OBJ(5.2)s own estimates of the key to generate chaotic phase sequence and apply its negative version to the received signal at the receiver side. The outage rate denoted as P_{out} is defined as the percentage of symbols that can be decoded correctly with Eve's key:$_{out}$ is defined as the percentage of symbols that can be decoded correctly with Eve's key:

$$\mathrm{P}_{out} = \frac{1}{4^{l-1}} \sum_{I,Q} P\left(-\gamma(I,Q) \le \theta^b[n] - \theta^e[n] \le \beta(I,Q)\right) \tag{5.8}$$

where $\left(\theta^b[n] - \theta^e[n]\right)$ is the resultant phase around the symbol after applying Eve's decoding phase sequence and the condition that makes correct decoding is when the resultant phase is within the range between $-\gamma$ and β, which are defined in Eq. (5.3) The numerical simulation results of the outage rate with $\delta = 10^{-5}$ and $\delta = 10^{-10}$ for both 4-QAM and 16-QAM modulation formats are illustrated in OBJFig. 5.10.

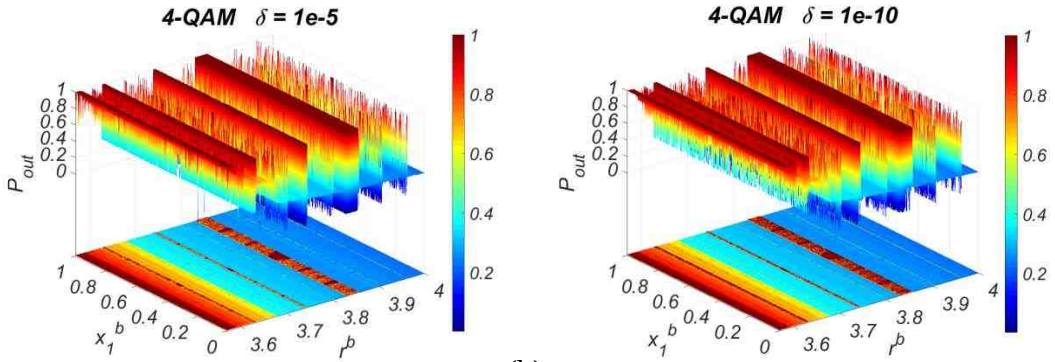

(a) (b)

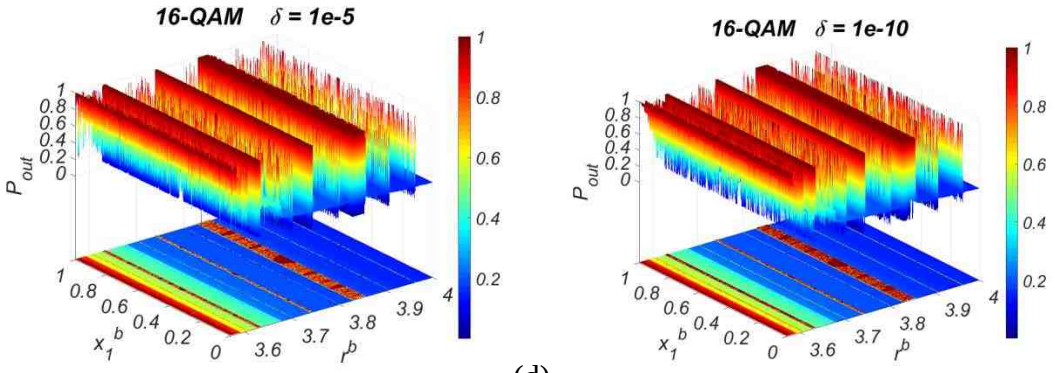

(c) (d)

Fig. 5.10 Outage rate with (a) δ = 1e-5 for 4-QAM. (b) $\delta = 10^{-10}$ for 4-QAM, (c) δ = 1e-5 for 16-QAM, and (d) $\delta = 10^{-10}$ for 16-QAM

It can be seen that the constant parameter in Bob's key (r^b) dominates the outage rate while the initial value (x_1^b) has limited impact. Furthermore, the simulation results show similar distribution of Pout over r^b and x_1^b with two different δ values, i.e. 10^{-5} and 10^{-10}, for both modulation formats. With the tiny difference (10^{-10}) which indicates high searching accuracy between keys, the outage rate maintains lower than 0.5 for r^b landing outside the islands of stability of logistic map. Since the principle of the logistic map is a bifurcation process, for the constant parameter r larger than 3.57, chaos emerges with some isolated ranges that show non-chaotic manner which are named as islands of stability [146, 149]. The examples of islands of stability are indicated in the bifurcation diagram of the logistic map shown in Fig. 5.11.

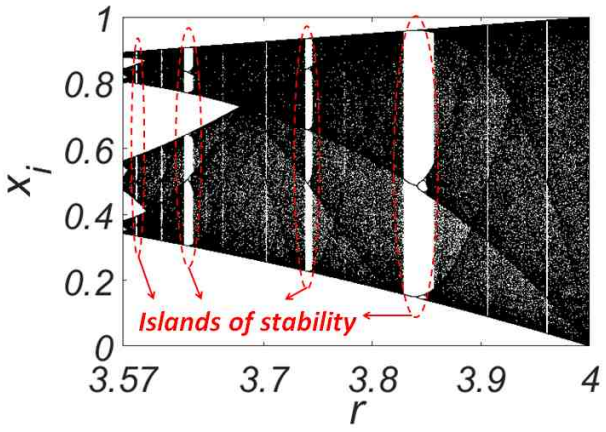

Fig. 5.11 Bifurcation diagram of the logistic map and islands of stability

We further evaluate the outage rate with different orders of δ for four typical values of r while x_1 is fixed as 0.35 for Bob. Three values of r are selected as 3.59, 3.65 and 3.78, which are outside the island of stability and are successively further away from it. The fourth value is 3.84 which stands inside the island of stability and thus does not lead to the chaotic behaviour, showing higher outage rate of 1 for most cases. The outage rate with low searching accuracy (δ = 0.001) to high searching accuracy (δ = 10^{-10}) for 4 typical values of r is plotted in Fig. 5.12. It is import to note that realising the searching accuracy higher than 10^{-10} is restricted by numerical precision of the processor.

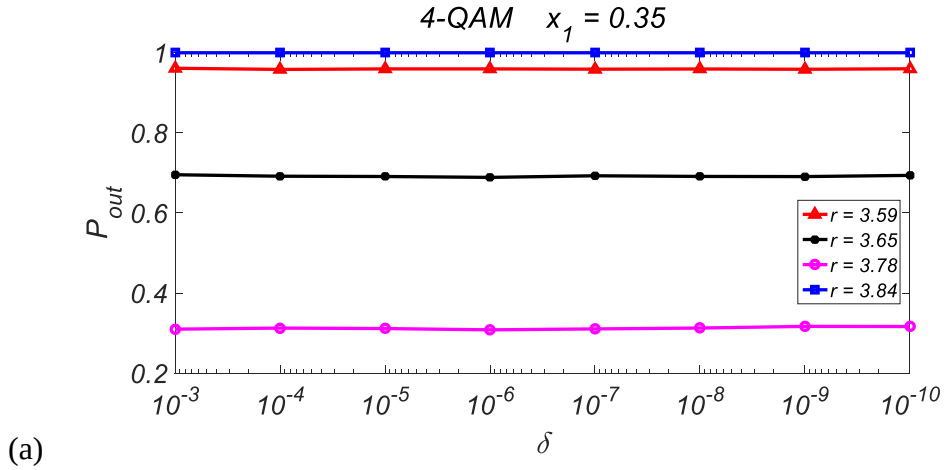

(a)

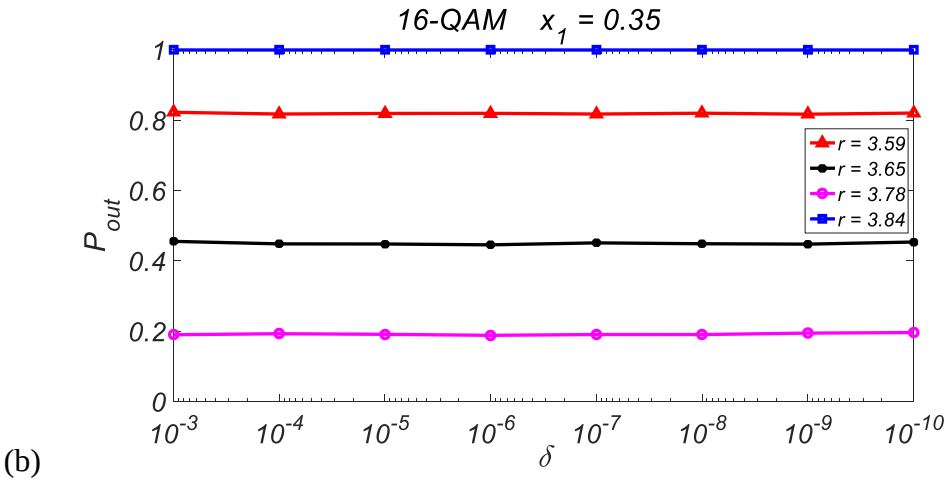

(b)

Fig. 5.12 Outage rate with different orders of searching accuracy (δ) for r = 3.59, 3.65, 3.78 and 3.84 while x_1=0.5 based on (a) 4-QAM modulation format and (b) 16-QAM modulation format

It can be seen that 4-QAM modulation format produces higher outage rate compared with 16-QAM due to its simple signal constellation for a specific value of r outside the islands of stability. The outage rate remains stable with searching accuracy higher than

10^{-3}. As a result, it is generally concluded that the outage rate can be well limited with the searching accuracy of potential eavesdropper up to $(10^{-10})^2$ by carefully selecting the constant parameter for each user according to outage rate calculated in Eq. (5.8).

In order to investigate the impact of searching accuracy on the OWC system performance, we further derive SER equation with searching accuracy over indoor OWC channel and conduct experimental demonstration using setup shown in Fig. 5.5. We here define the outage phase sequence as the difference between two phase sequences generated using Bob's and Eve's keys:

$$\theta_{out}[n] = \left|\theta^b[n] - \theta^e[n]\right| \tag{5.9}$$

By following the same convention employed in deriving SER in Section 4.4.1, the SER equation with searching accuracy and indoor OWC channel can be derived as:

$$\begin{aligned} &SER\left(l,\sigma,x_1^{\,b},r^b,\delta,N\right) \\ &= \frac{1}{N}\sum_{i=1}^{N}\left\{1-\frac{1}{4^{l-1}}\left[\begin{array}{l} \sum_{I_1,Q_1}\left(\begin{array}{l}\left(F\left(Q_1+1-y_{N,1,1},\sigma\right)-F\left(Q_1-1-y_{N,1,1},\sigma\right)\right)\cdot \\ \left(F\left(I_1+1-x_{N,1,1},\sigma\right)-F\left(I_1-1-x_{N,1,1},\sigma\right)\right)\end{array}\right) \\ +2\sum_{I_2,Q_1}\left(\begin{array}{l}\left(F\left(Q_1+1-y_{N,2,1},\sigma\right)-F\left(Q_1-1-y_{N,2,1},\sigma\right)\right)\cdot \\ F\left(-\left(I_2-1-x_{N,2,1}\right),\sigma\right)\end{array}\right) \\ +\sum_{I_2,Q_2}\left(F\left(-\left(Q_2-1-y_{N,2,2}\right),\sigma\right)\cdot F\left(-\left(I_2-1-x_{N,2,2}\right),\sigma\right)\right) \end{array}\right]\right\} \end{aligned} \tag{5.10}$$

$$F\left(\omega,\sigma\right) = \int_{-\infty}^{\omega}\frac{1}{\sigma\sqrt{2\pi}}\exp\left(-\frac{x^2}{2\sigma^2}\right)dx$$

where $x_{N,c,d}$ and $y_{N,c,d}$ is expressed as:

$$\begin{aligned} x_{N,c,d} &= \sqrt{I_c^{\,2}+Q_d^{\,2}}\cdot\cos\left(\angle\left(I_c,Q_d\right)+\theta_{out}[i]\right) \\ y_{N,c,d} &= \sqrt{I_c^{\,2}+Q_d^{\,2}}\cdot\sin\left(\angle\left(I_c,Q_d\right)+\theta_{out}[i]\right) \\ c,d &= 1,2 \end{aligned} \tag{5.11}$$

In Eq. (5.11)the notation of $\angle\left(I_c,Q_d\right)\left(I_c,Q_d\right)$positive in-phase axis where I_c Q_d ^{2l} – ary QAM can be given by: QAM can be given by:

$$
\begin{aligned}
I_1 &= 2a-1-2^l, \quad 2^{l-1} < a < 2^l \\
Q_1 &= 2b-1-2^l, \quad 2^{l-1} < b < 2^l \\
I_2 &= 2^l - 1 \\
Q_2 &= 2^l - 1
\end{aligned}
\tag{5.12}
$$

where *a* and *b* are natural numbers. Standard deviation in Eq. (5.10)OBJ(3.25)Derivation of the relationship between SER and BER is under a valid approximate relationship between EVM_{RMS} and SNR as shown in Eq. OBJ, which is only valid for the typical system with transmission and detection noise. However, when characterizing eavesdropper's performance, the noise level containing chaotic phase noise which is too high to hold this approximation. (3.17), which is only valid for the typical system with transmission and detection noise. However, when characterizing eavesdropper's performance, the noise level containing chaotic phase noise which is too high to hold this approximation. Hence, only SER is considered when evaluating Eve's performance.

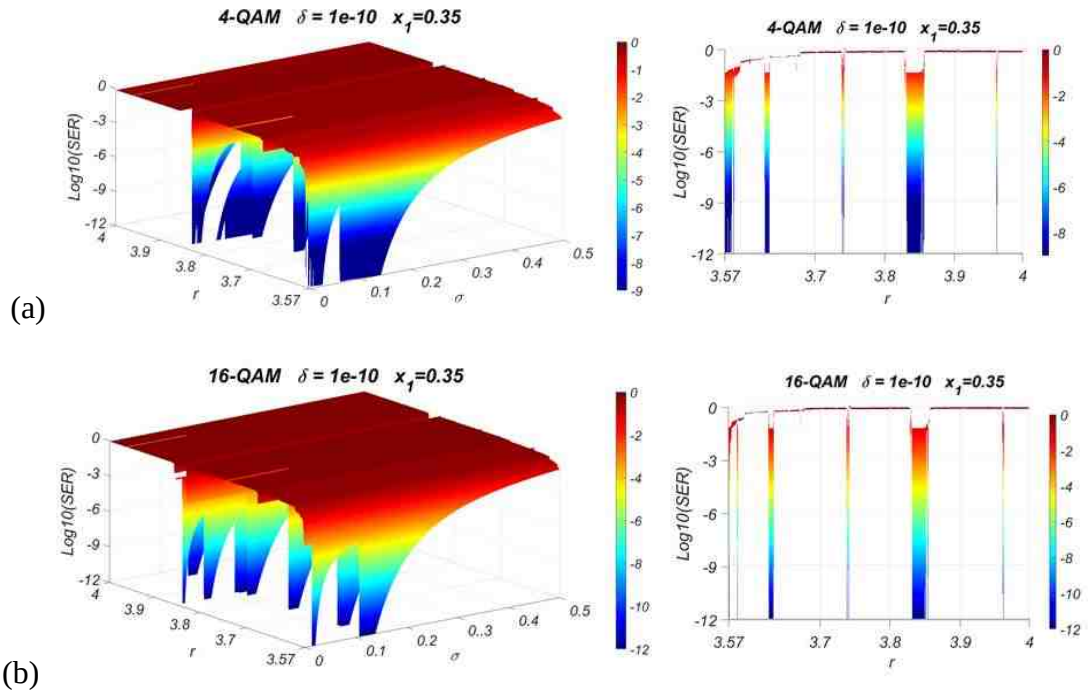

(a)

(b)

Fig. 5.13 Analytical SER in terms of σ and r with $x_1 = 0.35$ and $\delta = 10^{-10}$ for (a) 4-QAM and (b) 16-QAM

The analytical results of SER with a higher searching accuracy of 10^{-10} respect to r and σ based on 4-QAM and 16-QAM modulation formats are illustrated in Fig. 5.13 where

x_1 is fixed as 0.35. An examination of the variation as r takes different values clearly shows agreement with the islands of stability illustrated in Fig. 5.11. The SER performance with r having values outside the islands of stability maintains in a high level and the signal SNR which is represented by standard deviation (σ) has little impact on it. However, the SER performance with r inside the islands of stability is dependent on σ and is increasing with increased σ, which means the potential eavesdropper is able to extract legal user's message with satisfactory signal SNR. In real implementations, the values of r inside islands of stability should be avoided.

To further evaluate the impact of x_1 on SER performance of Eve, we also include the analytical SER in terms of the initial element x_1 and standard deviation (indicating signal SNR level) for 4-QAM and 16-QAM with three typical values of r selected outside the islands of stability, i.e. 3.59, 3.65 and 3.78 in Fig. 5.14. It can be seen that the initial element x_1 has negligible impact on Eve's SER, although the impact of x_1 becomes more obvious for r = 3.98, 3.65 and 3.59 successively. What is more, the SER performance of r that provides smaller outage rate ($P_{out,r=3.78} < P_{out,r=3.65} < P_{out,r=3.59}$) is less dependent on σ which indicates signal SNR.

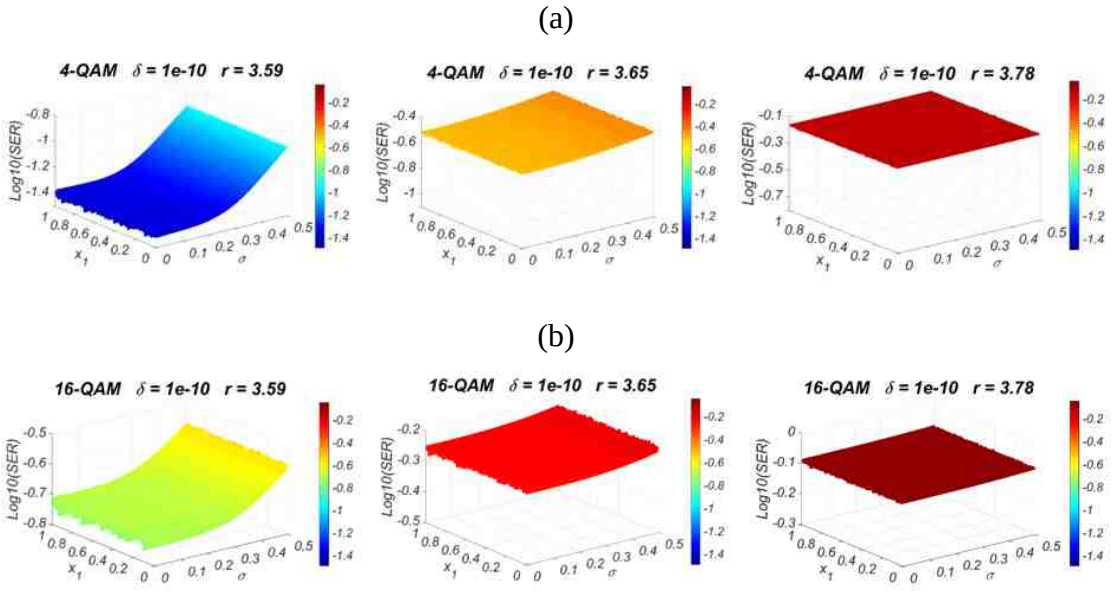

Fig. 5.14 Analytical SER in terms of σ and x_1 with three typical values of r and $\delta = 10^{-10}$ for (a) 4-QAM and (b) 16-QAM

In addition to analytical investigation, we experimentally evaluated the robustness of the mechanism against the high searching accuracy and showed satisfactory agreement between measured results and analytical results. In our experiments, some typical values of r were selected while x_1 was fixed as 0.35 for Bob, since the chaotic behaviour is dependent on r rather than x_1 as shown in the analysis before. Four users were considered for proof-of-concept demonstration and the typical value of r was selected as 3.59, 3.65, 3.78 and 3.84 for each user, respectively. A tiny difference between keys of Bob and Eve was considered, i.e. $\delta = 10^{-10}$, which indicates a high searching accuracy. The experimental setup is as in Fig. 5.5 with a beam waist of 20 cm. The SER performances for Bob and Eve based on 4-QAM modulation format with multiple data rates in terms of the distance from beam centre are plotted in Fig. 5.15 while several received constellations are illustrated in Fig. 5.16. The results using 16-QAM modulated data are shown in Fig. 5.17 and Fig. 5.18.

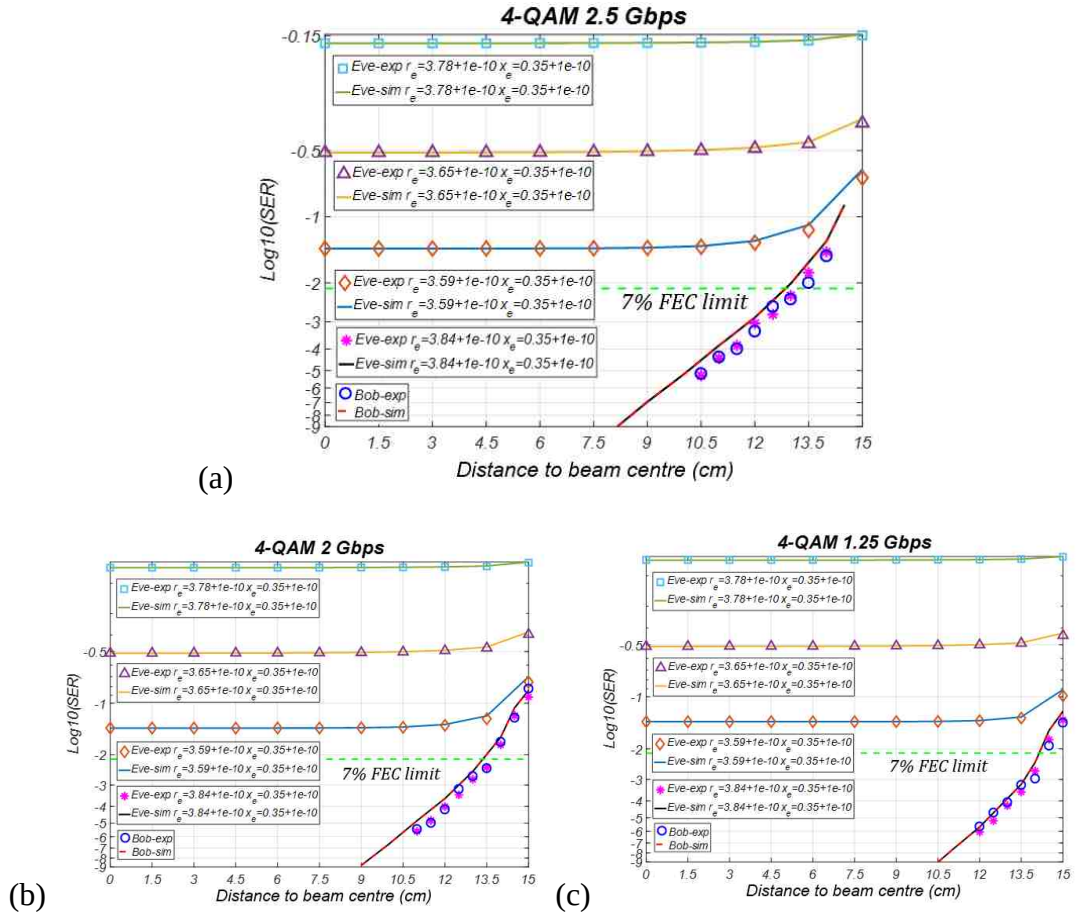

Fig. 5.15 SER performance with respect to different distances from beam centre for 4-QAM with (a) 2.5 Gb/s, (b) 2 Gb/s and (c) 1.25 Gb/s

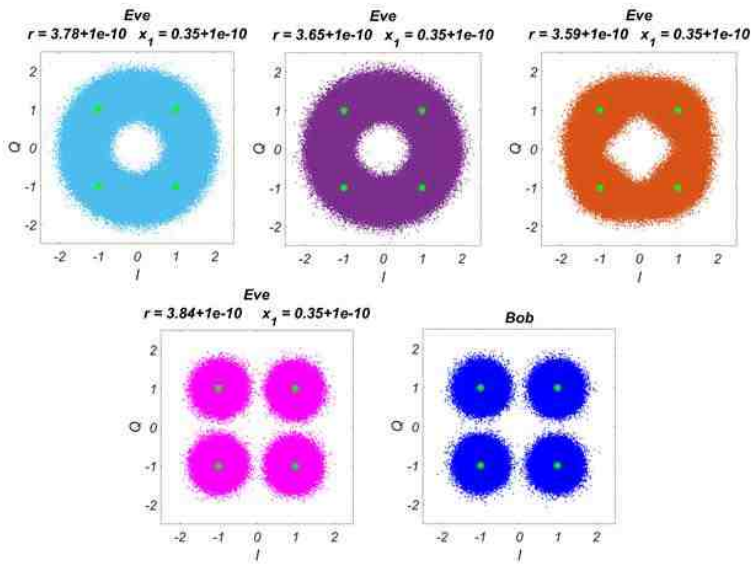

Fig. 5.16 Experimentally received signal constellations at 10.5 cm from the beam centre for 4-QAM with 2.5 Gb/s

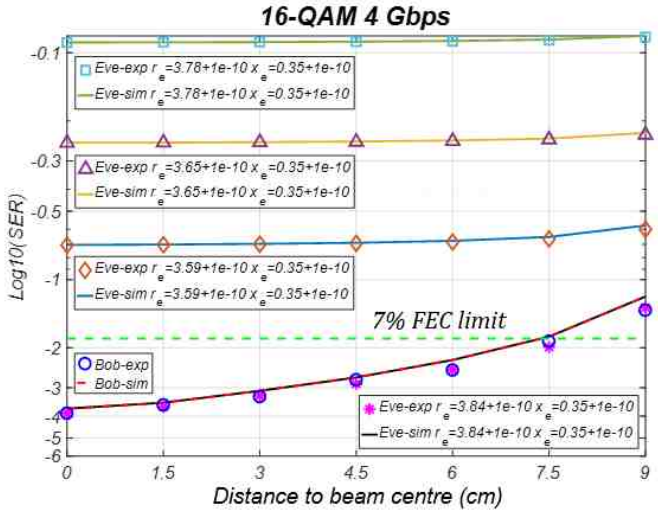

(a)

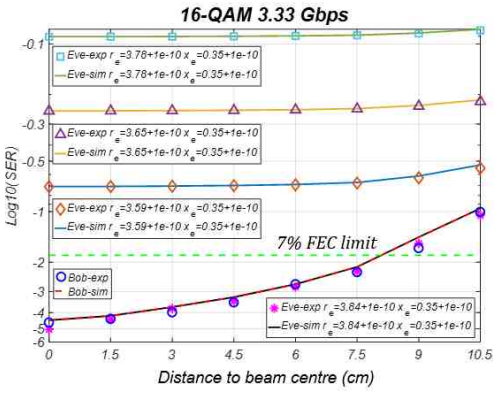

(b)

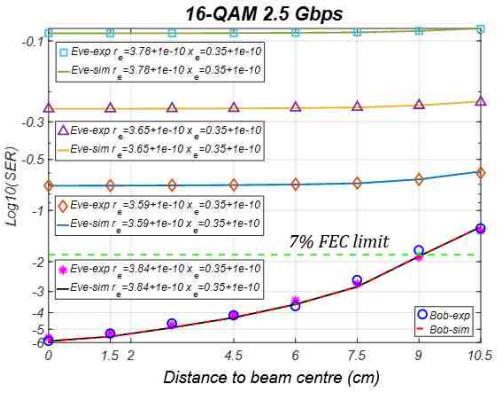

(c)

Fig. 5.17 SER performance with respect to different distances from beam centre for 16-QAM with (a) 4 Gb/s, (b) 3.33 Gb/s and (c) 2.5 Gb/s

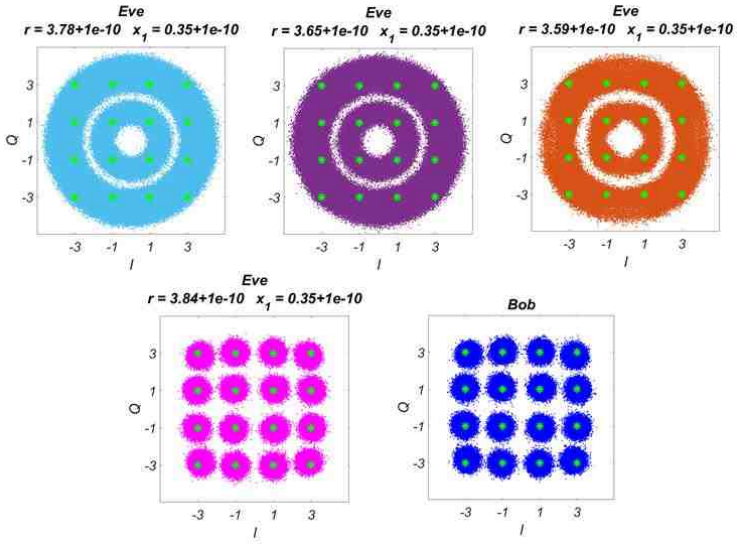

Fig. 5.18 Experimentally received signal constellations at beam centre for 16-QAM with 4 Gb/s

In Fig. 5.15 and Fig. 5.17, the analytical SER results are denoted by lines and are calculated according to Eq. (3.25)(5.10)Since there is no significant difference in SER amongst legal users with different keys as shown in Fig. Fig. 5.7Fig. Fig. 5.16Fig. Fig. 5.18 cm from the beam centre for 2.5 Gb/s 4-QAM and 0 cm for 4 Gb/s 16-QAM. Also, the other possible source for the offset is from approximations when calculating theoretical stand deviation. 0 cm for 4 Gb/s 16-QAM. Also, the other possible source for the offset is from approximations when calculating theoretical stand deviation.

Importantly, for keys with chaotic manner (r = 3.59, 3.65 and 3.78), the eavesdropper with high searching accuracy of 10^{-10} still has SER values above the 7% FEC limit, which indicates that the message remains secure. In addition, the key which provides lower outage rate as shown in Fig. 5.10 and Fig. 5.12 provides worse SER for Eve even with accurate searching. On the other hand, the eavesdropper successfully decodes the message of Bob equipped with r of 3.84. That is because that the bifurcation process using r = 3.84 produces periodic values and thus loses chaotic behaviour. As a result, the values of r that belong to islands of stability cannot claim any security due to the absence of chaos.

Instead of the analysis discussed above, based on the literatures [150, 151], a common method to demonstrate random characteristic of the generated sequence is the study of

auto-correlation and cross-correlation function. We alternatively study the auto-correlation and cross-correlation functions in the numerical simulations to evaluate the randomness of the generated chaotic sequence. The zero-normalised auto-correlation (*ZNAC*) and zero-normalised cross-correlation (*ZNCC*) for the generated phase sequence $\theta[n]$ and $\theta^*[n]$ are defined as follows:

$$\theta'[n] = \theta[n] - \overline{\theta[n]},$$
$$\Theta[n] = \frac{\theta'[n]}{\|\theta'[n]\|}, \tag{5.13}$$

$$ZNAC = \frac{1}{N}\sum_{n=1}^{N}\Theta(i)\Theta(i+\tau), \quad -(N-1) \le \tau \le N-1$$

$$ZNCC = \frac{1}{N}\sum_{n=1}^{N}\Theta(i)\Theta^*(i+\tau), \quad -(N-1) \le \tau \le N-1 \tag{5.14}$$

where the zero-normalised phase sequence is denoted as $\Theta[n]$, $\overline{\theta[n]}$ is the mean value of the original phase sequence $\theta[n]$, $\|.\|$ is the L^2 norm and τ is the displacement. The chaotic phase sequence is generated using r = 4 and x_1 = 0.6 for example to calculate autocorrelation and the corresponding result is illustrated in Fig. 5.19 – (a). The number of phase terms in each sequence is set as 400,000.

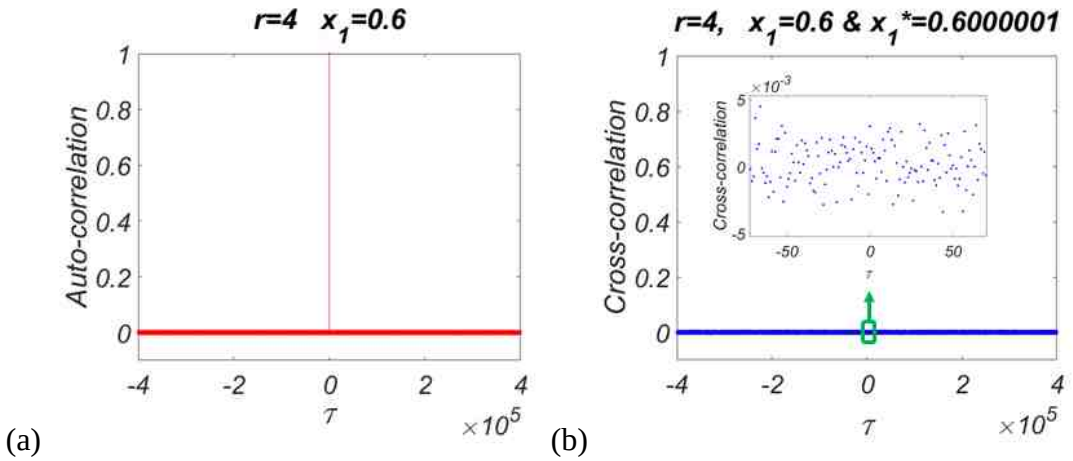

(a) (b)

Fig. 5.19 Examples of (a) autocorrelation for r = 4, x_1 = 0.6 and (b) cross-correlation for r = 4, x_1 = 0.6 and r = 4, x_1 = 0.6000001

It can be observed that the value of *ZNAC* maintains very low around 0 when τ is not equal to 0, which indicates that this sequence does not have self-similarity. Fig. 5.19 – (b) represents the result of *ZNCC* of two phase sequences generated using $r = 4$ and two initial elements with tiny difference, i.e. $x_1 = 0.6$ and $x_1^* = 0.6000001$, respectively. The value of *ZNCC* is shown to be very small around zero for all values of lag τ, which means the generated sequences have well satisfactory random property. In Fig. 5.20, we further illustrate the *ZNCC* results of Bob's phase sequences and Eve's phase sequence employed in our experiments as shown in Fig. 5.15 and Fig. 5.17, i.e. r^b = 3.59, 3.65, 3.78 and 3.84, respectively, while x_1^b =0.35.

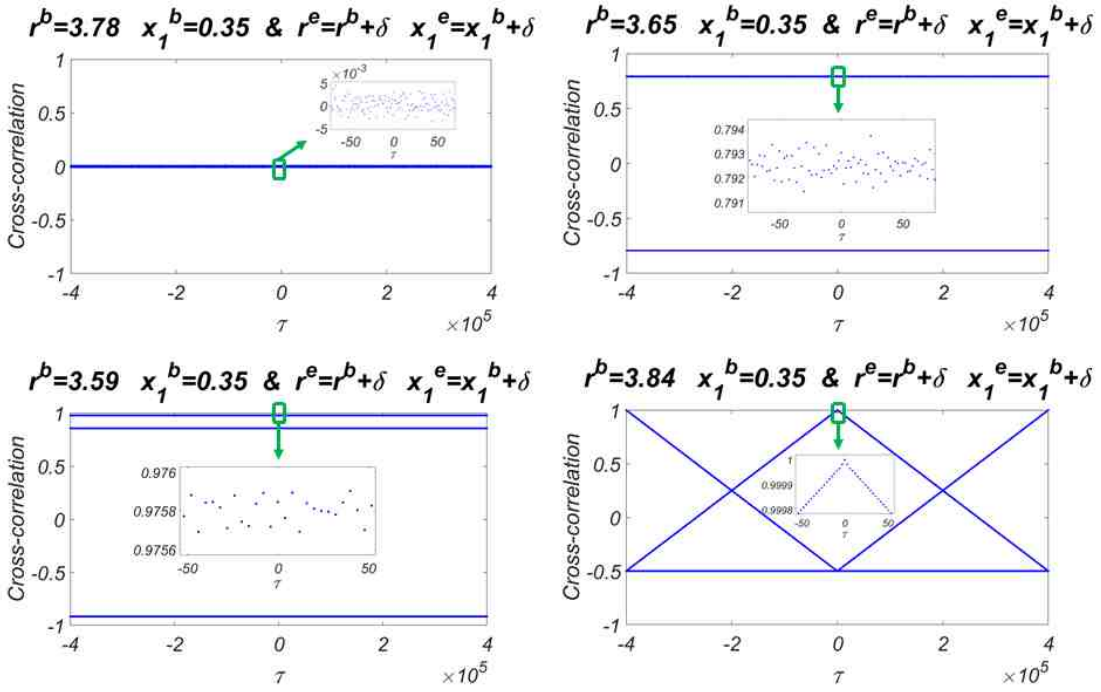

Fig. 5.20 Cross-correlation of the phase sequences for Bob and Eve with $\delta = 10^{-10}$ and r^b = 3.59, 3.65, 3.78 and 3.84, respectively.

From Fig. 5.15, Fig. 5.17 and Fig. 5.20, it can be concluded that the key, which provides the *ZNCC* values closer to 0, is able to lead the eavesdropper to have worse SER. Only Bob's sequence generated using r^b = 3.84 has the *ZNCC* that exactly equals to 1 with Eve's phase sequence when $\tau = 0$. However, the analysis of auto-correlation and cross-correlation is not intuitive to indicate the system performance. Even two sequences of chaotic phase of Bob and Eve look very similar with some values of *ZNCC* around

0.976 when r^b is equal to 3.59 and δ is 10^{-10}, the message of the legitimate user is still secure from eavesdropping as shown in the previous comprehensive investigation with both analytical results and experimental results on SER. The outage rate calculated using Eq. (5.8)–(5.10) guide to select keys for registered users. Although the equations in the analysis above are derived for indoor OWC channel based on QAM modulation format with chaotic phase generated using the logistic map, the derivation process can be transferred to other communication systems using different modulation formats and different methods to generate chaotic sequence, such as Lorenz map [157], Chebyshev chaotic map [158], etc. [158], etc.

5.4.2 Code overlapping ratio impact with chaotic phase

In addition to investigation on searching accuracy, tolerance to the time-slot code misalignment incorporating chaotic phase is another key factor that affects system robustness and also needs to be analysed as it affects multi-user interferences substantially. We derive theoretical BER equation and also conduct experimental demonstration for the case where chaotic phase is incorporated. By following the convention described in Section 4.4.1, the symbol error rate for the intended secured user with the overlapping ratio (R_o) is given by:

$$\begin{aligned} &SER\left(l,\sigma,R_o,\theta_b,\theta_o,N\right) \\ &=\frac{1}{N}\sum_{i=1}^{N}\left\{1-\frac{4}{\left(2^{2l}\right)^2}\left[\begin{array}{l}\displaystyle\sum_{c=1,d=1}\sum_{I_2,Q_2}\int_{Q_{1,d}-1-y_{N,d}}^{Q_{1,d}+1-y_{N,d}}\int_{I_{1,c}-1-x_{N,c}}^{I_{1,c}+1-x_{N,c}} f\left(x,y\right)dxdy \\ \displaystyle+2\sum_{c=1,d=2}\sum_{I_2,Q_2}\int_{Q_{1,d}-1-y_{N,d}}^{\infty}\int_{I_{1,c}-1-x_{N,c}}^{I_{1,c}+1-x_{N,c}} f\left(x,y\right)dxdy \\ \displaystyle+\sum_{c=2,d=2}\sum_{I_2,Q_2}\int_{Q_{1,d}-1-y_{N,d}}^{\infty}\int_{I_{1,c}-1-x_{N,c}}^{\infty} f\left(x,y\right)dxdy\end{array}\right]\right\} \end{aligned} \tag{5.15}$$

where $x_{N,c}$ and $y_{N,d}$ are derived as:

$$\begin{aligned} x_{N,c} &= I_{1,c}+R_o\sqrt{I_2{}^2+Q_2{}^2}\cos\left(\angle\left(I_2,Q_2\right)+\theta_o\left[i\right]-\theta_b\left[i\right]\right) \\ y_{N,d} &= Q_{1,d}+R_o\sqrt{I_2{}^2+Q_2{}^2}\sin\left(\angle\left(I_2,Q_2\right)+\theta_o\left[i\right]-\theta_b\left[i\right]\right) \\ &c,d=1,2 \end{aligned} \tag{5.16}$$

where $\theta_o[i]$ is the i^{th} element of the summation of chaotic phases from overlapped adjacent users and $\theta_b[i]$ is the i^{th} phase component of the intended user:

$$\begin{aligned} x_{i+1}^{j-1} &= r^{j-1} x_i^{j-1}\left(1-x_i^{j-1}\right), \quad \theta^{j-1}[n] = 360 \cdot x^{j-1}[n] \\ x_{i+1}^{j+1} &= r^{j+1} x_i^{j+1}\left(1-x_i^{j+1}\right), \quad \theta^{j+1}[n] = 360 \cdot x^{j+1}[n] \\ \theta_o[i] &= \theta^{j-1}[i] + \theta^{j+1}[i] \end{aligned} \tag{5.17}$$

$$\begin{aligned} x_{i+1}^{j} &= r^{j} x_i^{j}\left(1-x_i^{j}\right) \\ \theta_b[n] &= 360 \cdot x^{j}[n] \end{aligned} \tag{5.18}$$

The intended user is generalised as the j^{th} user and the key assigned to the preceding user, i.e. $(j-1)^{th}$ user, consists of the constant parameter r^{j-1} and the initial element x_1^{j-1} while the following user is denoted as the $(j+1)^{th}$ user. The other symbols as shown in Eq. (5.15)–(5.16) as follows: as follows:

$$\begin{aligned} I_{1,1} &= 2a - 1 - 2^l, \quad 2^{l-1} < a < 2^l \\ Q_{1,1} &= 2b - 1 - 2^l, \quad 2^{l-1} < b < 2^l \\ I_{1,2} &= 2^l - 1 \\ Q_{1,2} &= 2^l - 1 \\ I_2 &= 2p - 1 - 2^l, \quad 1 \le p \le 2^l \\ Q_2 &= 2q - 1 - 2^l, \quad 1 \le q \le 2^l \end{aligned} \tag{5.19}$$

where a, b, p and q are natural numbers. As discussed in Section 3.3.3 and Section 4.4.1, we further derive EVM_{RMS} in the proposed system with chaotic phase and code misalignment issue to link SER with BER. According to the definition of EVM_{RMS} shown in Eq. (3.12), EVM_{RMS} for this case can be expressed as:

$$
\begin{aligned}
EVM_{RMS} &= \sqrt{\frac{E\left[\begin{array}{l}\left|R_o \cdot \sqrt{I_{0,n}^{'\,2}+Q_{0,n}^{'\,2}} \cdot \cos\left(\angle\left(I_{0,n}^{'\,2}+Q_{0,n}^{'\,2}\right)+\theta_o[i]-\theta_b[i]\right)+N_I\right|^2 \\ +\left|R_o \cdot \sqrt{I_{0,n}^{'\,2}+Q_{0,n}^{'\,2}} \cdot \sin\left(\angle\left(I_{0,n}^{'\,2}+Q_{0,n}^{'\,2}\right)+\theta_o[i]-\theta_b[i]\right)+N_Q\right|^2\end{array}\right]}{P_{avg}}} \\
&= \sqrt{\frac{\begin{array}{l}E\left[R_o^{\,2}\cdot\left(I_{0,n}^{'\,2}+Q_{0,n}^{'\,2}\right)\right] \\ +E\left[2R_o \cdot \sqrt{I_{0,n}^{'\,2}+Q_{0,n}^{'\,2}} \cdot \cos\left(\angle\left(I_{0,n}^{'\,2}+Q_{0,n}^{'\,2}\right)+\theta_o[i]-\theta_b[i]\right)\cdot N_I\right] \\ +E\left[2R_o \cdot \sqrt{I_{0,n}^{'\,2}+Q_{0,n}^{'\,2}} \cdot \sin\left(\angle\left(I_{0,n}^{'\,2}+Q_{0,n}^{'\,2}\right)+\theta_o[i]-\theta_b[i]\right)\cdot N_Q\right] \\ +E\left(N_I^{\,2}\right)+E\left(N_Q^{\,2}\right)\end{array}}{P_{avg}}} \\
&= \sqrt{\frac{R_o^{\,2}\cdot P_{avg}+0+0+2\sigma^2}{P_{avg}}} \\
&= \sqrt{R_o^2+\frac{3\sigma^2}{4^l-1}}
\end{aligned}
\tag{5.20}
$$

As a result, the EVM_{RMS} has the same expression as that without chaotic phase interference in Eq. (4.16) That is because the chaotic phase noise for the intended user is cancelled at its decoder side while the overlapped symbols the chaotic phase noise forms the noisy constellation around the corresponding reference symbol of the intended user. As the proposed mechanism only add noise to phase component rather than modifying the symbol amplitude, the EVM_{RMS} The BER can thus be linked with SER based on Eq. (4.17) and is given by:(3.26) and is given by:

$$BER\left(l,\sigma,R_o,\theta_b,\theta_o,N\right)=$$

$$\frac{1}{\alpha\cdot N}\sum_{i=1}^{N}\left\{1-\frac{4}{\left(2^{2l}\right)^2}\left[\begin{array}{l}\sum\limits_{c=1,d=1}\sum\limits_{I_2,Q_2}\left(F\left(Q_{1,d}+1-y_{N,d},\sigma\right)-F\left(Q_{1,d}-1-y_{N,d},\sigma\right)\right)\cdot\\ \left(F\left(I_{1,c}+1-x_{N,c},\sigma\right)-F\left(I_{1,c}-1-x_{N,c},\sigma\right)\right)\\ +2\sum\limits_{c=1,d=2}\sum\limits_{I_2,Q_2}F\left(-\left(Q_{1,d}-1-y_{N,d}\right),\sigma\right)\cdot\\ \left(F\left(I_{1,c}+1-x_{N,c},\sigma\right)-F\left(I_{1,c}-1-x_{N,c},\sigma\right)\right)\\ +\sum\limits_{c=2,d=2}\sum\limits_{I_2,Q_2}F\left(-\left(Q_{1,d}-1-y_{N,d}\right),\sigma\right)\cdot\\ F\left(-\left(I_{1,c}-1-x_{N,c}\right),\sigma\right)\end{array}\right]\right\}$$

$$F\left(\omega,\sigma\right)=\int_{-\infty}^{\omega}\frac{1}{\sigma\sqrt{2\pi}}\exp\left(-\frac{x^2}{2\sigma^2}\right)dx$$

(5.21)

As it has been demonstrated that the proposed secure mechanism is robust against eavesdropper's exhaustive searching accuracy as high as 10^{-10} when the keys are selected outside the islands of stability, we equip two users each with the key outside the islands of stability, i.e. user-1: r = 3.75, x_1 = 0.66; user-2: r = 3.81, x_1 = 0.28, as an example to evaluate the BER performance with code misalignment and chaotic phase. Fig. 5.21 shows the analytical BER simulated based on Eq. (5.21) for 4-QAM and 16-QAM modulation formats.

Overall speaking, it can be observed from Fig. 5.21 that 16-QAM modulation format is less resilient to the code misalignment than 4-QAM modulation format. Once the keys are set, the BER performance is only dependent on code overlapping ratio and signal SNR for a specific modulation format, and when overlapping ratio is relatively high, the impact of signal SNR becomes negligible. Moreover, from Eq. (5.16)~(5.21) = 3.75 and x_1 = 0.66, and then further evaluate the BER performance of the intended user with different values of r for the overlapped adjacent user (user-2) while the initial value for user-2 is still fixed as 0.28 since it has negligible impact on the system performance as shown in the previous discussions. The value of σ is set as 0.1 to indicate the same signal SNR level for both modulation formats.σ is set as 0.1 to indicate the same signal SNR level for both modulation formats.

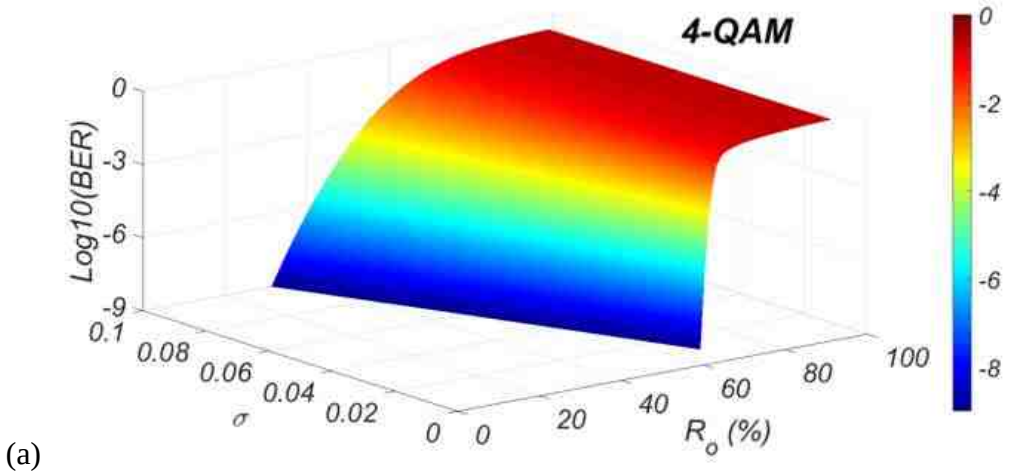

(a)

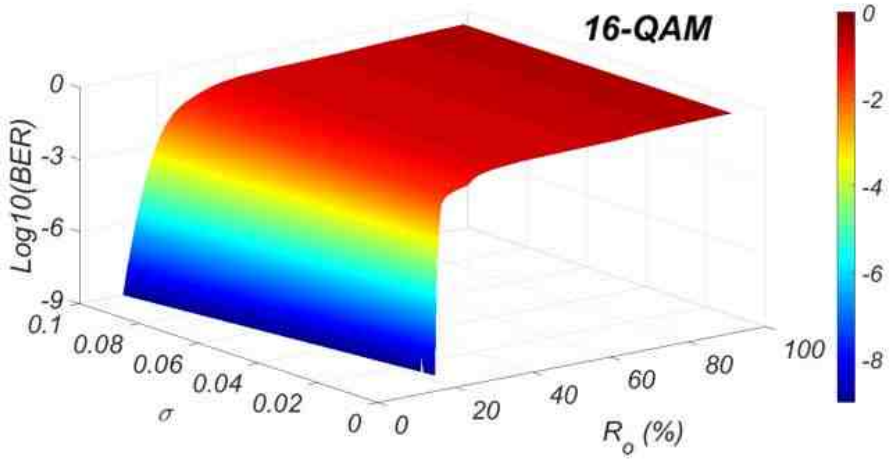

(b)

Fig. 5.21 Analytical BER performance with R_o and σ for (a) 4-QAM and (b) 16-QAM for two users with keys outside the islands of stability (user-1: r = 3.75, x_1 = 0.66; user-2: r = 3.81, x_1 = 0.28).

As shown in Fig. 5.22, the BER of the intended user with the key outside the islands of stability increase as the overlapping ratio becomes larger for both modulation formats. At the same time, the value of r for the overlapped adjacent user (user-2) has ignorable impact on the intended user's BER. That is because the EVM_{RMS} in the proposed system does not depend on the chaotic phase as described in Eq. (5.20).

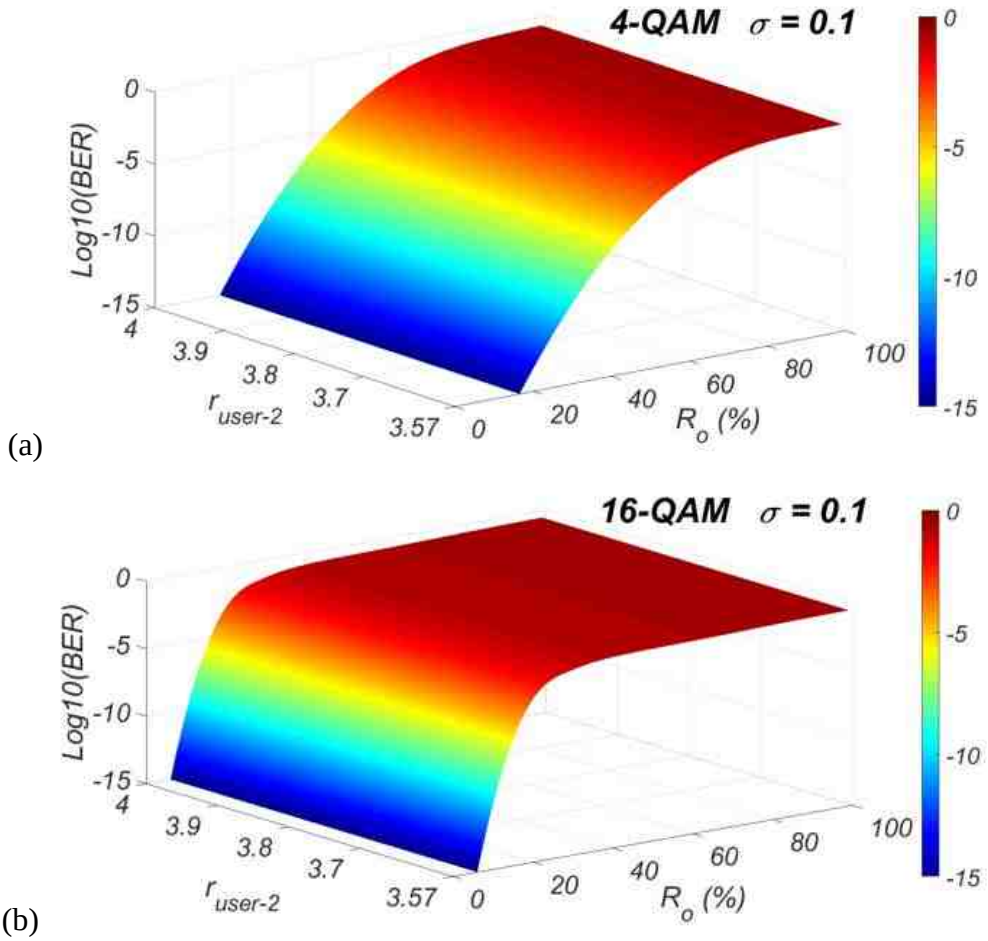

Fig. 5.22 Analytical BER performance as a function of R_o and different values of r for user-2 in (a) 4-QAM and (b) 16-QAM modulated system

In terms of experimental verification, two users were considered for simplicity and both users were assigned with r provides chaotic manner and thus has low outage rate (user-1: r = 3.75, x_1 = 0.66; user-2: r = 3.81, x_1 = 0.28). The high noise rate is also offered by the selected keys according to the results shown in Fig. 5.3. The BER of two users at three distances from the beam centre with different overlapping ratios were tested using experimental setup described in Fig. 5.5 with around 20 cm beam waist at the receiver plane, and both 4-QAM and 16-QAM modulations were taken into consideration.

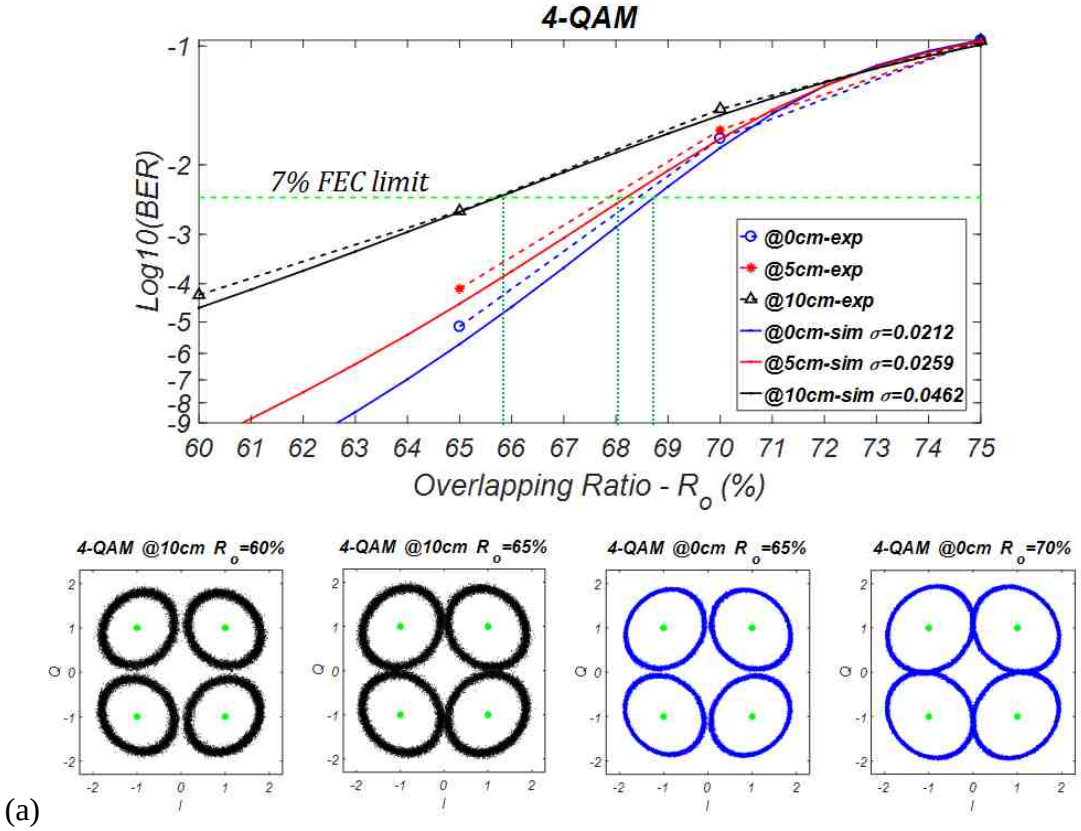

(a)

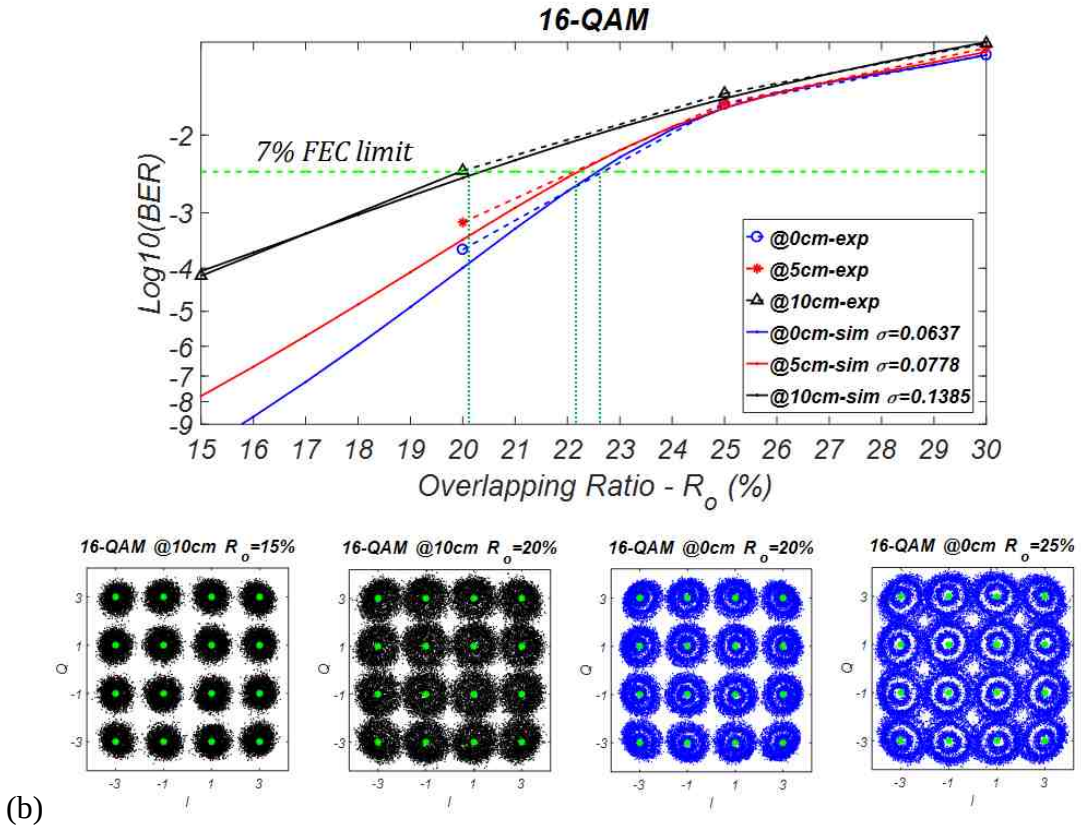

(b)

Fig. 5.23 BER performance and signal constellation examples in terms of overlapping ratio with different user locations for secured (a) 4-QAM and (b) 16-QAM transmission

Fig. 5.23 shows both results measured in the experiments and those calculated according to the derived analytical model. Received signal constellations with different overlapping ratios and at different locations are included for illustration. Experimental results display satisfactory matching with simulation results calculated using Eq. (3.25) (5.21), 5 cm and 10 cm in the experiments was measured as -20.2 dBm, -21.4 dBm and -24.3 dBm respectively. It also can be seen that the error-free detection at the beam centre can be realised with a maximum overlapping ratio of 68.6% and 22.6% for 4-QAM and 16-QAM systems, respectively. Furthermore, with the increasing overlapping ratio, the BER results at different locations become merged as the overlapping ratio starts to dominate in system performance rather than signal SNR.68.6% and 22.6% for 4-QAM and 16-QAM systems, respectively. Furthermore, with the increasing overlapping ratio, the BER results at different locations become merged as the overlapping ratio starts to dominate in system performance rather than signal SNR.

5.5 Conclusions

In this chapter, we have proposed an effective mechanism to provide multiple secure connections in indoor OWC system, whereby the TSC scheme is responsible for multiple access and the chaotic phase sequence generated based on the logistic map is employed to protect each connection from potential eavesdropping. Both analytical and experimental results have shown that it is feasible for the proposed mechanism to provide secure OWC connections. The analytical results indicate that the value of *r* dominates both the noise rate and the outage rate. The experiments have shown that SER without the knowledge of key always exceeds the 7% FEC limit, which means an illegal user cannot detect the signal without the key. What is more, the experiments have demonstrated that adding the chaotic phase does not affect the signal quality of each legitimate user. In terms of robustness of the proposed mechanism, theoretical analysis has been completed for the tolerance against eavesdropper's exhaustive search

and code misalignment issue. Experimental results have illustrated satisfactory agreement with the corresponding analytical results and shown that the proposed mechanism is robust against both eavesdropper's high searching accuracy of 10^{-10} and code misalignment, where the maximum code overlapping ratio for error-free operation is 68.6% and 22.6% for 4-QAM and 16-QAM modulated systems.

Chapter 6 Key System Parameters in High-speed Indoor Optical Wireless Communications

6.1 Introduction

In previous chapters, we have devised a novel OWC system for in-building applications, and ultra-broadband communications for multiple users simultaneously and securely can be established. Proof-of-concept experiments have been carried out with an expanded beam waist of 20 cm and a maximised bit rate of 2.5 Gb/s for 4-QAM and 4 Gb/s for 16-QAM. However, due to the availability of lenses, limited laser source output powers, coupling losses as well as D/A sampling frequency, the achievable system data rate is restricted in experimental demonstrations. In addition, it is not realistic to thoroughly investigate the impacts of several key parameters, including the transmission optical power, laser *RIN* level, expanded beam waist, background light power, and time-slot code overlapping ratio, on system performances, such as the maximum error-free coverage for various data rates via experiments.

Consequently, we extensively evaluate the indoor OWC system performance with general square QAM modulation format under different key parameters by using the analytical model derived and experimentally verified in previous chapters. The optimal beam waist is captured for the data rate in demand, and the corresponding maximum error-free coverage provided by a single transmitter is studied based on 4-QAM and 16-QAM modulation formats. Furthermore, the transmitted optical power and laser RIN property are investigated showing that the system performance is not limited by the intensity noise although increasing optical power results in higher intensity noise. The

impact of background light induced noise on the receiver sensitivity of multiple data rates based on 4-QAM and 16-QAM modulated system is evaluated both experimentally and analytically. Finally, the code misalignment as another key factor in multiple access OWC network is analysed and discussed. Analytical results shows that the code misalignment tolerance with secure connection is worse than that without secure communications due to the introduction of chaotic phase interference from the overlapped adjacent users. Although the 16-QAM modulated system is less tolerant to code misalignment than the 4-QAM based indoor OWC system, the code misalignment tolerance degradation due to chaotic phase is smaller.

The rest of this chapter is organised as follows:

Section 6.2 investigates the impacts of key transmitter parameters on the maximum error-free coverage, including beam waist after expanding, transmitted optical power and laser *RIN*. The SNR penalty introduced by the intensity noise is also derived and analysed. In Section 6.3, the impacts of background light and preamplifier induced noise are investigated and discussed. Finally, Section 6.4 provides the analysis of code misalignment tolerance for multiple data rates up to 10 Gb/s and shows comparison between scenarios with and without the chaotic phase.

6.2 Impacts of Transmitter Parameters

As discussed in Section 3.2, a single transmitter together with adaptive lens system is employed in the proposed indoor OWC system to cover a certain area at the user side. The beam width at the receiver plane can be adjusted by controlling the distance between the lens and the fibre end according to Eq. (3.2)(3.4)user terminal with a specific transmission power and receiver area is dependent on the beam width after expanding and the distance from the beam centre as described in Eq. (3.5). Fig. Fig. 6.1with respect to the distance from the beam centre under different beam waists, where the transmission power is restricted by eye and skin safety regulations and is set as 7 mW. The receiver area is 2 cm and the coupling loss is assumed to be 0 dB. Due to the

symmetry of optical power distribution, only one direction from the beam centre is shown.centre is shown.

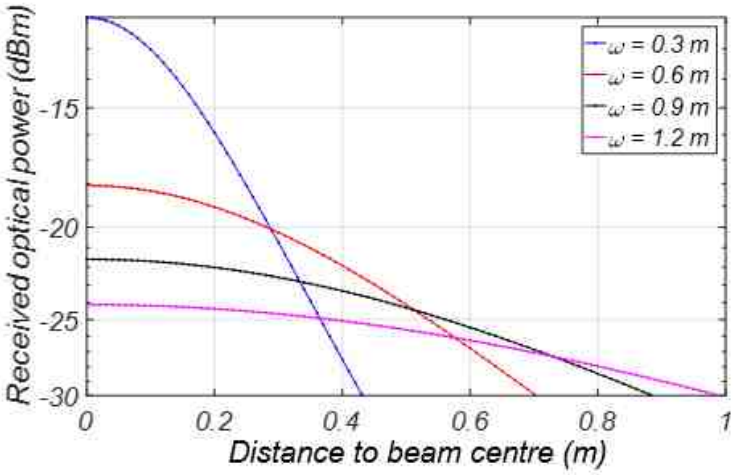

Fig. 6.1 Received optical power with respect to distance from beam centre under different beam waist (ω)

It is intuitive that the optical beam spreads to cover larger area with a larger beam waist at the receiver plane, however, the received optical power at the beam centre degrades accordingly as illustrated in Fig. 6.1. What is more, for a specific bit rate with certain receiver sensitivity, i.e. the minimum received optical power that provides error-free transmission, there is an optimal beam waist that could provide the largest error-free coverage by a single transmitter. For example, the beam waist of 0.6 m, 0.9 m and 0.3 m provides the successively larger error-free coverage areas with a received sensitivity of -23.5 dBm, while the beam waist of 1.2 m fails to provide error-free connection under this condition. As a result, we further test the BER performance with different beam waists when the user is moving away from the beam centre. Other key system parameters used in the analysis are summarised in Table 3. Fig. 6.2 – (a) shows the analytical results calculated using the system model developed in Section 3.3 for both 4-QAM and 16-QAM modulation formats with 10 Gb/s system capacity, and the BER threshold plane of 3.8×10^{-3} is also included to indicate the error-free coverage.

Transmission power (P_t)	7 mW	Receiver area (S_{rx})	$\pi \times 2^2$ cm^2
RIN	-118 dB/Hz	Responsivity (R)	0.8 A/W
Background light power (P_{bn})	-30.12 dBm	Coupling loss	0 dB

Table 3 Key system parameters used in investigating beam waist impact

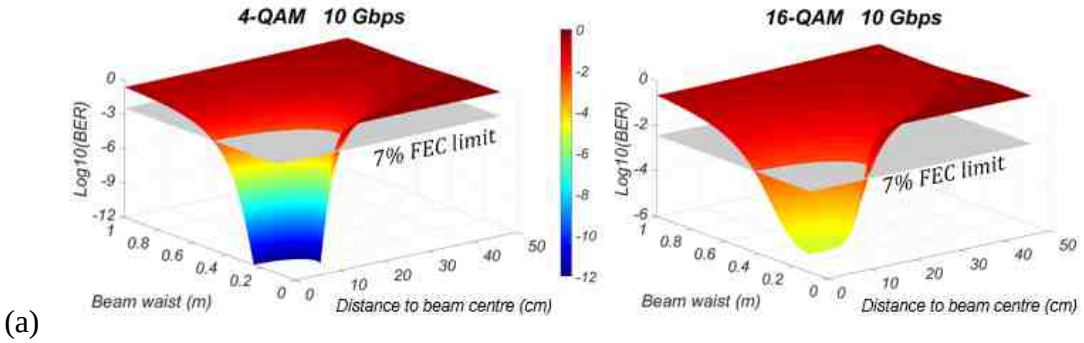

(a)

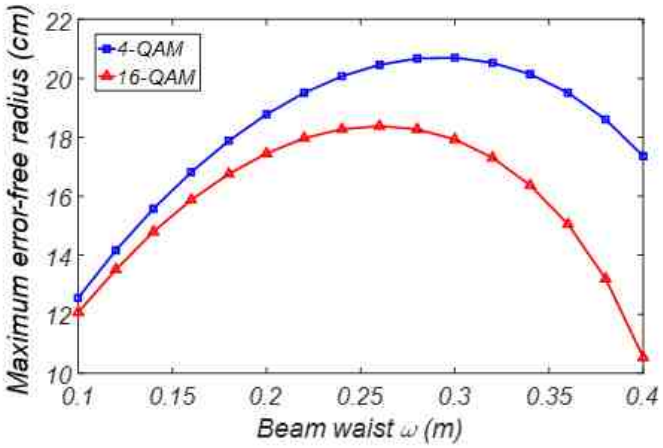

(b)

Fig. 6.2 (a) BER performance with respect to user location and beam waist for 10 Gb/s 4-QAM and 16-QAM; (b) Maximum error-free radius with different beam waists

Fig. 6.2 – (b) illustrates the intersection of the analytical BER results and the BER threshold plane, which indicates the largest coverage (in radius from beam centre) that can provide error-free transmission. It can be observed that there is an optimal beam waist to achieve maximised error-free coverage, and the error-free coverage size is reduced beyond this optimal point. We further analyse the achievable maximum error-free coverage provided by a single transmitter for the 4-QAM and 16-QAM systems

with different bit rates ranging from 1 Gb/s to 10 Gb/s and the corresponding optimal beam waist.

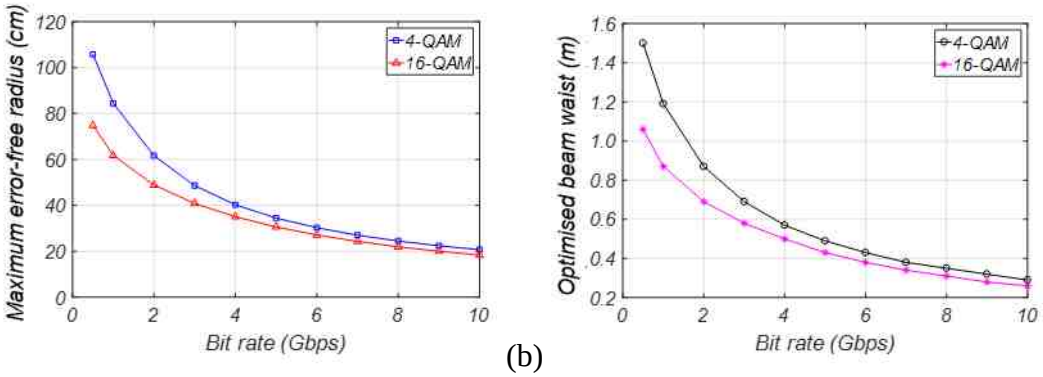

(a) (b)

Fig. 6.3 (a) Maximum error-free coverage and (b) corresponding beam waist for 4-QAM and 16-QAM with different data rates

As illustrated in Fig. 6.3, the largest error-free radius and the corresponding optimal beam waist decreases with an increasing data rate for both 4-QAM and 16-QAM modulation formats due to the increased bandwidth-related noise. For a specific bit rate, 4-QAM is able to provide larger error-free coverage compared to 16-QAM as it requires less SNR. However, the difference in achievable error-free radius between 4-QAM modulated system and 16-QAM modulated system becomes less significant when the bit rate increases, where there is 30.92 cm difference for the system capacity of 1 Gb/s and only 2.33 cm for the 10 Gb/s system. Thus, the higher-order 16-QAM modulation format is more appropriate than 4-QAM for high data rate systems exceeding 10 Gb/s, as it is more spectrally efficient and requires more cost-effective opto-electronic devices with smaller bandwidth. What is more, with the aid of the derived system analytical model and the results shown in Fig. 6.3, the lens configuration at the transmitter side can be adjusted adaptively according to the user's location and system capacity requirement.

In addition to the optical beam waist at the receiver plane, another key parameter of the optical wireless transmitter is the transmitted optical power, which is measured after the fibre end at the transmitter end, as it directly results in received optical power changes and thus affects the signal SNR. On one hand, increasing the optical transmission power is able to improve the received signal power. On the other hand, it

is also related to RIN noise as described in Eq. (3.24)an increased optical power. increased optical power.

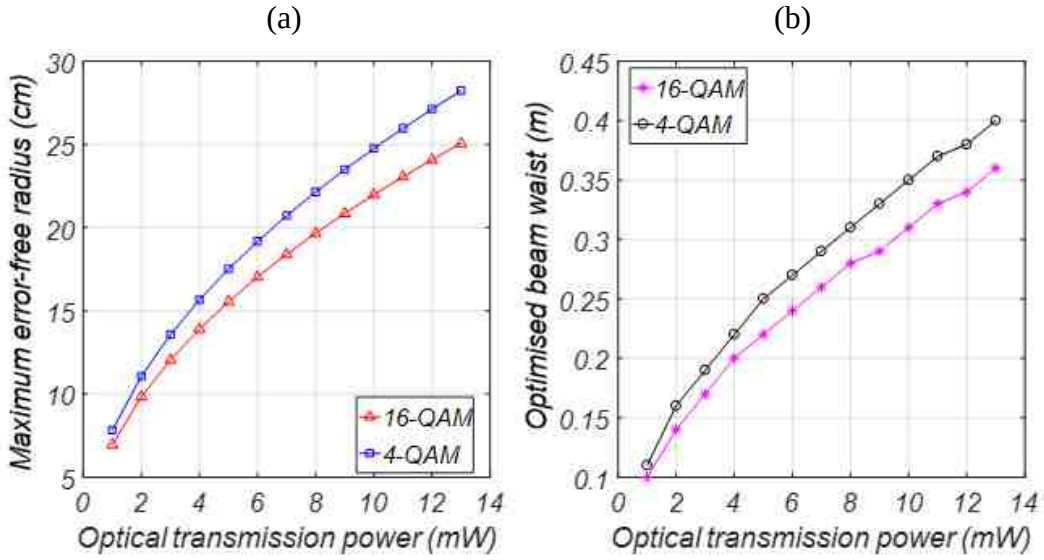

Fig. 6.4 (a) Maximised error-free coverage and (b) corresponding optimal beam waist in terms of transmission power for 10 Gb/s 4-QAM and 16-QAM

Analytical results of maximised achievable error-free coverage and the corresponding employed optical beam waist are illustrated in Fig. 6.4. Key system parameters are set as the same as those in Table 3 except the transmission power while the bit rate is fixed at 10 Gb/s. It can be seen that the error-free coverage is enlarged by increasing transmission power for both 4-QAM and 16-QAM modulation formats Although increasing the transmission power results in higher level of the RIN noise, the increase in signal power dominates the change of signal SNR. As a result, the error-free area and the corresponding beam waist can be decided by controlling the transmission power for a specific system capacity. In addition to modifying the transmission power, the received optical power can also be increased by employing the receiver with larger detective area.

As mentioned in Section 3.3.2, the contribution of the laser intensity fluctuations to the total electrical noise at the receiver is included in the analytical model. As another key parameter at the transmitter side, we further investigate the impacts of laser *RIN*. The BER performances in terms of the distance from beam centre under various values of *RIN* for 4 Gb/s 4-QAM and 16-QAM modulated OWC systems are shown as an

example in Fig. 6.5. The optical beam waist is selected as the optimal value for the 4 Gb/s bit rate according to Fig. 6.3, i.e. 57 cm for 4-QAM and 50 cm for 16-QAM. Other parameter settings are the same as shown in Table 3 except that *RIN* is treated as a variable. The intersections of the BER surface and the BER threshold plane for both modulation formats are illustrated in Fig. 6.6.

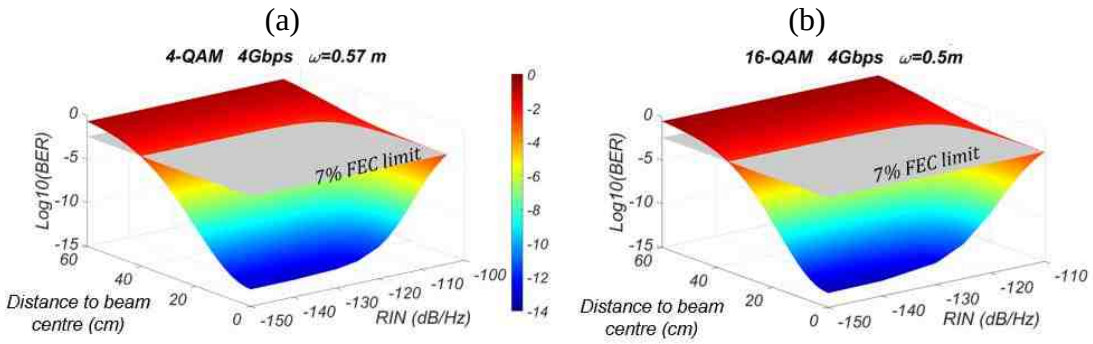

Fig. 6.5 BER performance at different locations for (a) 4 Gb/s 4-QAM and (b) 4 Gb/s 16-QAM system with respect of different *RIN* values

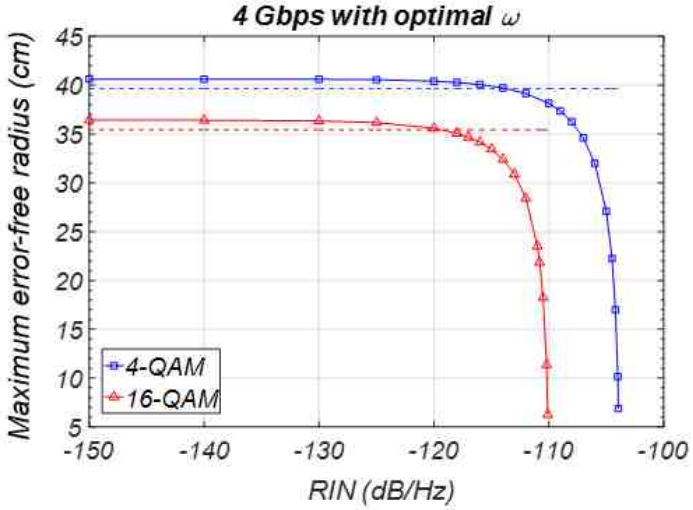

Fig. 6.6 Maximised error-free distance from beam centre with respect to different values of RIN for 4Gb/s 4-QAM and 16-QAM system

Results above show that the achievable error-free coverage becomes larger by decreasing *RIN* value, However, it maintains relatively stable after a certain value of *RIN* for both modulation formats. We here define the error-free radius increment threshold as the point where the maximally achievable error-free radius is reduced by

1 cm due to the reduction of *RIN*. As we can see from Fig. 6.6, for 4 Gb/s indoor OWC system, there is only marginal improvement (< 1 cm) in the error-free coverage when the *RIN* is smaller than -113.7 dB/Hz for the 4-QAM modulation format and when it is smaller than -119.3 dB/Hz for the 16-QAM modulation format. The same analysis as shown in Fig. 6.5 and Fig. 6.6 can be carried out for other system capacities as well.

Here, the SNR penalty due to intensity noise is theoretically studied for different bit rates. With a certain received optical power (P_r), we define the SNR penalty ($SNR_{penalty}$) as the difference between the SNR values in dB with and without the intensity noise. For the system employing a laser source with relatively stable output, the intensity noise can be ignored and the SNR (SNR_{wo}) without the intensity noise is thus estimated as:

$$SNR_{wo} = \frac{\left(R \cdot P_r\right)^2}{\beta\left(N_{pr}^2 + N_{bn}^2\right)} \tag{6.1}$$

In contrast, the SNR considering the intensity noise (SNR_w) is calculated as:

$$SNR_w = \frac{\left(R \cdot P_r\right)^2}{\beta\left(N_{pr}^2 + N_{bn}^2 + \left(R \cdot P_r\right)^2 \cdot RIN \cdot B\right)} \tag{6.2}$$

Consequently, the SNR penalty in dB with a fixed received optical power is derived as:

$$\begin{aligned} SNR_{penalty}\left(dB\right) &= 10\log_{10}\left(\frac{SNR_{wo}}{SNR_w}\right) \\ &= \frac{N_{pr}^2 + N_{bn}^2 + \left(R \cdot P_r\right)^2 \cdot RIN \cdot B}{N_{pr}^2 + N_{bn}^2} \end{aligned} \tag{6.3}$$

It can be concluded that the SNR penalty induced from the intensity noise is not dependent on the modulation format for a certain signal bandwidth. The SNR penalty result is plotted in Fig. 6.7 for 2 Gb/s, 4 Gb/s, 6 Gb/s, 8 Gb/s and 10 Gb/s, respectively, based on Eq. (6.3) both 4-QAM and 16-QAM modulation formats as an example. It is straightforward that increasing *RIN* results in a larger SNR power penalty for all cases with a fixed received optical power. What is more, with the same *RIN* parameter, the higher bit rate system has less SNR penalty. This is because another principle noise source in the OWC system, the preamplifier induced noise, is more seriously affected by the signal electrical bandwidth with a relationship proportional to B^3, as described

in Eq. (3.23)increase of bit rate, the noise induced by the preamplifier dominates the total noise power.by the preamplifier dominates the total noise power.

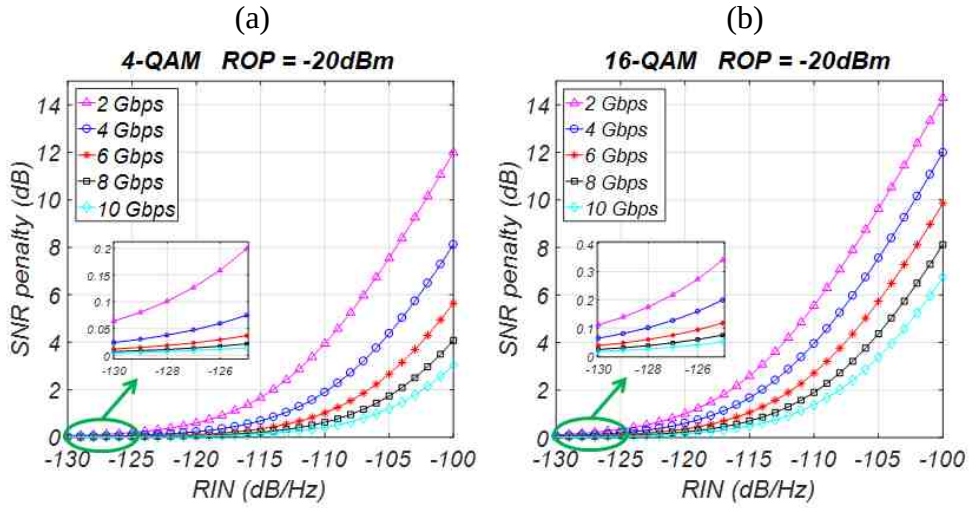

Fig. 6.7 SNR penalty as a function of different values of RIN for 2 Gb/s, 4 Gb/s, 6 Gb/s, 8 Gb/s and 10 Gb/s in (a) 4-QAM system and (b) 16-QAM system

Fig. 6.8 further illustrates the SNR penalty results as a function of bit rates, where two received optical power levels (-20 dBm and -23 dBm) are evaluated with 5 different *RIN* parameters, i.e. -105 dB/Hz, -110 dB/Hz, -115 dB/Hz, -120 dB/Hz and -125 dB/Hz. It is obvious that higher received optical power results in larger SNR penalty with the same *RIN* and bit rate. This is because that the intensity noise is proportional to the received optical power. Furthermore, the intensity noise has more serious impact on the 16-QAM modulation format compared with 4-QAM when the bit rate is fixed. That is because the 16-QAM modulated siganl occupies half of the electrical bandwidth of the 4-QAM modulated signal with the same bit rate. For a well-designed laser source with the value of *RIN* lower than -115 dB/Hz, the SNR penalty induced from the intensity noise can be limited to smaller than 3.5 dB when the optical power at the receiver side is lower than -20 dBm.

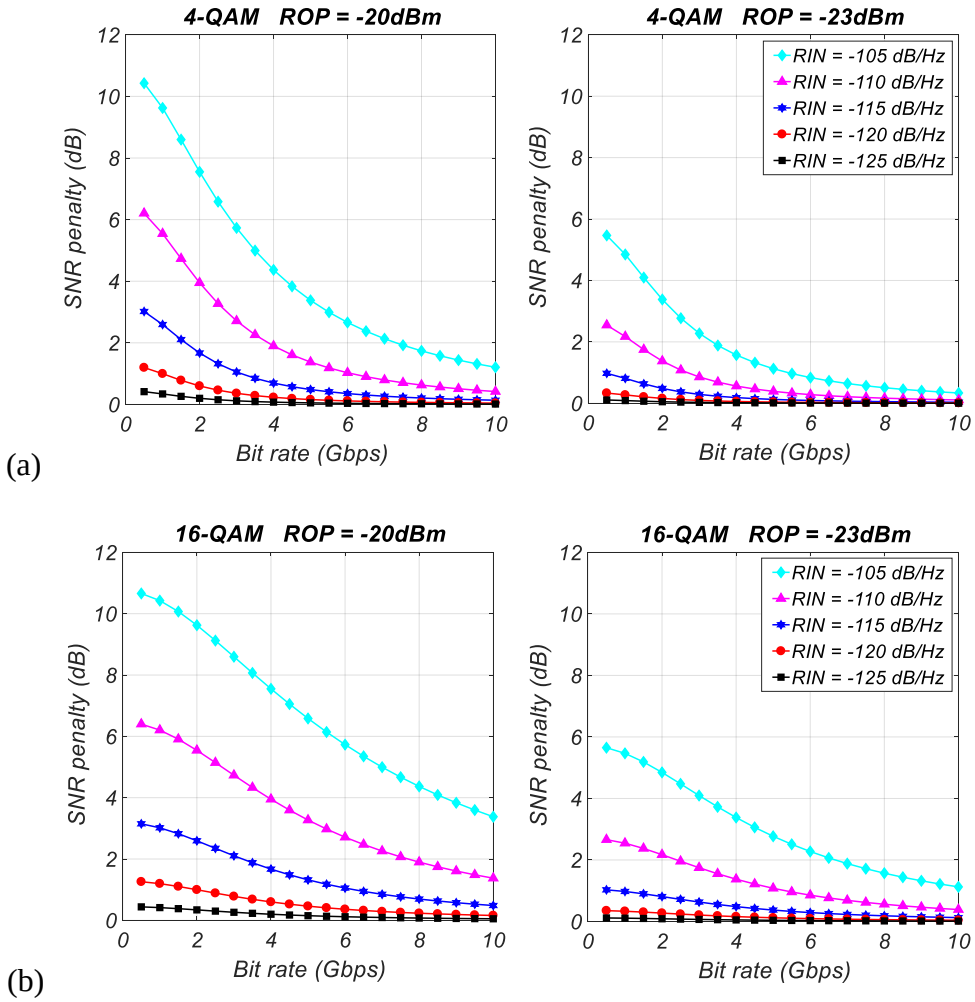

Fig. 6.8 SNR penalty in terms of bit rates with two received optical power level (-20 dBm and -23 dBm) for (a) 4-QAM and (b) 16-QAM

6.3 Impacts of transmission channel and receiver

We have thoroughly investigated the impacts of key factors at the transmitter side on the system performance in the last section. In this section, we further investigate the impacts of typical OWC transmission channel and the preamplifier noise from the receiver. Compared with optical fibre transmissions, in optical wireless communications, the background light from indoor lighting system and outdoor sunlight interferes with the data-carrying optical signal. Here, we first evaluate the

receiver sensitivity with and without the background light through both the analytical model and experiments. The BER threshold employed to obtain the receiver sensitivity is consistent as 7% FEC limit (3.8×10^{-3}).

The experimental setup is shown in Fig. 3.4, where the background light power was measured after the lens at the receiver side using a free space optical power meter with the optical signal turned off. In the experiment, a desk lamp was employed at the receiver to provide strong background light, which was measured as -24.36 dBm. The lamp was turned off for the scenario without background light.

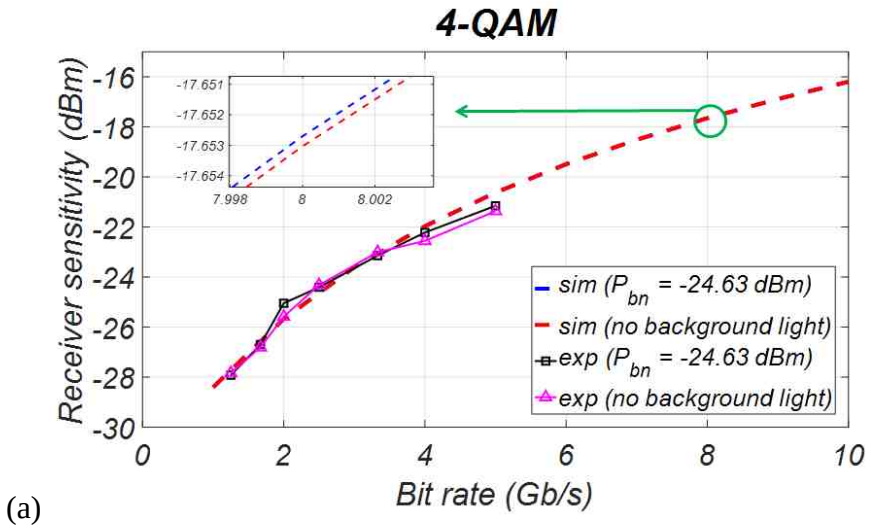

(a)

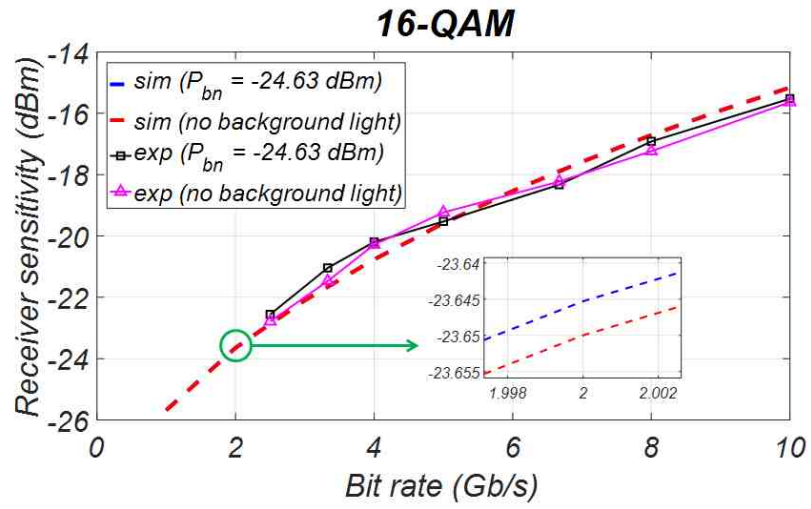

(b)

Fig. 6.9 Analytical and measured receiver sensitivity of indoor OWC system with and without background light for (a) 4-QAM and (b) 16-QAM

As illustrated in Fig. 6.9, the analytical and measured results agree well with less than 1 dB difference. Although the receiver sensitivity becomes worse when the background light of -24.36 dBm is incorporated, both experimental results and simulation results show that the difference in the receiver sensitivity for the system with and without the background light is negligible. We further investigate the power penalty (PP_{bn}) introduced by the background light, which is defined as the difference in the required received optical power to achieve the same signal SNR. Since the principal noise sources for typical indoor OWC system include the preamplifier induced noise, the intensity noise and the background light induced noise, the SNR without the background light noise is calculated as:

$$SNR_{wo} = \frac{\left(R \cdot P_{r-wo}\right)^2}{\beta\left(N_{pr}^2 + \left(R \cdot P_{r-wo}\right)^2 \cdot RIN \cdot B\right)} \tag{6.4}$$

where P_{r-wo} is the required received optical without any background light to achieve SNR_{wo} . Similarly, the SNR with the presence of the background light (SNR_{wo}) is expressed as:

$$SNR_{w} = \frac{\left(R \cdot P_{r-w}\right)^2}{\beta\left(N_{pr}^2 + N_{bn}^2 + \left(R \cdot P_{r-w}\right)^2 \cdot RIN \cdot B\right)} \tag{6.5}$$

Let Eq. (6.4)=(6.5), we then have:

$$\frac{N_{pr}^2 + N_{bn}^2}{P_{r-w}^2} + R^2 \cdot RIN \cdot B = \frac{N_{pr}^2}{P_{r-wo}^2} + R^2 \cdot RIN \cdot B \tag{6.6}$$

Consequently, the power penalty in dB introduced by the background light can be given by:

$$PP_{bn}(dB) = 10\log_{10}\left(\frac{P_{r-w}}{P_{r-wo}}\right) = 5\log_{10}\left(\frac{N_{pr}^2 + N_{bn}^2}{N_{pr}^2}\right) \tag{6.7}$$

According to the derivation shown in Eq. (6.7)*RIN* noise or dependent on the modulation format for a certain signal bandwidth. The analytical results with respect to different system capacities for 4-QAM and 16-QAM modulation formats are plotted in Fig. 6.10

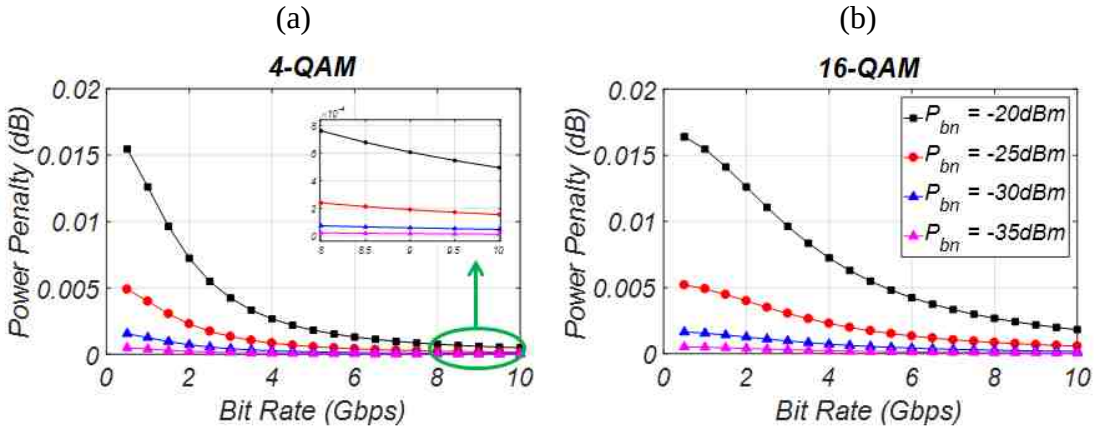

Fig. 6.10 Analytical results of the power penalty introduced by the different power levels of background light in terms of data rates for (a) 4-QAM and (b) 16-QAM.

It can be seen from Fig. 6.10 that the power penalty increases with stronger background light but decreases with the system capacity for both modulation formats investigated. What is more, the power penalty in 16-QAM modulated indoor OWC system is slightly higher than that in 4-QAM system with the same system capacity, which means the background light has more impact on higher order modulation format for a specific bit rate. However, the power penalty remains lower than 0.02 dB even with the presence of strong background light power of -20 dBm in our system since the preamplifier induced noise plays a more dominant role.

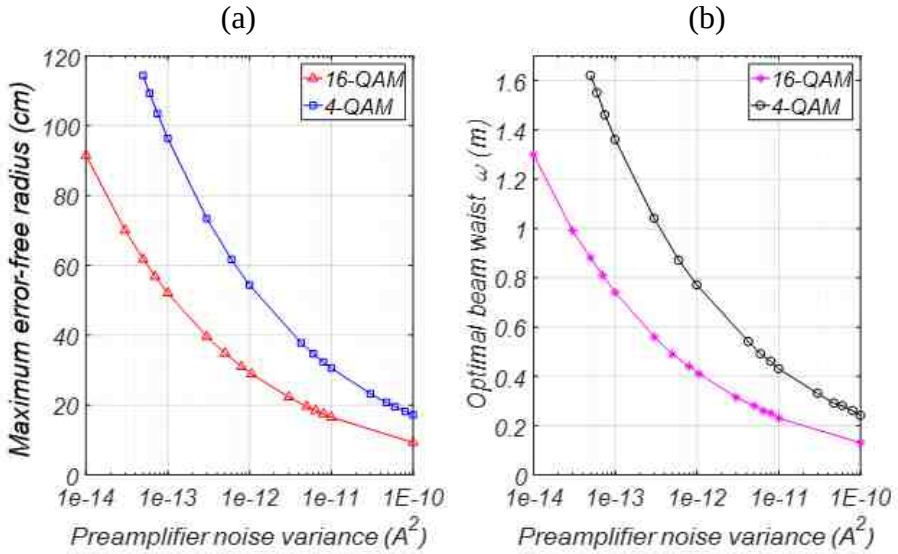

Fig. 6.11 (a) Maximised error-free coverage and (b) corresponding optimal beam waist in terms of preamplifier induced noise for 10 Gb/s 4-QAM and 16-QAM

We then investigate the impact of preamplifier noise level on the error-free coverage in a 10 Gb/s system. The maximum error-free radius and the corresponding optimal beam waist for both 4-QAM and 16-QAM are shown in Fig. 11, when the transmission optical power is 7 mW and other parameters are the same as listed in Table 3.

It is straightforward that increasing the preamplifier induced noise power dramatically degrades the system error-free coverage. As described in Eq. (3.23)B^3) and the ratio of the square of total input capacitance and the FET trans-conductance (C_T^2/g_m Furthermore, the photodetector speed is mainly determined by the photodetector capacitance [152]. In order to reduce the preamplifier noise while maintaining high-speed detection, large number of studies have been carried out to design photodiodes with low capacitance by using advanced CMOS technology [152 -156].].

6.4 Impact of Code Misalignment

In the proposed multiple access scheme for indoor OWC system supporting secure connections, another key factor that significantly affects the system performance is the code misalignment as it governs the interference between adjacent users. In Section 4.4 and Section 5.4.2, the analytical BER with code overlapping ratio has been illustrated with respect to different standard deviations of the received signal in Fig. 4.19 and Fig. 5.21. However, the maximum symbol rate demonstrated in the experiments for both 4-QAM and 16-QAM for both modulation formats is only 125 Mb/s due to hardware limitations. In this section, the analysis of code misalignment is extended to the indoor OWC system with higher-speed connections via the analytical model developed in previous chapters.

We first evaluate the BER performance without secure transmission as a function of code overlapping ratio (R_o) at the beam centre. Based on the derivation shown in Eq. (4.18). The key system parameters used in the simulation are listed in Table 3 combination of bit rate and modulation format, the beam waist is selected as the optimal

beam waist that provides the largest error-free coverage according to the results shown in Fig. 6.3 The code misalignment tolerance definition is consistent with that in Section 4.4 and Section 5.4.2, which is the largest overlapping ratio that the system is tolerant to achieve error-free connections (7% FEC limit: BER ≤ 3.8×10^{-3}). .

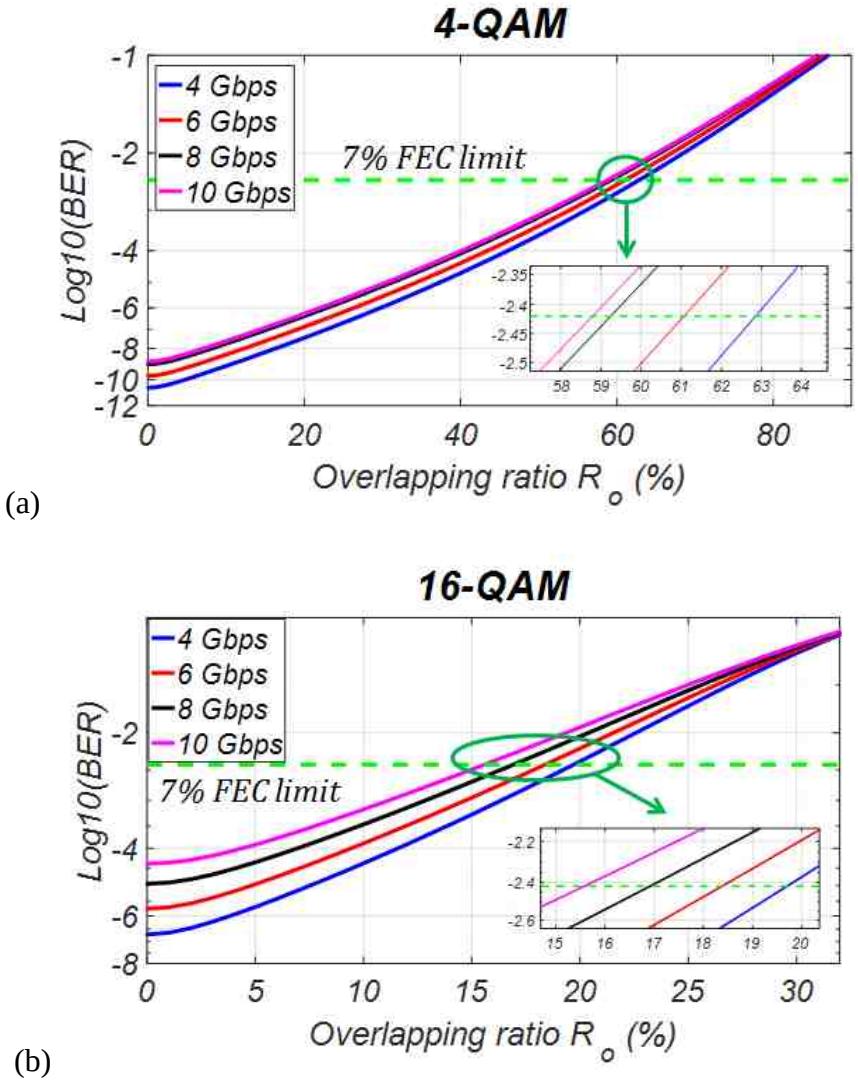

Fig. 6.12 Analytical BER results in terms of code overlapping ratio for 4 Gb/s, 6 Gb/s, 8 Gb/s and 10 Gb/s at beam centre for (a) 4-QAM and (b) 16-QAM

It can be seen that the system with lower bit rate is more tolerant to code misalignment due to less bandwidth-related noise. With the optimal beam waist, the code misalignment tolerance difference at the beam centre for the bit rate from 4 Gb/s to 10 Gb/s is well controlled within 5%. For 10 Gb/s system with the optimal beam waist, the

maximal code misalignment tolerance at the beam centre can be 58.8 % for the 4-QAM modulation format and 15.5 % for the 16-QAM modulation format.

However, the tolerance decreases with the distance from the beam centre because of the degraded signal SNR as shown in the intersection of the BER with BER threshold plane in Fig. 6.13, which further illustrates the BER performance as a function of both overlapping ratio and the distance from beam centre for the 10 Gb/s system. The code misalignment tolerance gradually decreases to 13 % for 4-QAM and 4 % for 16-QAM at the location of its corresponding maximised error-free radius from the beam centre (4-QAM: 20.72 cm and 16-QAM: 18.39 cm). What is more, decreasing transmission power, reducing receiver area and increasing coupling loss degrade the code misalignment tolerance, which is attributed to the decrease in the received optical power and consequently in the signal SNR.

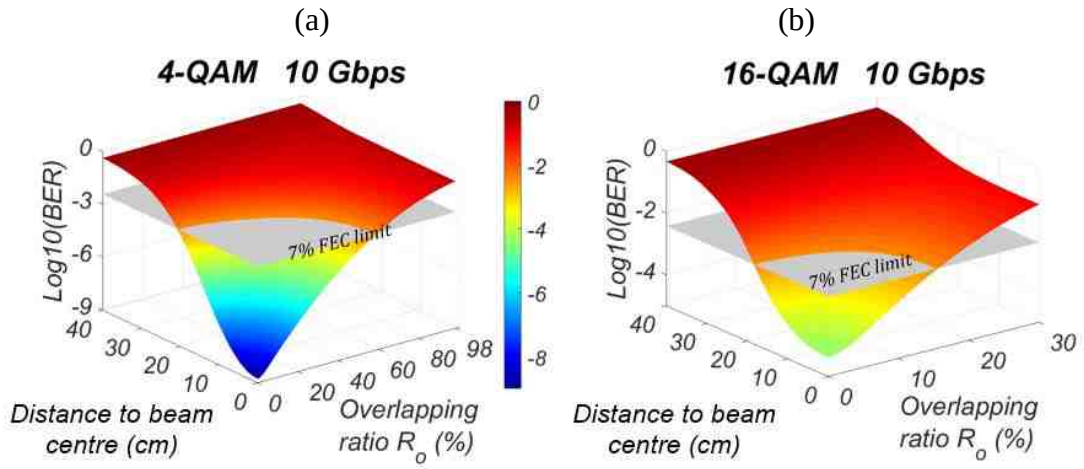

Fig. 6.13 BER performance for 10 Gb/s system with respect to distance to beam centre and code overlapping ratio for (a) 4-QAM and (b) 16-QAM

To address the demand of secure multiple access in indoor OWC networks, the chaotic phase is employed together with the time slot coding scheme. The comparison of the code misalignment tolerance between systems with and without the chaotic phase is shown in Fig. 6.14. System data rates ranging from 1 Gb/s to 10 Gb/s with the corresponding optimal beam waist are evaluated at the beam centre for both 4-QAM and 16-QAM modulation formats. Two users are considered for simplicity and the key selected for each user is outside the islands of stability following the analysis shown in

Section 5.4, for example, r = 3.75, x_1 = 0.66; user-2: r = 3.81, x_1 = 0.28. It is intuitive that the code misalignment tolerance becomes worse due to the chaotic phase interfered from the adjacent users for both modulation formats, and 16-QAM is less immune to the code misalignment issue compared to 4-QAM modulation format. For unsecured multiple OWC connections employing TSC scheme only, the code misalignment tolerance for 10 Gb/s system with optimal beam waist is evaluated at the beam centre as 58.79% and 15.58% for 4-QAM and 16-QAM, respectively. When the proposed chaotic phase is incorporated to provide secure transmission, the code misalignment tolerance correspondingly decreases to 48.22% and 14.67% indicating that the impact of chaotic phase on the code misalignment tolerance is less severe on 16-QAM modulated system. Furthermore, the chaotic phase impact on the code misalignment tolerance becomes smaller as the system bit rate increases.

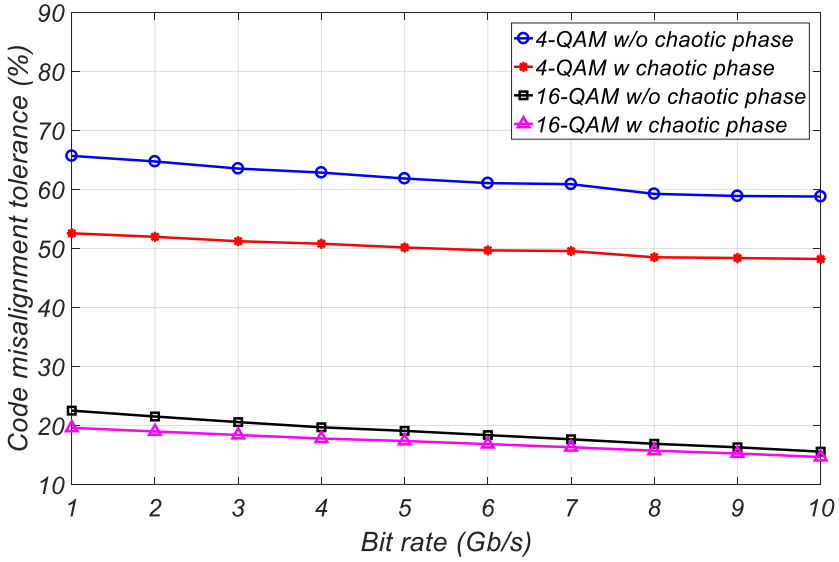

Fig. 6.14 Code misalignment tolerance in terms of bit rates for 4-QAM and 16-QAM with and without chaotic phase.

6.5 Conclusions

Chapter 6

In this chapter, the performance of indoor OWC system based on 4-QAM and 16-QAM modulation format has been comprehensively investigated with the help of the derived system analytical model as described in previous chapters. The optimal beam waist at the receiver side and the corresponding achievable maximum error-free coverage have been studied for both 4-QAM and 16-QAM modulated OWC system with the system bit rate ranging from 0.5 Gb/s to 10 Gb/s. Results show that the maximum error-free radius provided by a single transmitter with the transmission optical power of 7 mW decreases from 105.8 cm to 20.72 cm for 4-QAM and from 74.88 cm to 18.39 cm for 16-QAM with the increased system bit rate. Although the 4-QAM modulation format is able to provide larger coverage, this advantage is less significant for high-speed indoor OWC connections and the higher order modulation format of 16-QAM is superior for higher speed applications due to its higher spectral efficiency. Code misalignment tolerance results have shown that although the 16-QAM modulated system is less tolerant to code misalignment than the 4-QAM based indoor OWC system, the code misalignment tolerance degradation due to chaotic phase is smaller. Last but not least, the system analytical model derived in the previous chapters has shown the capability of comprehensively investigating various aspects of indoor OWC systems. By following similar approaches, the analytical model and analysis can be extended to other modulation formats.

Chapter 7 Conclusions and Future Work

7.1 Thesis Summary

With proliferation of data-intensive applications, such as high-definition video streaming, real-time transmission, virtual reality, augmented reality and tactile communications, it is expected to be a dramatic increase in mobile data traffic especially for indoor scenarios. In addition to providing high data rate transmission, the thesis aims to provide high-speed secure connections to multiple users in an effective and robust way. A novel mechanism employing time-slot coding scheme to support multiple users and chaotic phase to secure each connection is proposed, experimentally demonstrated and investigated in depth. A comprehensive system model is also developed to facilitate performance investigation.

In Chapter 2, several promising candidates that have potential to be deployed for indoor high-speed applications have been comprehensively reviewed and summarised, including Wi-Fi, millimetre-wave, ultra-wide band and optical wireless communications systems. Compared to other techniques, OWC systems have remarkable advantages such as the availability of huge unregulated bandwidth, the immunity to electromagnetic waves, and robustness against interference from radio frequency systems. Different types and configurations of OWC system have been discussed. In addition to high data rate applications, both multiple access techniques and adaptive loading techniques have been reviewed. Furthermore, although OWC system is widely acknowledged with capability to provided physical security due to the optical wave with short wavelength, such security is only considered convincing for

point-to-point links where narrow optical beams are employed. The limited literature has been studied for multi-user accessed OWC system.

The work presented in Chapter 3 provided system model that has been experimentally verified to conduct comprehensive investigation on typical OWC. The SER equation has first been mathematically formulated based on the detection of QAM symbols under a general square constellation with appropriate noise models affecting the specific symbols with the constellation. Noise was represented by the standard deviation of the distribution of the noisy received symbols. Three major noise sources were considered including laser intensity noise, background light induced noise, and preamplifier induced noise. The system BER was further linked with the SER by establishing a relationship between them. Both standard deviation and BER have been experimentally measured and compared to analytical results for 4-QAM and 16-QAM modulated system with multiple data rates, i.e. 1.25 Gb/s, 1.67 Gb/s, 2 Gb/s, 2.5 Gb/s, 3.33 Gb/s, 4 Gb/s and 5 Gb/s for 4-QAM and 2.5 Gb/s, 3.33 Gb/s, 4 Gb/s, 5 Gb/s, 6.67 Gb/s, 8 Gb/s and 10 Gb/s for 16-QAM. The comparison between measured results from experimental demonstration and analytical results obtained via the analytical model showed good agreement in BER, where the maximum receiver sensitivity offset between them is within 0.5 dBm. The verified system model in this chapter has the potential to be modified and thus provides fundamentals for comprehensive investigation of OWC system with QAM modulation formats in the subsequent chapters.

In Chapter 4, we have proposed an effective multiple access scheme named as time-slot coding scheme for OWC systems. The proof-of-concept experiments have been conducted based on both 4-QAM and 16-QAM modulation formats for 5-user, 8-user and 12-user with multiple data rates to demonstrate feasibility of TSC scheme. The experimental results have shown that the BER performance for a certain system capacity does not degrade with the increasing number of users in the system. The adaptive loading function that is compatible with the original TSC scheme, where both 4-QAM and 16-QAM were simultaneously employed and selectively assigned to different users according to their locations, has also been experimentally demonstrated. Experimental results have shown that error-free coverage can be maximally extended by 61.2% when users further away from the beam centre are modulated with normalised 4-QAM. By using the proposed TSC scheme with adaptive loading function, the issues

of requiring heavy overheads in DMT modulation and code redundancy in RAC are alleviated. What is more, switching between different modulation formats and synchronisation problem in TDHMF can be eliminated by applying the proposed time-slot code. The theoretical analysis of time-slot code misalignment issue has been formulated for indoor OWC systems with a general square QAM modulation format. Analytical results indicate that the proposed TSC is more tolerant to the imperfect timing issue compared to the conventional TDMA. The TSC is more desired compared to the conventional TDMA especially for high-speed communications, since imperfect timing issues during the non-ideal hardware implementation procedures for code generation is less likely to happen than that during data acquiring process at the receiver side in the conventional TDMA. The impact of code misalignment on the performance of the TSC scheme has been experimentally verified. Experimental results indicate that code misalignment tolerance larger than 26.9% with 16-QAM and 92.3% with 4-QAM modulation format can be achieved with a received optical power level higher than -19.7 dBm.

In Chapter 5, an effective mechanism to provide secure connections for multiple users in indoor OWC system, whereby the TSC scheme is responsible for multiple access and the chaotic phase sequence generated according to the logistic map is employed to protect each connection from potential eavesdropping. The securing key consists of a constant value r and an initial element x_1. The noise rate was defined and simulated to evaluate feasibility of the proposed mechanism. The analytical results indicated that the value of r dominates both the noise rate. Both analytical and experimental results have shown that it is feasible for the proposed mechanism to provide secure OWC connections while an illegal user cannot detect the signal without the key. What is more, the experiments have demonstrated that there is no power penalty introduced by adding chaotic phase as it can be fully cancelled at each legal user terminal. In terms of robustness of the proposed mechanism, theoretical analysis has been investigated for the tolerance against eavesdropper's exhaustive search and code misalignment issue. Experimental results have illustrated satisfactory agreement with the corresponding analytical results and have shown that the proposed mechanism is robust against both eavesdropper's high searching accuracy of 10^{-10} and code misalignment, where the maximum code overlapping ratio for error-free operation is 68.6% and 22.6% for 4-QAM and 16-QAM modulated systems.

In Chapter 6, the key parameters of indoor OWC system based on 4-QAM and 16-QAM modulation formats have been comprehensively investigated with the aid of the derived system analytical model as shown in the previous chapters. The optimal beam waist at the receiver side and the corresponding achievable maximised error-free coverage have been highlighted for both 4-QAM and 16-QAM modulated OWC system with the system bit rate up to 10 Gb/s. Simulation results illustrated trade-off between system date rate and error-free coverage, where the maximised error-free radius provided by a single transmitter with the transmission optical power of 7 mW decreases from 105.8 cm to 20.72 cm for 4-QAM and from 74.88 cm to 18.39 cm for 16-QAM. Although 4-QAM modulation format is able to provide larger coverage, this advantage is less significant for high-speed indoor OWC connections and the higher order modulation format of 16-QAM is superior for higher speed applications due to its higher spectral efficiency. Code misalignment tolerance results with multiple date rates have shown that although 16-QAM is less immune to the code misalignment issue compared to 4-QAM modulation format, it has less degradation in code misalignment tolerance when the chaotic phase is introduced. Last but not least, the system analytical model derived in the previous chapters has shown the capability of comprehensively investigating various aspects of indoor OWC system. By following a similar convention, the analytical model and analysis have potential to be extended to other modulation formats.

7.2 Future Work

An effective and robust multi-user access scheme with secure capability was proposed and experimentally demonstrated to provide downlink services for indoor OWC system. The system model derivation, analytical studies of key system parameters, mechanism limitation studies and experimental demonstration were performed in depth. During investigation carried out for this thesis, several aspects with potential to be beneficial for realistic indoor OWC system would be extended for further study.

- In this thesis, experimental demonstration and theoretical formulation for the proposed secure multi-user mechanism are studied based on QAM modulation formats. Given the phase terms can be effectively introduced and the mathematically formulated system model has the potential to be adapted to examine the performance of other modulation formats, benefits of such complex formats can be studied and compared. In addition, as the system inevitably requires non-linear devices, such as MZM and electrical amplifier, non-linear distortion to the signal exists and may have more impact on more complex modulation formats. Accordingly, it would be appreciated to comprehensively investigate the non-linearity effects and apply potential non-linearity compensation methods to further optimise the system performance.
- The investigations in this thesis have focused on approaches for downlink transmission, while realistic deployments would need to cater full-duplex multiple access. Uplink transmission with multi-user capability needs to be further studied including system architecture and multiple access techniques for uplink services. A coordination mechanism using TSC scheme is expected to realise uplink request or data transmission. The comparable uplink multi-user access techniques including TDMA, FDMA, CDMA and other multiplexing techniques require further studies.
- According to the principle of TSC scheme, the code set is determined according to the number of users. The system is thus required to be flexible and adaptive with the increasing or decreasing number of users registered in the OWC network. With the uplink being built, it is essential to develop an optical wireless protocol to realise user registration process in the OWC network. The protocol is also expected to securely facilitate the distribution of time-slot code and securing key to each registered user. Furthermore, data transmission scheduling using the medium access control (MAC) protocol requires research attentions as well.
- A multi-user localisation mechanism provided by OWC link is desired in the future research activities. In particular, an efficient optical wireless based localisation mechanism that is capable to provide and update the locations of multiple users with low latency requires more attentions.

- In this thesis, multiple users are covered by a single expanded optical beam. However, the error-free coverage provided by the single optical beam is limited, which accordingly limit the number of users and the system data rate that can be served. In order to achieve larger error-free coverage to cover more users and/or to provide seamless mobility to users, a novel system architecture remains elusive. A ceiling mounted transmitter array containing multiple lasers is promising to cover different areas. The system using multiple transmitters also has potential to mitigate the blockage issue and strict alignment between transmitter and receiver which are vulnerable in the line-of-sight link with a single transmitter. The space division multiplexing technique can be employed together with multiple transmitters to eliminate interference between each transmitter. The coordination among multiple transmitters for data transmission and handover issues need to be further investigated.
- In addition, the applicability of cooperation among multiple transmitters is promising to offer various benefits including high power efficiency and high data rate. The user served by more than two transmitters would employ diversity techniques such as selection diversity and maximal ratio combining to improve its communication performance with higher data rate or larger error-free coverage. However, to benefit from cooperative transmission scheme, a diffused beam might be employed to cover the entire room. The communication link provided by this diffused beam is not required to support high-speed services but is responsible to monitor the entire room to acquire full knowledge and thus to efficiently allocate the resources. A protocol that optimises resource allocation needs to be further developed.
- In addition to employing OWC alone, a hybrid network architecture that employs more than two techniques deserves further investigation. For example, millimetre wave technology or Wi-Fi has potential to be integrated with OWC technique. The hybrid network architecture is flexible for various data traffic demands and different coverage requirements. It also has potential to provide seamless mobility to multiple users and is immune to optical link blockage. However, adaptive handover/switching with low latency from one technique to another is challenging and interesting to be investigated in the future.

- Considering that the experimental setup used in this thesis is based on discrete components, the bulky size and strict alignment requirement obstruct the advance of the system into commercialised use. Therefore, a portable integrated transceiver that releases alignment while improving optical power collection efficiency is desired and a research targeting the development of such low profile integrated transceiver using rapidly maturing platforms such as the silicon photonics would be required to demonstrate practical viability of optical wireless transmission. In addition, with the integrated hardware being available, it is invaluable to investigate and elaborate economic and practical aspects when installing the OWC system for indoor applications along with theoretical studies. Particularly, a comprehensive comparison amongst the potential technologies regarding economic and practical aspects is appreciated.

Bibliography

1. N. Al-Falahy and O. Y. Alani, “Potential technologies to 5G network: challenges and opportunities,” IT Professional, vol. 19, no. 1, pp. 12-20, 2017
2. T. T. Dateki, H. Seki, and M. Minowa, “From LTE-advanced to 5G: Mobile access in progress,” Fujitsu Sci. Tech. J., vol. 52, no. 2, pp. 97–102, Apr. 2016.
3. G. R. Aiello and G. D. Rogerson, “Ultra-wideband wireless systems”, IEEE Microwave Magazine, vol. 4, no. 2, pp. 36-47, 2003.
4. V. Niemela, J. Haapola, M. Hamalainen, and J. Iinatti, “An ultra wideband survey: global regulations and impulse radio research based on standards”, IEEE Communications Surveys & Tutorials, vol. 19, no. 2, pp. 874-890, 2017
5. K. Saha, V. V. Vira, A. Garg, D. Koutsonikolas, “A feasibility study of 60 GHz indoor WLANs,” In Computer Communication and Networks (ICCCN), 2016 25th International Conference on (pp. 1-9). IEEE, 2016.
6. M. P. J. Lavery, H. Huang, Y. Ren, G. Xie, and A. E. Willner, “Demonstration of a 280 Gbit/s free-space spacedivision-multiplexing communications link utilizing plane-wave spatial multiplexing,” Opt. Lett. 41(5), 851– 854 (2016).
7. Z. Cao, L. Shen, Y. Jiao, X. Zhao, and T. Koonen, “200 Gbps OOK transmission over an indoor optical wireless link enabled by an integrated cascaded aperture optical receiver,” in Optical Fiber Communication Conference (2017), paper Th5A.6.
8. J. M. Kahn and J. R. Barry, “Wireless infrared communications,” Proc. IEEE 85(2), 265–298 (1997)
9. E. Wong, M. P. I. Dias, and L. Ruan, “Predictive resource allocation for tactile internet capable passive optical LANs,” Journal of Lightwave Technology, vol. 35, no. 13, pp. 2629-2641, 2017
10. A. Aijaz, M. Dohler, A. H. Aghvami, V. Friderikos, and M. Frodigh, “Realizing the tactile internet: haptic communications over next generation 5G cellular networks,” IEEE Wireless Communications, vol. 24, no. 2, pp. 82-89, 2017.

11. J. Kim, J. Lee, and W. Lee, “Strategic control of 60 GHz millimeter-wave high-speed wireless links for distributed virtual reality platforms,” Mobile Information Systems, vol. 2017, Article ID. 5040347, 2017
12. E. Bastug, M. Bennis, M. Medard, and M. Debbah, “Toward interconnected virtual reality: opportunities, challenges, and enablers,” IEEE Communications Magazine, vol. 55, no. 6, pp. 110-117, 2017
13. X. Ge, L. Pan, Q. Li, G. Mao, and S. Tu, “Multipath cooperative communications networks for augmented and virtual reality transmission,” IEEE Transactions on Multimedia, vol. 19, no. 10, pp. 2345-2358, 2017
14. E. Hanada, “The electromagnetic environment of hospitals: how it is affected by the strength of electromagnetic fields generated both inside and outside the hospital,” Annali-Istituto Superiore Di Sanita, vol. 43, no. 3, pp. 208–217, 2007.
15. A. Doufexi, S. Armour, M. Butler, A. Nix, D. Bull, and H. McGeehan, “A comparison of the HIPERLAN/2 and IEEE 802.11a wireless LAN standards,” IEEE Communications Magazine, vol. 40, no. 5, pp/ 172-180, 2002.
16. S. Mangold, S. Choi, G.R. Hiertz, O. Klein, and B. Walke, “Analysis of IEEE 802.11e for QoS support in wireless LANs,” IEEE Wireless Communications, vol. 10, no. 6, pp. 40-50, 2003.
17. D. Vassis, G. Kormentzas, A. Rouskas, and I. Maglogiannis, “The IEEE 802.11g standard for high data rate WLANs,” IEEE Network, vol. 19, no. 3, pp. 21-26, 2005.
18. Y. Xiao, “IEEE 802.11n: enhancements for higher throughput in wireless LANs,” IEEE Wireless Communications, vol. 12, no. 6, pp. 82-91, 2005.
19. E. Perahia, M.X. Gong, “Gigabit wireless LANs: an overview of IEEE 802.11 ac and 802.11 ad,” ACM SIGMOBILE Mobile Computing and Communications Review, vol. 15, no. 3, pp. 23-33, 2011.
20. B. Bellalta, “IEEE 802.11AX: high-efficiency WLANs,” IEEE Wireless Communications, vol. 23, no. 1, pp. 38-46, 2016.
21. Wi-Fi Alliance, “Securing Wi-Fi wireless networks with today’s technologies,” 2003.
22. W. Sun, O. Lee, Y. Shin, S. Kim, C. Yang, H. Kim and S. Choi, “Wi-Fi could be much more,” IEEE Communications Magazine, vol. 52, no. 11, pp. 22-29, 2014
23. "Official IEEE 802.11 working group project timelines". January 26, 2017. Retrieved 2017-02-12.

24. T. Nitsche, C. Cordeiro, A. B. Flores, E. W. Knightly, E. Perahia, and J. C. Widmer, "IEEE 802.11ad: directional 60 GHz communication for multi-gigabit-per-second Wi-Fi (invited paper)," IEEE Communications Magazine, vol. 52, no. 12, pp. 132-141, 2014.
25. Y. Ghasempour, C. R. C. M. da Silva, C. Cordeiro, and E. W. Knightly, "IEEE 802.11ay: next-generation 60 GHz communication for 100 Gb/s Wi-Fi," IEEE Communications Magazine, vol. PP. no. 99, pp. 1-7, 2017.
26. L. Jing, C. R. Rowell, S. Raju, M. Chan, R. D. Murch, and C. P. Yue, "Fabrication and measurement of millimeter-wave on-chip MIMO antenna for COMS RFIC's," In Wireless Symposium (IWS), 2016 IEEE MTT-S International(pp. 1-4). IEEE, 2016.
27. A. L. Swindlehurst, E. Ayanoglu, P. Heydari, and F. Capolino, "Millimeter-wave massive MIMO: the next wireless resolution?" IEEE Communications Magazine, vol.52 no. 9, pp. 56-92, 2014.
28. H. Kuo, C. Lin, C. Yu, P. Lo, J. Lyu, C. Chou, and H. Chuang, "A fully integrated 60-GHz CMOS direct-conversion Doppler radar RF sensor with clutter canceller for signle-antenna noncontact human vital-signs detection," IEEE transactions on Microwave Theory and Techniques, vol. 64, no. 4, pp. 1018-1028, 2016.
29. I. Nasr, R. Jungmaier, A. Baheti, D. Noppeney, J. S. Bal, M. Wojnowski, E. Karagozier, H. Raja, J. Lien, I. Poupyrev, and S. Trotta, "A highly integrated 60 GHz 6-channel transceiver with antenna in package for smart sensing and short-range communications," IEEE Journal of Solid-State Circuits, vol. 51, no. 9, pp. 2066-2076, 2016.
30. A. Stohr, B. Shih, S. T. Abraha, A. G. Steffan, and A. Ng'oma, "High spectral-efficient 512-QAM-OFDM 60 GHz CRoF system using a coherent photonic mixer (CPX) and an RF envelope detector," in Optical Fiber Communication Conference (OFC), pp. Tu3B.4, 2016.
31. R. Wu, S. Kawai, Y. Seo, N. Fajri, K. Kimura, S. Sata, S. Kondo, T. Ueno, T. Siriburanon, S. Maki, B. Liu, Y. Wang, N. Nagashima, M. Miyahara, K. Okada, and A. Matsuzawa, "A 42 Gb/s 60 GHz CMOS transceiver for IEEE 802.11ay," Solid-State Circuits (ISSCC), 2016 IEEE International Conference on, pp. 248-249, 2016.
32. S. Sur, V. Venkateswaran, X. Zhang and P. Ramanathan, "60 GHz indoor networking through flexible beams: a link-level profiling," in the Proceedings of

the 2015 ACM SIGMETRICS International Conference on Measurement and Modeling of Computer Systems, pp. 71-84, Portland, Oregon, USA, 2015

33. S. E. Alavi, M. R. K. Soltanian, I. S. Amiri, M. Khalily, A. S. M. Supa'at, and H. Ahmad, "Towards 5G: a photonic based millimeter wave signal generation for applying in 5G access fronthaul," Scientific Report, vol. 6, pp. 19891, 2016.
34. L. Fan, G. Xia, J. Chen, X. Tang, Q. Liang, and Z. Wu, "High-purity 60 GHz band millimeter-wave generation based on optically injected semiconductor laser under subharmonic microwave modulation," Optics Express, vol. 24, no. 16, pp. 18252-18265, 2016.
35. Y. Tian, KL. Lee, C. Lim, and A. Nirmalathas, "Experimental comparison of DSB-SC & OSSB based 60 GHz radio-over-fiber frontaul links, " Microwave Photonics (MWP), 2016 IEEE International Topical Meeting on, pp. 141-144, 2016.
36. Y. Tian, KL. Lee, C. Lim, and A. Nirmalathas, "60 GHz analog radio-over-fiber fronthaul investigations, " Journal of Lightwave Technology, vol. 35, no. 19, pp. 4304-4310, 2017.
37. L. Zhang, M. Zhu, C. Ye, SH. Fan, C. Liu, X. Hu, P. Cao, Q. Chang, Y. Su, and GK. Chang, "Generation and transmission of multiband and multi-gigabit 60 GHz MMW signals in an RoF system with frequency quintupling technique," Optics Express, vol. 21, no. 8, pp. 9899-9905, 2013.
38. A. Nirmalathas, C. Lim, and Y. Yang, "Digitized RF over fiber systems," Advanced Photonics for Communications, OSA 2014, pp. ST1D.1, San Diego, CA, US, July 2014.
39. S. Geng, D. Liu, Y. Liu, H. Zhuo, W. Rhee and Z. Wang, "A 13.3 mW 500 Mb/s IR-UWB transceiver with link margin enhancement technique for meter-range communications," IEEE Journal of Solid-State Circuits, vol. 50, no. 3, pp. 669-678, 2015.
40. J. P. Yao, F. Zeng, and Q. Wang, "Photonic generation of ultrawideband signals," J. Lightwave Technol., vol. 25, no. 11, pp. 3219–3235, 2007.
41. J. He, F. Long, R. Deng, J. Shi, M. Dai, and L. Chen, "Flexible multiband OFDM ultra-wideband services based on optical frequency combs", Journal of Optical Communications and Networking, vol. 9, no. 5, pp. 393-400, 2017.
42. R. Puerta, S. Rommel, J. J. V. Olmos, and I. T. Monroy, "10 Gb/s ultra-wideband wirelss transmission based on multi-band carrierless amplitude phase modulation",

Wireless and Microwave Technology Conference (WAMICON), 2016 IEEE 17th Annual, Clearwater, FL, USA, June 2016.

43. H. Elgala, R. Mesleh, H. Haas, “Indoor optical wireless communication: potential and state-of-the-art,” Communication Magazine, IEEE, vol. 49, no. 9, pp. 56-62, 2011.
44. C. Singh, J. John and K.K. Tripathi, “A review of indoor optical wireless systems,” IETE Technical Review, vol. 19, no. 1-2, pp. 3-17, 2002.
45. S. Prince, A. M. Vibin, “Optical wireless audio communication using LED lighting system”, Wireless Personal Communications, vol. 86, no. 3, pp/ 1159-1168, 2016.
46. D. Karunatilaka, V. Kalavally, and R. Parthiban, “Improving lighting quality and capacity of OFDM-based WDM-VLC systems”, IEEE Photonics Technology Letters, vol. 28, no. 20, pp. 2149-2152, 2016.
47. S. Liu, X. Chi, and L. Zhao, “Bandwidth allocation under multi-level service guarantees of downlink in the VLC-OFDM system”, Journal of the Optical Society of Korea, vol. 20, no. 6, pp. 704-715, 2016
48. C. Hsu, C. Chow, I. Lu, Y. Liu, C. Yeh, and Y. Liu, “High speed imaging 3 by 3 MIMO phosphor white-light LED based visible light communication system”, IEEE Photonics Journal, vol. 8, no. 6, 2016.
49. J. Li, Y. Xu, J. Shi, Y. Wang, X. Ji, H. Ou, and N. Chi, “A 2 by 2 imaging MIMO system based on LED visible light communications employing space balanced coding and integrated PIN array reception”, Optics Communications, vol. 367, pp. 214-218, 2016.
50. Y. Zhou, J. Shi, Z. Wang, J. Zhang, X. Huang, and N. Chi, “Maximization of visible light communication capacity employing quasi-linear preequalization with peak power limitation”, Mathematical Problems in Engineering, vol. 2016, no. 2016, pp. 6902152, 2016.
51. H. Li, X. Chen, B. Huang, D. Tang, and H. Chen, “High bandwidth visible light communications based on a post-equalization circuit,” IEEE Photonics Technol. Lett., vol. 26, no. 2, pp. 119–122, 2014.
52. Z. Wang, W. Zhong, C. Yu, J. Chen, C. P. S. Francois, and W. Chen, “Performance of dimming control scheme in visible light communication system”, Optics Express, vol. 20, no. 17, pp. 18861-18868, 2012.

53. J. Fang, Z. Chen, Z. L. Jiang, X. Yu, S. Yiu, K. Ren, X. Tan, and Z. Chen, “An efficient flicher-free FEC coding scheme for dimmable visible light communication based on polar codes”, IEEE Photonics Journal, vol. 9, no. 3, 2017.
54. F. Yang and J. Gao, “Dimming control scheme with high power and spectrum efficiency for visible light communications”, IEEE Photonics Journal, vol. 9, no. 1, 2017.
55. Y. Yang, Z. Zeng, J. Cheng, and C. Guo, “Spatial dimming scheme for optical OFDM based visible light communication”, Optics Express, vol. 24, no. 26, pp. 30254-30263, 2016.
56. H. Wang and S. Kim, “Dimming control systems with polar codes in visible light communication”, IEEE Photonics Technology Letters, vol. 29, no. 19, pp. 1651-1654, 2017.
57. S. Lou, C. Gong, N. Wu, and Z. Xu, “Joint dimming and communication design for visible light communication”, IEEE Communications Letters, vol. 21, no. 5, pp. 1043-1046, 2017.
58. A.G. Alkholidi, K.S. Altowij, “Free space optical communications – theory and practice,” DOI: 10.5772/58884, 2014.
59. Z. Ghassemlooy, S. Arnon, M. Uysal, Z. Xu, and J. Cheng, “Emerging optical wireless communications – advances and challenges,” IEEE Journal on Selected Areas in Communications, vol. 33, no. 9, pp. 1738-1749, 2015.
60. Z. Cao, Y. Jiao, L. Shen, X. Zhao, R. Stabile, J. J. G. M. V. D. Tol, and T. Koonen, “Ultra-high throughput indoor infrared wireless communication system enabled by a cascaded aperture optical receiver fabricated on InP membrane,” Journal of Lightwave Technology, vol. PP, no. 99, pp. 1-11, 2017.
61. A. Gomez, K. Shi, C. Quintana, M. Sato, G. Faulkner, B. C. Thomsen, and D. O’Brien, “Beyond 100 Gb/s indoor wire field-of-view optical wireless communications,” IEEE Photonics Technology Letters, vol. 27, no. 4, pp. 367–370, 2015.
62. K. Langer and J. Grubor, “Recent developments in optical wireless communications using infrared and visible light,” Transparent Optical Networks, 2007. ICTON ’07. 9th International Conference on, pp. 146-151 (Tu. D3. 1), Rome, Italy, July 2007.
63. C. W. Oh, Z. Cao, E. Tangdiongga, and T. Koonen, “Free-space transmission with passive 2D beam steering for multi-gigabit-per-second per-beam indoor optical wireless networks,” Optics Express, vol. 24, no. 17, pp. 19211-19227, 2016.

64. J. B. Carruther and J. M. Kahn, “Angle diversity for nondirected wireless infrared communication,” IEEE Transactions on Communications, vol. 48, no. 6, pp. 960-969, 2000.
65. K. Wang, A. Nirmalathas, C. Lim, and E. Skafidas, “High-speed duplex optical wireless communication system for indoor personal area networks,” Optics Express, vol. 18, no. 24, pp. 25199-25216, 2010.
66. K. Wang, A. Nirmalathas, C. Lim, and E. Skafidas, “Experimental demonstration of a full-duplex indoor optical wireless communication system,” IEEE Photonics Technology Letters, vol. 24, no. 3, pp. 188-190, 2011.
67. E. A. Alyan, S. A. Aljunid, M. S. Anuar, and C. B. M. Rashidi, “SAC-OCDMA over indoor optical wireless communication (OWC) system based on zero cross correlation (ZCC) code,” Materials Science Forum, vol. 857, pp. 603-607, Trans Tech Publications, 2016.
68. Z. Zheng, T. Chen, L. Liu, and W. Hu, “Experimental demonstration of femtocell visible light communication system employing code division multiple access,” in the Proceedings of Optical Fiber Communication Conference (OFC), pp. Tu2G.4, Los Angeles, CA, USA, March 2015.
69. O. Gonzalez, J. A. Martin-Gonzalez, M. F. Guerra-Medina, F. J. LopezHernandez, and F. A. Delgado-Rajo, “Cyclic code-shift extension keying for multi-user optical wireless communications,” Electro. Lett., vol. 51, no. 11, pp. 847–849, May 2015.
70. Y. Wang, Y. Wang, L. Tao, J. Shi, and N. Chi, “Experimental demonstration of a full-duplex high-speed visible light communication access network architecture based on frequency division multiplexing,” Optical Engineering, vol. 53, no. 11, pp. 116104, 2014.
71. K. Wang, A. Nirmalathas, C. Lim and E. Skafidas, “Indoor gigabit full-duplex optical wireless communication system with SCM based multiple-user access,” Microwave Photonics, 2011 International Topical Meeting on & Microwave Photonics Conference, 2011 Asia-Pacific MWP/APMP, 2011.
72. C. Yang, Y. Wang, X. Huang and N. Chi, “Demonstration of high-speed multi-user multi-carrier CDMA visible light communication,” Optics Communications, vol.335, no. 2015, pp. 269-272, 2015.
73. J.M. Kahn and J.R. Barry, “Wireless Infrared Communications,” Proceeding IEEE, vol.85, no.2, pp. 265-298, 1997.

74. T. Song, K. Wang, J. Ma, and A. Nirmalathas, “Experimental demonstration of optical wireless personal area communication system supporting multiple users,” in the Proceedings of Optical Fiber Communication Conference (OFC), pp. Th2A.20, Anaheim, CA, USA, March 2016.
75. Z. Ding, X. Lei, G. K. Karagiannidis, R. Schober, J. Yuan, and V. Bhargava, “A survey on non-orthogonal multiple access for 5G networks: research challenges and future trends,” IEEE Journal on Selected Areas in Communications, vol. 35, no. 10, pp. 2181-2195, 2017.
76. L. Dai, B. Wang, Y. Yuan, S. Han, C. I, and Z. Wang, “Non-orthogonal multiple access for 5G: solutions, challenges, opportunities, and future research trends,” IEEE Communications Magazine, vol. 53, no. 9, pp. 74-81, 2015.
77. H. Marshoud, V. M. Kapinas, G. K. Karagiannidis, and S. Muhaidat, “Non-orthogonal multiple access for visible light communications,” IEEE Photonics Technology Letters, vol. 28, no. 1, pp. 51-54, 2016.
78. Y. Saito, Y. Kishiyama, A. Benjebbour, T. Nakamura, A. Li, and K., 2013 Higuchi, “Non-orthogonal multiple access (NOMA) for cellular future radio access”, In Vehicular Technology Conference (VTC Spring), 2013 IEEE 77th (pp. 1-5). IEEE, June 2013.
79. X. Guan, Y. Hong, Q. Yang, and C. Chan, “Phase pre-distortion for non-orthogonal multiple access in visible light communications,” in the Proceedings of Optical Fiber Communication Conference (OFC), pp. Th1H.4, Anaheim, CA, USA, March 2016.
80. Z. Ding, M. Peng, and H. V. Poor, “Cooperative non-orthogonal multiple access in 5G systems,” IEEE Communications Letters, vol. 19, no. 8, pp. 1462-1465, 2015.
81. B. Wang, K. Wang, Z. Lu, T. Xie, and J. Quan, “Comparison study of non-orthogonal multiple access schemes for 5G,” In Broadband Multimedia Systems and Broadcasting (BMSB), 2015 IEEE International Symposium on (pp. 1-5). IEEE, Ghent, Belgium, 2015.
82. Y. Wang, Y. Wang, N. Chi, J. Yu, and H. Shang, “Demonstration of 575 Mb/s downlink and 225 Mb/s uplink bi-directional SCM-WDM visible light communication using RGB LED and phosphor-based LED,” Optics Express, vol. 21, no. 1, pp. 1203-1208, 2013.

83. T. A. Tsiftsis, H. G. Sandalidis, G. K. Karagiannidis, and M. Uysal, “Optical wireless links with spatial diversity over strong atmospheric turbulence channels,” IEEE Transactions on Wireless Communications, vol. 8, no. 2, pp. 951-957, 2009.
84. J. B. Carruthers and J. M. Kahn, “Angle diversity for nondirected wireless infrared communication,” IEEE Transactions on Communications, vol. 48, no. 6, pp. 960-969, 2000.
85. B. Schnabel, E. Kley, and F. Wyrowski, “Study on polarization visible light by subwavelength-perid metal-stripe gratings,” Optical Engineering, vol. 38, no. 2, 1999.
86. D. Kwon, S. Kim, S. Yang, and S. Han, “Optimized pre-equalization for gigabit polarization division multiplexed visible light communication,” Optical Engineering, vol. 54, no. 7, pp. 076101, 2015.
87. X. Li, J. Yu, N. Chi, and J. Zhang, “Optical-wireless-optical full link for polarization multiplexing quadrature amplitude/phase modulation signal transmission,” Optics Letters, vol. 38, no. 22, pp. 4712-4715, 2013.
88. S. Kim, D. Kwon, S. Yang, and S. Han, “Asymmetric multi-input multi-output system in visible light communication for polarization-tolerant polarization division multiplexing transmission,” Optical Engineering, vol. 55, no. 3, pp. 036102, 2016.
89. Y. Wang, C. Yang, Y. Wang, and N. Chi, “Gigabit polarization division multiplexing in visible light communication,” Optics Letter, vol. 39, no. 7, 1823-1826, 2014.
90. S. L. Jansen, I. Morita, T. C. W. Schenk, and H. Tanaka, “Long-haul transmission of 16×52.5 Gbits/s polarization-division-multiplexed OFDM enabled by MIMO processing (invited),” Journal of Optical Networking, vol. 7, no. 2, pp. 173-182, 2008.
91. J. Wang, J. Yang, I. M. Fazal, N. Ahmed, Y. Yang, H. Huang, Y. Ren, Y. Yue, S. Dolinar, M. Tur, and A. E. Willner, “Terabit free-space data transmission employing orbital angular momentum multiplexing,” Nature Photonics, vol. 6, no. 7, pp. 488-496, 2012.
92. G. Gibson, J. Courial, M. J. Padgett, M. Vasnetsov, V. Pas’ko, S. M. Barnett, and S. Fanke-Arnold, “Free-space information transfer using light beams carrying orbital angular momentum,” Optics Express, vol. 12, no. 22, pp. 5448-5456, 2004.

93. A. Trichili, C. Rosales-Guzman, A. Dudley, B. Ndagano, A. B. Salem, M. Zghal, and A. Forbes, "Optical communication beyond orbital angular momentum," Scientific Reports, vol. 6, pp. 27674, 2016.
94. Y. Fang, J. Yu, J. Zhang, N. Chi, J. Xiao, and G. Chang, "Ultrahigh-capacity access network architecture for mobile data backhaul using integrated W-band wireless and free-space optical links with OAM multiplexing," Optics Letters, vol. 39, no. 14, pp. 4168-4171, 2014.
95. L. Zou, L. Wang, S. Zhao, and H. Chen, "Turbulence mitigation scheme based on multiple-user detection in an orbital-angular-momentum multiplexed system," Chinese Physics B, vol. 25, no. 11, pp. 114215, 2016.
96. T. Lei, M. Zhang, Y. Li, P. Jia, G. N. Liu, X. Xu, Z. Li, C. Min, J. Lin, C. Yu, H. Niu, and X. Yuan, "Massive individual orbital angular momentum channels for multiplexing enabled by Dammann gratings," Light: Science & Applications, vol. 4, no. 3, pp. e257, 2015.
97. M. Mirhosseini, M. Malik, Z. Shi, and R. W. Boyd, "Efficient separation of the orbital angular momentum eigenstates of light," Nature Communications, vol. 4, pp. 2781, 2013.
98. G. Xie, L. Li, Y. Ren, H. Huang, Y. Yan, N. Ahmed, Z. Zhao, M. P. J. Lavery, N. Ashrafi, S. Ashrafi, R. Bock, M. Tur, A. F. Molisch, and A. E. Willner, "Performance metrics and design considerations for a free-space optical orbital-angular-momentum-multiplexed communication link," Optica, vol. 2, no. 4, pp. 357-365, 2015.
99. D. Bykhovsky and S. Arnon, "Multiple access resource allocation in visible light communication system," Journal of Lightwave Technology, vol. 32, no. 8, pp. 1594-1600, 2014.
100. T. Rahman, D. Rafique, B. Spinnler, A. Napoli, M. Bohn, A. M. J. Koonen, C. M. Okonkwo, and H. de Waardt, "Digital subcarrier multiplexed hybrid QAM for data-rate flexibility and ROADM filtering tolerance," in the Proceedings of Optical Fiber Communication Conference (OFC), pp. Tu3K.5, Anaheim, CA, USA, March 2016.
101. Y. Hong, T. Wu, and L. Chen, "On the performance of adaptive MIMO-OFDM indoor visible light communications," IEEE Photonics Technology Letters, vol. 28, no. 8, pp. 907-910, 2016.

102. J. Grubor, V. Jungnickel, and K. Langer, “Capacity analysis in indoor wireless infrared communication using adaptive multiple subcarrier transmission,” in Proceedings of 7th International Conference on Transparent Optical Networks (ICTON), pp. 171-174, Barcelona, Catalonia, Spain, July 2005.

103. C. Kottke, J. Hilt, K. Habel, J. Vucic, and K. Langer, “1.25 Gbit/s visible light WDM link based on DMT modulation of a single RGB LED luminary,” European Conference and Exhibition on Optical Communication, pp. We. 3. B. 4, Amsterdam, Netherlands, Sep. 2012.

104. O. Gonzalez, R. Perez-Jimenez, S. Rodriguez, J. Rabadan, and A. Ayala, “OFDM over indoor wireless optical channel,” IEEE Proceedings – Optoelectronics, vol. 152, no. 4, pp. 199-204, 2005.

105. X. Q. Jin, J. L. Wei, R. P. Giddings, T. Quinlan, S. Walker, and J. M. Tang, “Experimental demonstrations and extensive comparisons of end-to-end real-time optical OFDM transceivers with adaptive bit and/or power loading,” IEEE Photonics Journal, vol. 3, no. 3, pp. 500-511, 2011.

106. A. M. Khalid, G. Cossu, R. Corsini, P. Choudhury, and E. Ciaramella, “1 Gb/s transmission over a phosphorescent white LED by using rate-adaptive discrete multitoned modulation,” IEEE Photonics Journal, vol. 4, no. 5, pp. 1465-1473, 2012.

107. V. Curri, A. Carena, P. Poggiolini, R. Cigliutti, F. Forghieri, C. Fludger, T. Kupfer, “Time-division hybrid modulation formats: Tx operation strategies and countermeasures to nonlinear propagation,” in Proceedings of Optical Fiber Communication Conference, San Francisco, CA, USA, 2014, Paper Tu3A.2.

108. X. Zhou, L. E. Nelson, and P. Magill, “Rate-adaptable optics for next generation long-haul transport networks,” IEEE Communications Magazine, vol. 51, no. 3, pp. 41-49, 2013.

109. Q. Zhuge, M. Morsy-Osman, X. Xu, M. Chagnon, M. Qiu, and D. V. Plant, “Spectral efficiency-adaptive optical transmission using time domain hybrid QAM for agile optical networks,” Journal of Lightwave Technology, vol. 31, no. 15, pp. 2621-2628, 2013.

110. A. A. Saed, S. Ho, and C. W. Sung, “Adaptive modulation for two users in VLC,” in Proc. IEEE Globalcom Workshop, San Diego, CA, USA, 2015, pp. 1–6.

111. D. A. A. Mello, A. N. Barreto, T. C. Lima, T. F. Portela, L. Beygi, and J. M. Kahn, “Optical networking with variable-code-rate transceivers,” Journal of Lightwave Technology, vol. 32, no. 2, pp. 257–266, Nov. 2013.

112. G. Gho and J. M. Kahn, “Rate-adaptive modulation and low-density parity-check coding for optical fiber transmission systems,” Journal of Optical Communications and Networking, vol. 4, no. 10, pp. 760-768, 2012.

113. M. Wang, J. Wu, W. Yu, H. Wang, J. Li, J. Shi, and C. Luo, “Efficient coding modulation and seamless rate adaptation for visible light communications,” IEEE Wireless Communications, vol. 22, no. 3, pp. 86-93, 2015.

114. H. Cui, C. Luo, K. Tan, F. Wu, and C. W. Chen, “Seamless rate adaptation for wireless networking,” In Proceedings of the 14th ACM International Conference on Modelling, Analysis and Simulation of Wireless and Mobile Systems pp. 437-446, Miami, Florida, USA, Nov. 2011.

115. J. Li, Z. Feng, and P. Zhang, “A survey of security issues in cognitive radio networks,” China Communications, vol. 12, no. 3, pp. 132-150, 2015.

116. M. Agaskar and V. W. S. Chan, “Nulling strategies for preventing interference and interception of free space optical communication,” in Proceedings of IEEE International Conference on Communications (2013), pp. 3927–3932.

117. A. Mostafa and L. Lampe, “Physical-layer security for indoor visible light communications,” in Proceedings of IEEE International Conference on Communications (2014), pp. 3342–3347.

118. J. Qiu, L. Zhang, D. Li, and X. Liu, “High security chaotic multiple access scheme for visible light communication systems with advanced encryption standard interleaving,” Optical Engineering, vol. 55, no. 6, pp. 066121, 2016.

119. W. Zhang, C. Zhang, W. Jin, C. Chen, N. Jiang, and K. Qiu, “Chaos coding based QAM IQ-encryption for improved security in OFDMA-PON,” IEEE Photonics Technol. Lett., vol. 26, no. 19, pp. 1964–1967, 2014.

120. C. Kurtsiefer, P. Zarda, M. Halder, H. Weinfurter, P. M. Gorman, P. R. Tapster, and J. G. Rarity, “Quantum cryptography: a step towards global key distribution,” Nature, vol. 419, no. 6906, pp. 450, 2002.

121. A. R. Dixon, Z. L. Yuan, J. F. Dynes, A. W. Sharpe, and A. J. Shields, “Gigahertz decoy quantum key distribution with 1 Mbit/s secure key rate,” Opt. Express, vol. 16, no. 23, pp. 18790–18797, 2008.

122. K. Wang, A. Nirmalathas, C. Lim, and E. Skafidas, “High-speed duplex optical wireless communication system for indoor personal area networks,” Optics Express, vol. 18, no. 24, pp. 25199-25216, 2010.

123. M. V. Jamali, J. A. Salehi, and F. Akhoundi, “Performance studies of underwater wireless optical communication systems with spatial diversity: MIMO scheme,” IEEE Transactions on Communications, vol. 65, no. 3, pp. 1176-1192, 2016

124. M. P. Prabakaran, A. Sivasubramanian and K. Chitra, “Performance analysis of QAM with MEMS based SCIR for indoor optical wireless communication,” Applied Mechanics and Materials, vol. 592-594, no. 2014, pp. 2189-2192, 2014

125. S. A. Self, “Focusing of spherical Gaussian beams”, Applied optics, vol. 22, no. 5, pp.658-661, 1983.

126. P. LoPresti, H. Refai, and J. Sluss. "Adaptive power and divergence to improve airborne networking and communications." In 24th Digital Avionics Systems Conference IEEE, DASC, vol. 1, pp. 1-B, 2005.

127. R. A. Shafik, M. S. Rahman, and A. R. Islam. "On the extended relationships among EVM, BER and SNR as performance metrics." In Electrical and Computer Engineering International Conference on (ICECE), IEEE, pp. 408-411, 2006.

128. P. J. Winzer and W. R. Leeb, "Fiber coupling efficiency for random light and its applications to lidar." Optics letters, vol. 23, no. 13, pp. 986-988, 1998.

129. I. P. Kaminow and T. L. Koch, Optical fiber telecommunications III, Academic Press, 1997.

130. S. E. Hashemi, “Relative intersity noise (RIN) in high-speed VCSELs for short reach communication”, Master thesis, Department of Microtechnology and Nanoscience, Chalmers University of Technology, 2012

131. J. B. Carruthers, “Multipath Channels in Wireless Infrared Communications: Modeling, angle diversity and estimation,” Ph.D. dissertation, Univ. of California, Berkeley, 1997.

132. B. Leskovar, "Optical receivers for wide band data transmission systems." IEEE Transactions on Nuclear Science, vol. 36, no. 1, pp. 787-793, 1989.

133. F. E. Alsaadi and J. M. H Elmirghani. "Adaptive mobile line strip multibeam MC-CDMA optical wireless system employing imaging detection in a real indoor environment," IEEE Journal on Selected Areas in Communications, vol. 27, no. 9, 2009.

134. J. G. Proakis, “Optimal receivers for the additive white Gaussian noise channel,” in Digital Communications, 4th ed. New York, NY, USA: McGraw-Hill, 2000, pp. 276–278.

135. K. Cho and D. Yoon, “On the general BER expression of one-and two-dimensional amplitude modulations,” IEEE Trans. Commun., vol. 50, no. 7, pp. 10 74–1080, Jul. 2002.

136. AS/NZS 2211.1:2004, Safety of laser products (Standards Australia International Ltd and Standards New Zealand, 2004).

137. Y. Wang, X. Huang, L. Tao, J. Shi, and N. Chi, “4.5-Gb/s RGB-LED based WDM visible light communication system employing CAP modulation and RLS based adaptive equalization,” Opt. Express, vol. 23, no. 10, pp. 13626–13633, 2015.

138. J. C.-I. Chuang, “The effects of port synchronization on TDMA personal communications for tow duplexing methods,” in Proc. IEEE 42nd Veh. Technol. Conf., Denver, CO, USA, 1992, pp. 494–497.

139. P. P. Nuspl, K. E. Brown, W. Steenaart, and B. Ghicopoulos, “Synchronization methods for TDMA,” Proc. IEEE, vol. 65, no. 3, pp. 434–444, Mar. 1977

140. F. Sivrikaya and B. Yener, “Time synchronization in sensor network: A survey,” IEEE Netw., vol. 18, no. 4, pp. 45–50, Jul. 2004.

141. J. Snow, W. Feng, and W. Feng, “Implementing a low power TDMA protocol over 802.11,” in Proc. IEEE Wireless Comm. Netw. Conf., New Orleans, LA, USA, 2005, pp. 75–80.

142. P. Signal, S. Rai, R. Punia, and D. Kashyap, Int. J. Comput. Sci. Inf. Technol., vol. 7, no. 107, 2015.

143. K. Wang, A. Nirmalathas, C. Lim, and E. Skafidas, “Impact of background light induced shot noise in high-speed full-duplex indoor optical wireless communication systems,” Opt. Express, vol. 19, no. 22, pp. 21321–21332, 2011

144. K. Wang, A. Nirmalathas, C. Lim, and E. Skafidas, “Experimental demonstration of a novel indoor optical wireless localization system for high-speed personal area networks,” Opt. Lett., vol. 40, no. 7, pp. 1246–1249, Apr. 2015.

145. J. Li, Z. Feng, Z. Feng, and P. Zhang, “A survey of security issues in cognitive radio networks,” China Commun., vol. 12, no. 3, pp. 132–150, 2015.

146. J. C. Sprott, Chaos and Time-Series Analysis (Oxford University, 2003), Chap.2.

147. R. L. Rivest, “Chaffing and winnowing: confidentiality without encryption,” Crypto Bytes, vol. 4, no. 1, pp. 12–17, 1998.

148. J. C. Sprott, Chaos and Time-Series Analysis (Oxford University, 2003), Chap.5

149. C. Zhang, “Period three begins,” Math. Mag., vol. 83, no. 4, pp. 295–297, 2010.

150. W. Zhang, C. Zhang, W. Jin, C. Chen, N. Jiang, and K. Qiu, "Chaos coding-based QAM IQ-encryption for improved security in OFDMA-PON." IEEE Photon. Technol. Lett., vol. 26, no. 19, pp. 1964-1967, 2014.

151. W. Zhang, C. Zhang, C. Chen, H. Zhang, W. Jin, and K. Qiu, "Hybrid chaotic confusion and diffusion for physical layer security in OFDM-PON," IEEE Photonics Journal, vol. 9, no. 2, 2017.

152. M. Lee, "A quasi-monolithic optical receiver using a standard digital CMOS technology." PhD thesis., School of Electrical and Computer Engineering, Georgia Institute of Technology, 1996.

153. M. G. Ahmed, M. Talegaonkar, A. Elkholy, G. Shu, A. Elmallah, A. Rylyakov, and P. K. Hanumolu, "A 12-Gb/s-16.8-dBm OMA Sensitivity 23-mW Optical Receiver in 65-nm CMOS". IEEE Journal of Solid-State Circuits, vol. 53, no. 2, pp. 445-457, 2018.

154. S. H. Huang and W. Z. Chen, "A 25 Gb/s 1.13 pJ/b− 10.8 dBm Input Sensitivity Optical Receiver in 40 nm CMOS", IEEE Journal of Solid-State Circuits, vol. 52, no. 3, pp. 747-756, 2017.

155. D. Li, Z. Zhang, Y. Xie, M. Liu, Q. Yang, and L. Geng, "A 25Gb/s low-noise optical receiver in 0.13 μm SiGe BiCMOS." In IEEE Electronics, Circuits and Systems (ICECS), 2016 IEEE International Conference on, pp. 576-579, 2016.

156. T. Takemoto, Y. Matsuoka, H. Yamashita, Y. Lee, K. Akita, H. Arimoto, M. Kokubo, and T. Ido. "A 50.6-Gb/s 7.8-mW/Gb/s− 7.4-dBm sensitivity optical receiver based on 0.18-μm SiGe BiCMOS technology." In VLSI Circuits (VLSI-Circuits), 2016 IEEE Symposium on, pp. 1-2, 2016.

157. C. Sparrow, The Lorenz equation: bifurcation, chaos, and strange attactors (Springer Science and Business Media, 2012).

158. T. Kohda, A. Tsuneda, and T. Sakae, "Chaotic binary sequences by Chebyshev maps and their correlation properties", In Spread Spectrum Techniques and Applications, 1992. ISSTA 92. IEEE Second International Symposium on, Yokohama, Japan, 1992, pp. 63-66.

Appendix A

For 16-QAM modulation format, consider the first quadrant:

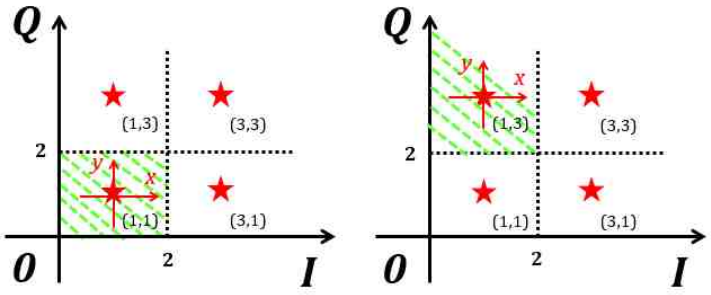

Fig. A1 (a) (b)

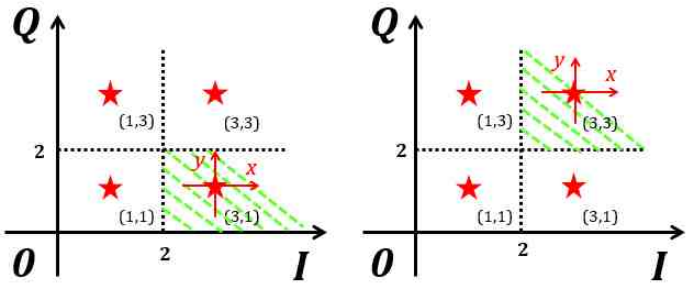

Fig. A2 (a) (b)

The rate (R_1) that received symbols can be demodulated correctly as the reference symbol (1, 1) is calculated by integrating x and y over the decision region of symbol (1, 1), as shown in the green-dash-line region in Fig. A1 (a):

$$R_1 = \int_{-1}^{1}\int_{-1}^{1} f(x,y)dxdy \tag{1.1}$$

The rate (R_2) that received symbols can be demodulated correctly as the reference symbol (1, 3) is calculated by integrating x and y over the decision region of symbol (1, 3), as shown in the green-dash-line region in Fig. A1 (b):

$$R_2 = \int_{-1}^{\infty}\int_{-1}^{1} f(x,y)dxdy \tag{1.2}$$

The rate (R_3) that received symbols can be demodulated correctly as the reference symbol (3, 1) is calculated by integrating x and y over the decision region of symbol (3, 1), as shown in the green-dash-line region in Fig. A2 (a):

$$R_3 = \int_{-1}^{1}\int_{-1}^{\infty} f(x,y)dxdy \tag{1.3}$$

The rate (R_4) that received symbols can be demodulated correctly as the reference symbol (3, 3) is calculated by integrating x and y over the decision region of symbol (3, 3), as shown in the green-dash-line region in Fig. A2 (b):

$$R_4 = \int_{-1}^{\infty}\int_{-1}^{\infty} f(x,y)dxdy \tag{1.4}$$

Since it is assumed that the variables x and y are independent and have the same Gaussian distribution with zero mean and standard deviation, we have:

$$R_2 = R_3 \tag{1.5}$$

After applying the derivation discussed above to the other quadrants, the symbol error rate (SER) for 16-QAM is calculated as:

$$\begin{aligned}
SER_{16-QAM} &= 1 - \frac{4\left(\int_{-1}^{1}\int_{-1}^{1} f(x,y)dxdy + 2\int_{-1}^{\infty}\int_{-1}^{1} f(x,y)dxdy + \int_{-1}^{\infty}\int_{-1}^{\infty} f(x,y)dxdy\right)}{16} \\
&= 1 - \frac{1}{4}\left(\int_{-1}^{1}\int_{-1}^{1} f(x,y)dxdy + 2\int_{-1}^{\infty}\int_{-1}^{1} f(x,y)dxdy + \int_{-1}^{\infty}\int_{-1}^{\infty} f(x,y)dxdy\right) \\
&= 1 - \frac{1}{4}\left(\left(F(1,\sigma) - F(-1,\sigma)\right)^2 + 2\left(F(1,\sigma)\cdot\left(F(1,\sigma) - F(-1,\sigma)\right)\right) + \left(F(1,\sigma)\right)^2\right)
\end{aligned}$$

$$F(v,\sigma) = \int_{-\infty}^{v} \frac{1}{\sigma\sqrt{2\pi}} \exp\left(-\frac{x^2}{2\sigma^2}\right) dx \tag{1.6}$$

Appendix B

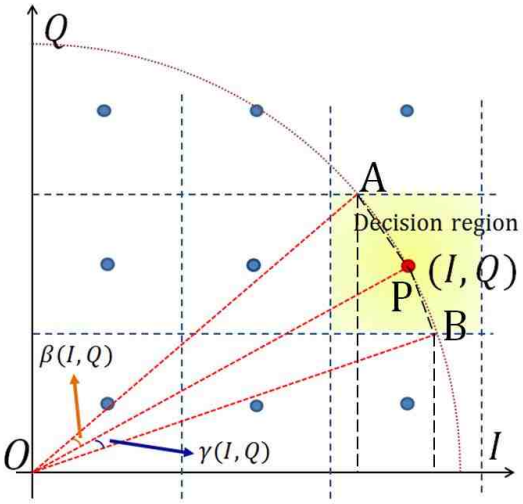

To calculate β and γ, the coordinates of four specific points (O, P, A, B) in the I-Q plane are required, in which:

$$O(0,0), \quad P(I,Q)$$

For $I < Q$:

$$A(I-1, \sqrt{I^2+Q^2-(I-1)^2})$$
$$B(I+1, \sqrt{I^2+Q^2-(I+1)^2})$$

In ΔAOP, we have:

$$|OA|^2 = I^2+Q^2$$
$$|OP|^2 = I^2+Q^2$$
$$|AP|^2 = (I-1-I)^2+\left(\sqrt{I^2+Q^2-(I-1)^2}-Q\right)^2 = 2Q^2+2I-2Q\sqrt{I^2+Q^2-(I-1)^2}$$

Apply the law of cosines, we have:

$$\cos\beta = \frac{|OA|^2 + |OP|^2 - |AP|^2}{2|OA|\cdot|OP|} = \frac{I^2 - I + Q\sqrt{I^2 + Q^2 - (I-1)^2}}{I^2 + Q^2}$$

$$\therefore \beta = \cos^{-1}\frac{I^2 - I + Q\sqrt{I^2 + Q^2 - (I-1)^2}}{I^2 + Q^2}$$

Similarly, in ΔBOP, we have:

$$|OB|^2 = I^2 + Q^2$$

$$|OP|^2 = I^2 + Q^2$$

$$|BP|^2 = (I + 1 - I)^2 + \left(\sqrt{I^2 + Q^2 - (I+1)^2} - Q\right)^2 = 2Q^2 - 2I - 2Q\sqrt{I^2 + Q^2 - (I+1)^2}$$

Apply the law of cosines, we arrive:

$$\cos\gamma = \frac{|OB|^2 + |OP|^2 - |BP|^2}{2|OB|\cdot|OP|} = \frac{I^2 + I + Q\sqrt{I^2 + Q^2 - (I+1)^2}}{I^2 + Q^2}$$

$$\therefore \gamma = \cos^{-1}\frac{I^2 + I + Q\sqrt{I^2 + Q^2 - (I+1)^2}}{I^2 + Q^2}$$

For $I = Q$,

$$A(I-1, \sqrt{I^2 + Q^2 - (I-1)^2})$$

$$B(\sqrt{I^2 + Q^2 - (Q-1)^2}, Q-1)$$

Similar procedures to the case where $I < Q$, we can get:

$$\beta = \cos^{-1}\frac{I^2 - I + Q\sqrt{I^2 + Q^2 - (I-1)^2}}{I^2 + Q^2}$$

$$\gamma = \cos^{-1}\frac{Q^2 - Q + I\sqrt{I^2 + Q^2 - (Q-1)^2}}{I^2 + Q^2}$$

For $I > Q$,

$$A(\sqrt{I^2 + Q^2 - (Q+1)^2}, Q+1)$$

$$B(\sqrt{I^2 + Q^2 - (Q-1)^2}, Q-1)$$

Similar procedures to the case where $I < Q$, we can get:

$$\beta = \cos^{-1}\frac{Q^2+Q+I\sqrt{I^2+Q^2-\left(Q+1\right)^2}}{I^2+Q^2}$$

$$\gamma = \cos^{-1}\frac{Q^2-Q+I\sqrt{I^2+Q^2-\left(Q-1\right)^2}}{I^2+Q^2}$$

Consequently, we arrive:

$$\beta\left(I,Q\right)=\begin{cases}\cos^{-1}\dfrac{I^2-I+Q\sqrt{I^2+Q^2-\left(I-1\right)^2}}{I^2+Q^2}, & I\le Q\\ \cos^{-1}\dfrac{Q^2+Q+I\sqrt{I^2+Q^2-\left(Q+1\right)^2}}{I^2+Q^2}, & I>Q\end{cases}$$

$$\gamma\left(I,Q\right)=\begin{cases}\cos^{-1}\dfrac{I^2+I+Q\sqrt{I^2+Q^2-\left(I+1\right)^2}}{I^2+Q^2}, & I<Q\\ \cos^{-1}\dfrac{Q^2-Q+I\sqrt{I^2+Q^2-\left(Q-1\right)^2}}{I^2+Q^2}, & I\ge Q\end{cases}$$